ABSTRACT

Title of dissertation: Electrolocation-Based Obstacle Avoidance
and Autonomous Navigation in
Underwater Environments

Kedar D. Dimble, Doctor of Philosophy, 2013

Dissertation directed by: Professor J. Sean Humbert
Department of Aerospace Engineering

Weakly electric fish are capable of performing obstacle avoidance in dark and complex aquatic environments efficiently using a navigation technique known as *electrolocation*. That is, electric fish infer relevant information about surrounding obstacles from the perturbations that these obstacles impart to their self-generated electric field. This dissertation draws inspiration from electrolocation to demonstrate unmapped reflexive obstacle avoidance in underwater environments. The perturbation signal, called the *electric image*, contains the spatial information of the perturbing objects regarding their location, size, conductivity etc. Electrostatic equations elucidate the concept of electrolocation and the mechanism of obstacle detection using electric field perturbations. Spatial decomposition of an electric image using Wide-Field Integration processing extracts relative proximity information about the obstacles. The electric field source is changed to an oscillatory one and a quasistatic approach is taken. Simulations were performed in straight tunnel, cluttered corridor and an obstacle field. Experimental validation was conducted with

a setup comprising a tank, a computer-controlled gantry system and an electrosensor. Consistency between the simulations and the experiments was maintained by recreating similar environments.

Simulations using both the electrostatic and the quasistatic approach demonstrate that the algorithm is capable of performing various maneuvers like tunnel centering, wall following and clutter navigation. The experimental results agree with the simulation results and validate the efficacy of the approach in performing obstacle avoidance. The presented approach is computationally lightweight and readily implementable, making underwater autonomous navigation in real-time feasible.

ELECTROLOCATION-BASED OBSTACLE AVOIDANCE AND AUTONOMOUS NAVIGATION IN UNDERWATER ENVIRONMENTS

by

Kedar D. Dimble

Dissertation submitted to the Faculty of the Graduate School of the
University of Maryland, College Park in partial fulfillment
of the requirements for the degree of
Doctor of Philosophy
2013

Advisory Commmittee:

Associate Professor J. Sean Humbert, Chair/Advisor
Associate Professor Derek A. Paley
Associate Professor Raymond Sedwick
Associate Professor Dave Akin
Professor Amr Baz, Dean's Representative

To my beloved, Ovee and Dhrupud, for filling my life outside the lab with loads of joy and happiness.

ACKNOWLEDGEMENTS

showered me with great advice on various topics from time to time. Amar played the role of my go-to stress reliever and financial advisor.

I am really blessed to have a family as amazing as mine. My mother and father, Aai and Baba, strived very hard to put me and my brother through college and to make us good human beings. I am, in all my capacity, still trying to be one. My father being an engineer himself and my mother being from an industrialist family were able to maintain an educational and engineering oriented environment at home when I was growing up. That has in some way worked, I suppose. They finally get to see me attain this doctoral degree, which they were long waiting for. I think I can never thank them enough for all they have done for me. My elder brother, Dada, has served as a big inspiration for me throughout my life due to his hard working and scientific approach towards engineering. I thank him and my sister-in-law for being supportive and encouraging. My lovely niece Ovee and my über energetic son Dhrupud are two utterly entertaining kids who kept me going by helping me switch off the stress from work. Finally, my wife, Vibha, has been a great support while I was being a grad student. Somehow she figured out a way to maintain a family on a grad student salary. She doesn't say but I must have bored her at times by my lab tales and PhD humor. Not to mention her sitting through my presentation rehearsals. In addition there are so many others who have contributed in one way or the other to my work, like my in-laws, old roommates, professors from other schools working on similar projects etc., that it is impossible to thank everyone here.

Finally, I would like to quote a Sanskrit prayer in praise of Saraswati, the Hindu Goddess of knowledge and wisdom.

<div align="center">

या कुन्देन्दु तुषार हार धवला या शुभ्रवस्त्रावृता
या वीणा वरदण्ड मण्डित करा या श्वेतपद्मासना।
या ब्रम्हाच्युत शङ्करप्रभृतिभिर्देवैः सदा वंदिता
सा मां पातु सरस्वती भगवती निःशेषजाड्यापहा॥

</div>

(Gist: O Goddess Saraswati, I pray to you to always protect me from evil and remove all my apathy, laziness and ignorance.)

Table of Contents

List of Tables

List of Figures

Nomenclature

WFI	Wide-Field Integration
FEM	Finite Element Methods
CNC	Computerized Numerical Control
RMS	Root Mean Square
R	Radius of the electro-sensor ring
a	Tunnel width
a_m	Nominal tunnel width
Δa Allowed Perturbation in tunnel width	
Δ Uncertainty in tunnel width	
γ	Locations of electro-receptors
V	Total potential due to the source
V'	Total potential due to image multipole
Φ	Electric image
Q	Charge carried by the source on the sensor
ϵ	Permittivity of water
$P(r, \xi)$	Radial position of point P in space
r_0	Distance of P from the origin
r	Distance of P from center of the sensor
r_e	Distance of P from each electro-receptor
y	Lateral offset of the sensor
θ	Angular offset of the sensor
$\boldsymbol{q}$	State vector $[y, \theta]$
v_i	i^{th} WFI output
F_i	i^{th} basis function
$C^\dagger$	State extraction matrix
m	Number of receptors on the sensor
n	Total number of basis functions
K_y, K_θ	Static feedback gains

Chapter 1

Introduction

Autonomous underwater vehicles have been in existence for more than half a century now, the first being developed at the University of Washington from the late 1950's until early 1960's [1]. Their objective was to measure temperature and sound velocity at varying depths in oceans. In time, there have been significant improvements in vehicles, sensors, algorithms and controllers in order to achieve even complex tasks. Contemporary vehicles are required to be designed to perform tasks like reconnaissance [2, 3], aquatic structures, flora and fauna examination [4], ocean bed imaging [5] etc. Obstacle avoidance forms the basic behavior required by an autonomous vehicle for completing many of these tasks. The obstacle avoidance problem has been handled extensively for robotic vehicles operating on ground [6, 7], in air [8, 9] as well as under water [10, 11, 12], using visual or sonar sensing modalities. Vision and sonar are the two most widely used sensing modalities in underwater robotics. While these work almost flawlessly for airborne and ground vehicles, there are challenges in using them on underwater vehicles. Vision deteriorates at a rapid rate with depth under water. Additionally, dissolved matter in water poses difficulties in clearly detecting objects from visual images. Sonar on the other hand does not

exhibit this problem, however it has a directional nature where only the objects within the sound cone can be realized correctly. Thus several successive scans and added processing of the acquired data is necessary. Sonar reflection and echo from unwanted sources in the environment is another difficulty that is required to be resolved by the processing algorithms. Hence, the success of an obstacle avoidance scheme depends on factors other than the underlying signal processing algorithm. This is evident from the above limitations of underwater vision and sonar based sensing.

This project aims towards addressing these issues with the conventional sensing modalities. Nature presents us with a simple yet effective underwater sensing technique called *electrolocation*, which does not depend on visibility in water and is omnidirectional in nature [13]. By providing a similar capability to an underwater vehicle, a principal, adjunct or redundant method of obstacle sensing and avoidance can be developed.

1.1   Background

1.1.1   Basic Physiology of the Electrolocation System

The two key elements in the electroreception system are the electric organ, which produces the field, and the electro-receptors, which senses the electric field after it has been perturbed by the environment. The electric organ is usually situated in the tail region of the fish [14]. It produces electric field by releasing varying concentrations of positively charged sodium and potassium ions [15]. This process

2

of ion exchange is carried out by arrays of cells called *electrocytes* possessing a complex neural network to control them [16]. The electro-receptors are electrolytic gel-filled narrow-mouthed cups submerged in the skin [17]. They act as biological voltmeters and transmit the sensed voltage to the brain via afferent neurons [16]. Thousands of electro-receptors are distributed over the fish's body, more of them being at preferred locations like the head and trunk [18]. To ensure that no current is drawn by the skin of the fish, the skin has a very high resistance [19].

1.1.2   Concept of an Electric Image

The field lines of the electric field of the fish originate at the electric organ in the tail region and terminate at the electroreceptors dispersed all over the body. When a conductive object is introduced in the fish's field, a local increase in the electric flux and thus a local positive perturbation is observed. By conductive, it is implied that the object is more conductive than the surrounding water, e.g., sea grass, metal pieces, etc. Similarly, a non-conductive object or an object that is less conductive than the water, like rocks, glass pieces, other fish, etc. weaken the electric field locally, thus producing a negative perturbation [20]. This can also be seen in Figure 1.1.

The perturbations are perceived by the fish in the form of voltage spikes at the locations of electro-receptors. The profile of all the spikes together produces a surface with certain "hot-spots" representing the perturbations. Such profiles are called *electric images* [21] and constitute the sensory signal of electric fish.
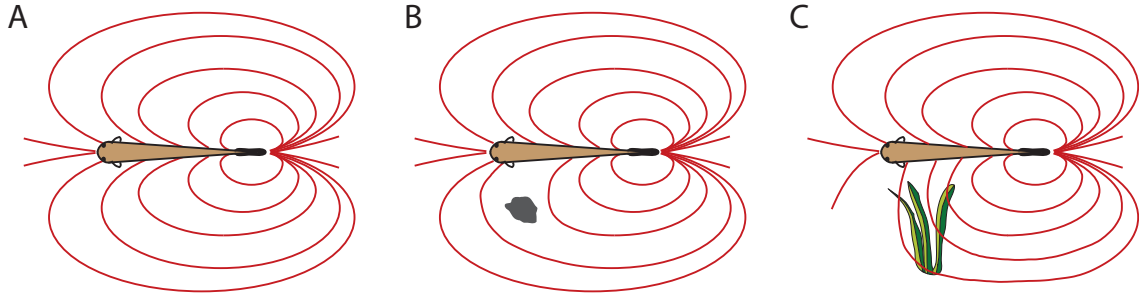
Figure 1.1: Effect of an object on fish's electric field, (A) Unperturbed field, (B) Field lines are dispersed by a non-conductive object, e.g., a rock, (C) Field lines are concentrated by a conductive object, e.g., sea grass.

Perturbations to the field of magnitudes as small as 1μV can also be registered by electric fish in order to interpret the location information of the perturbing object [22]. When one horizontal slice of the fish is considered, the electric image from all the electro-receptors is in the form of a 2D curve instead of a surface, as shown in Figure 1.2. This work considers only planar geometries, because the concept of a planar electric image is important.
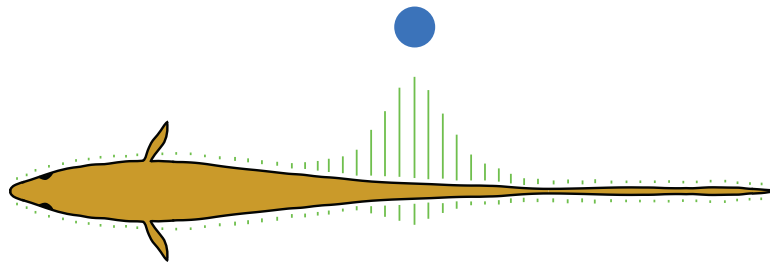
Figure 1.2: Electric image of an object as perceived by a fish.

1.1.3 Motivation for an Artificial Electro-sensor

Weakly electric fish in the *Gymnotiformes* and the *Mormyridae* groups are champions at electrolocation, although each group is known for a different mechanism to perform it. Gymnotiformes, found in South America, produce an electric field that temporally varies as a cyclic wave with a few constituent frequencies superimposed on each other [18], hence referred to as a *wave-type* fish. Mormyridae, found in Africa, generate pulses to create their electric field [18] and are fittingly called *pulse-type* fish. The frequency response of the electric field of wave-type fish is understandably narrow as only a few frequencies are contained in it. On the other hand, the frequency response of a pulse-type fish is wide due to presence of instantaneous pulses. Due to this reason, pulse-type fish are capable of detecting objects with a variety of complex impedance values. However extra effort is required for maintaining a pulse-type electric field as compared to a wave-type field. In this project, while designing the electro-sensor, many of the features found in wave-type fish are adopted directly or after simplification to be compatible with contemporary hardware available.

1.2 Electrolocation in Robotics

Lissmann and Machin [13, 23] performed experiments on electric fish wherein rods of materials with different conductivity were placed in two porous pots, and the fish were rewarded on approaching the pot containing higher conductivity rod. These experiments qualitatively established for the first time that these fish are able to

differentiate objects based on the object's conductivity. It has been known since the work of Lissmann [24] and later Knudsen [25] that the electric field observed sufficiently far from the fish resembles that of an oscillating electric dipole. This finding made possible mathematical analysis of behaviors of electric fish based on electric images. Rasnow [26] derived a formula using electrostatics for analytically computing the electric image of a sphere, with its electrical properties, diameter, and distance from the electric field dipole as variables. Assad et al. [14] further reconstructed the electric fields of different species of electric fish using measurements at multiple sites in the fields. He suggested through behavioral experiments that relative width [14] could be used to model the process by which an electric fish extracts the proximity information of an object from the corresponding electric image. In an independent study by Von der Emde [20], slope-to-amplitude ratio was believed to be a better metric to model the proximity information extraction behavior of a fish. Irrespective of the study, it is clear that electric images possess artifacts that reflect proximity information of the perturbing object.

The response of resistive objects and objects with complex impedance to a fish's electric field were modeled in [27] and [19]. In the case of a resistive object results showed modulation of the magnitude of the peak of the electric image whereas in an object with complex impedance a distortion of the image occurs. Finite Element Method (FEM) was used to model the effect of objects with complex impedance on an electric field similar to that of a fish; similar distortion of electric images were observed [28]. Significant amount of experimental work has also been carried out in this field. In a prototypical setting, it was shown that the exact loca-

6

tion and the approximate shape of an object can be reconstructed from the electric images obtained by sensing it from multiple distinct locations in the environment [29]. In another study, spherical objects of different materials were moved past a biomimetic underwater electro-sensor array to study the effect of object distance on the corresponding electric images [22]. It was verified that the amplitude of electric images decreased with increasing distance and vice versa. In [30], the location of an object was computed in simulation and experiments by solving an inverse problem using a map of electric images previously acquired with the same object at different locations in the environment. Solving the inverse problem involved an interpolation routine based on the predetermined electric images from the map and the electric image due to the object at the required position.

The advent of advanced model estimation methods has enabled researchers to accurately estimate the locations of obstacles in an artificially generated electric field. Solberg et al. [31] used a particle filter to estimate the location of a spherical object in an electric dipole field using two sensing electrodes. Starting with a large number of uniformly dispersed particles, their algorithm was able to iteratively converge on the actual position of the object, either stationary or moving. After extending their two electrode sensor to take a form of a cylindrical array of sensors, the same signal processing technique proved helpful in performing obstacle avoidance by a robot in underwater scenes [32]. They also showed, in a separate work, that Electrical Impedance Tomography can be used to compute the location of objects based on their impedance values computed as a reverse problem from the corresponding electric images [33]. An unscented Kalman filter was shown to

be effective in electrolocating spherical and cubical objects and in performing wall-following maneuvers using a multipole sensor [34, 35]. Using the same experimental setup, in [36] a sensor was demonstrated to travel along electric field lines towards or away from an object depending on whether the object was conductive or non-conductive. The sensor was propelled between non-conductive obstacles towards a conductive object by the resultant field.

For learning a way to extract proximity information from electric images due to global stimuli we used insects as motivation, because insects perceive their visual fields as patterns of relative motion between themselves and the environment, more commonly known as *optic flow* [37, 38]. Specialized neurons called *tangential cells* are used to spatially decompose the optic flow patterns to generate visual cues like visual odometry, useful for navigation [39, 40]. In doing so, they extract the relative information contained in optic flow for control and do not compute the absolute quantities [41]. The approach found in naturally evolved systems not only provides the relevant control parameters to the insects, but makes the process less intensive for their brain, which has limited computational capabilities. The transition of these efficient signal processing methods from the physiology and neuroethology domains to the robotics domain is made possible by translating the spatial decomposition routine into mathematical terms using a method termed as *Wide-Field Integration* (WFI) [42, 43, 44, 45]. Due to inherent simplicity of the algorithm it has been proven that a control system developed around the WFI technique can completely eliminate the need for dynamic estimation of absolute quantities by utilizing static output feedback of optic flow [46]. The algorithm has been successfully demonstrated on

ground and air borne vehicles to perform unmapped reflexive obstacle avoidance [47, 45, 8]. In this project, it has been demonstrated that WFI processing of an electric image yields relative proximity information of the perturbing objects which can be confined in a control theoretic framework to perform reflexive obstacle avoidance maneuvers.

1.3   Approach/Methods

This thesis focuses on extracting control-relevant information from electric images with low computational effort. For doing so, the approach proposed and taken is encapsulated below.

- Derive qualitative equations for computing electric images for a straight tunnel with conductive walls. These equations will be based on electrostatic principles due to their simplicity.

- Constitute a control strategy by deriving feedback laws for a straight tunnel with conductive walls.

- Assume that geometries that are more complex than a straight tunnel locally look like a straight tunnel.

- Perform robust analysis to get an idea of the stability of the controller with respect to variation of tunnel width.

- Evaluate the control strategy in simulations and experiments by applying the control strategy designed for a straight, conductive tunnel.

The direct implication of this approach will be the use of a common control strategy for variety of environments. Various combinations of object geometries and materials can then be used to form to test and evaluate the controller.

1.4   Contribution

The contributions of this research to the contemporary state-of-the-art are primarily a simple representation of electric images and an easier procedure to extract relevant proximity information from them. The detailed contributions are listed below.

- *Formulation of the Physics of Electrolocation*: Implemented the principles from electrostatics to compute electric images for our version of a bio-inspired electro-sensor.

- *Adaptation and Evaluation of WFI-based Algorithms*: Adapted the existing WFI technique into a numerical version to extract proximity information from distributed electric field potential patterns. Evaluated obstacle avoidance algorithms in simulation by processing electric images computed for simpler environment geometries.

- *FEM based simulations for complicated geometries*: Confirmed the working of the WFI-based sensing and obstacle avoidance routines in environments with complicated geometries using FEM generated electric images.

- *Creation of a sensor and signal processing scheme*: For hardware implementation, an electro-sensor and a signal acquisition and processing scheme were

designed to mimic an electric fish.

- *Experimental validation*: Validated the physical model of electrolocation and the control algorithm using a gantry system to autonomously navigate the electro-sensor between obstacles under water.

The following chapters categorically detail each of the above contributions.

1.5   Thesis Organization

The thesis is organized as follows. Chapter 2, derives electrostatics equations for electric images due to straight and circular walls using a technique called the *method of images*. An important set of equations for a straight tunnel is also derived in this Chapter.

Chapter 3, describes in detail the procedure to extract control-relevant information from electric images using the WFI method. We propose the use of two state extraction functions to compute the relative states of the electro-sensor with respect to an obstacle. A static feedback controller is designed to use these extracted relative states effectively to manipulate the motion of a robotic vehicle and to perform obstacle avoidance. The WFI algorithm was adapted to process the electric images by performing numerical integration of generally non-integrable equations that are encountered in this problem. The state-extraction functions and thus the entire analysis is derived for a straight tunnel with conductive walls. Simulation results are presented in order to demonstrate the use of the relative states in performing obstacle avoidance in environments with conductive obstacles of relatively simple

geometries.

Chapter 4, presents simulations in environments containing non-conductive obstacles. For this purpose, electric images are generated using the quasistatic approach found under finite element methods. This approach also allows the use of an oscillatory source to power the electric field of the electro-sensor, as opposed to a static source in the electrostatics case. Additionally, obstacle geometries can be made more complicated, thus enabling simulations of more realistic environment scenes.

Chapter 5, describes the presented analysis and simulations are validated experimentally. Effort was made to replicate environments similar to their simulation counterparts. The sensor design is maintained to be consistent with the design used for the electrostatic analysis. The experimental setup consists of a large glass water tank and an X-Y positioning gantry and an electro-sensor.

Chapter 6, contains concluding remarks and directions for future research for this project.

Chapter 2

Electrostatic Expressions for Electric Images

This chapter presents the electrostatic equations for electric images formed due
to the perturbation of an electric field from various environments like a straight
wall, a tunnel and a circular arena. An electro-sensor model motivated from the
electroreception system in fishes is used to formulate these equations. (For greater
insight into electrolocation in fishes, the reader is referred to [19, 48, 49, 50, 51, 52,
53].) Further, we take assistance of a well-known tool from electrostatics used to
simplify the electric field differential equations, called the *method of images*. There
are two main assumptions behind this analysis: all obstacles are conductive in nature
and the electric field source is static in nature. Although a non-oscillatory source
is rarely observed in nature, this treatment is considered here due the its inherent
accessibility and the convenience it presents in introducing the concepts of electric
image processing and control methodology.

Electric images of a fish need a complete electromagnetic analysis to capture
the effect of all the variables involved, which typically is a cumbersome task. How-
ever, for visualizing the nature and variation of the electric image due to perturbing
objects, it is easier to analyze them using electrostatics. Electrostatic analysis is not

a substitute for full electromagnetic study, but it is a faster way to understand the concept of electrolocation and to design controllers for robotic vehicles as performed in Chapter 3.

2.1   Electro-Sensor Model
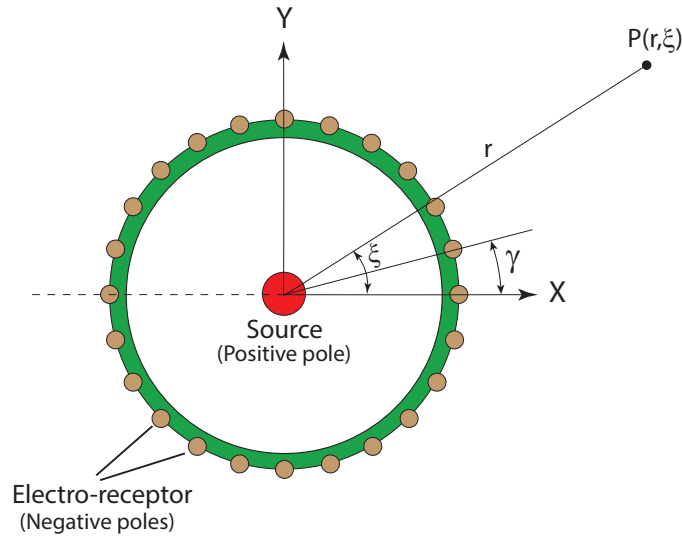
Figure 2.1: Model of electro-sensor used for electrostatics analysis

The sensor model assumed is shown in Figure 2.1. It consists of an electric multipole system with the source pole located centrally to a circular ring of radius R carrying m electro-receptors. The electro-receptors are modeled as small spherical electrodes and are distributed evenly along the ring. The centrally located source can be considered as the positive pole carrying a charge Q and the peripheral electro-receptors as negative poles, each possessing a charge $\frac{-Q}{m}$. The variables in an electrostatic potential equation at a point in a field of a known charge are the value of the charge itself and the distance between the point and the charge [54, 55].

14

On similar lines, the equation to evaluate the potential at a general point P, having a radial position (r_0, ξ), as shown in Figure 2.1, due to the multipole system of the sensor is thus the sum of the potentials due to all of the individual charges as given by Eq. (2.1) below, according to the superposition theorem [54, 55]:

$$V(r, \xi) = \frac{1}{4\pi\epsilon} \left(\frac{1}{r} - \sum_{k=1}^{m} \frac{Q}{mr_{e,k}} \right) \tag{2.1}$$

Here, r is the distance of point P from the source and $r_{e,k}$ is the distance of point P from each of the m electro-receptors. Subscript k iterates the equation for each of the m receptors. The presence of the factor m in the denominator in the second half of the right hand side of the equation comes directly from the value of the charge on each electro-receptor.

2.2 Method of Images

For a point charge in free space, electric field intensity and voltage potential at any point can be computed using Coulomb's Law and the work done against the field, respectively. But when an object is inserted in the field, both of the above computations become exceedingly difficult. The method of images is a tool in electrostatics that is useful in solving Coulomb's equation and the voltage differential (or integral) equation. It states that charges and surfaces are equivalent to a system of the charges and their corresponding images due to the surfaces only. The boundary conditions due to the surfaces are replaced by image charges and the effect of the surfaces is accounted for [55].

A popular example for explaining this concept is that of a point source placed

near a conducting wall. Consider a positive pole with charge Q at a position y from a straight conducting wall. The effect of the wall on the electric field of the pole can be reproduced by introducing another pole at a position $-y$ from the wall with opposite polarity. This secondary pole is called as image pole and is illustrated in Figure 2.2. The total potential at a point in space is expressed as the sum of those due to the source and the image poles as given by Eq. (2.2) below. The point of interest $P(r_0, \xi)$ is the location in space where the potential is computed.
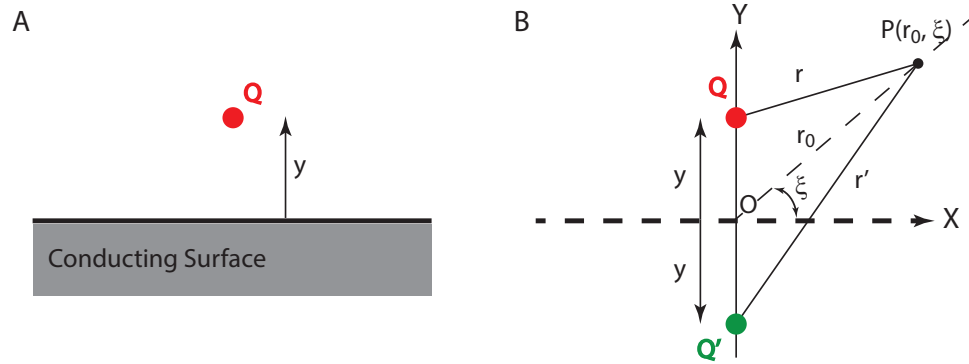
Figure 2.2: Method of images applied to the straight-wall problem. Red color stands for positive charge(s) and green color stands for negative charge(s).

$$V_{wall} = \frac{Q}{4\pi\epsilon} \left(\frac{1}{r} - \frac{1}{r'} \right) \tag{2.2}$$

Here, r and r' are the lengths $\bar{PQ}$ and $\bar{PQ'}$, respectively; they are equal to the 2-norm of the following vectors.

$$
\begin{aligned}
\boldsymbol{r} &= \begin{bmatrix} r_0 \cos(\xi) \\ r_0 \sin(\xi) \end{bmatrix} - \begin{bmatrix} 0 \\ y \end{bmatrix} \\
\boldsymbol{r'} &= \begin{bmatrix} r_0 \cos(\xi) \\ r_0 \sin(\xi) \end{bmatrix} + \begin{bmatrix} 0 \\ y \end{bmatrix}
\end{aligned}
\tag{2.3}
$$

16

This analysis holds for a general charged body of any shape provided the image has the same shape and geometry as that of the original body. Moreover, for conducting surfaces that are not planar, the analysis is still valid if certain modifications are made to the image, as demanded by the shape of the surface. Thus for a circular arena, a similar expression for potential can be derived. For a charge Q inside the arena, the image can be assumed to have formed outside the arena. This image will lie on the same radius vector of the arena on which the original charge is located, as illustrated in Figure 2.3.
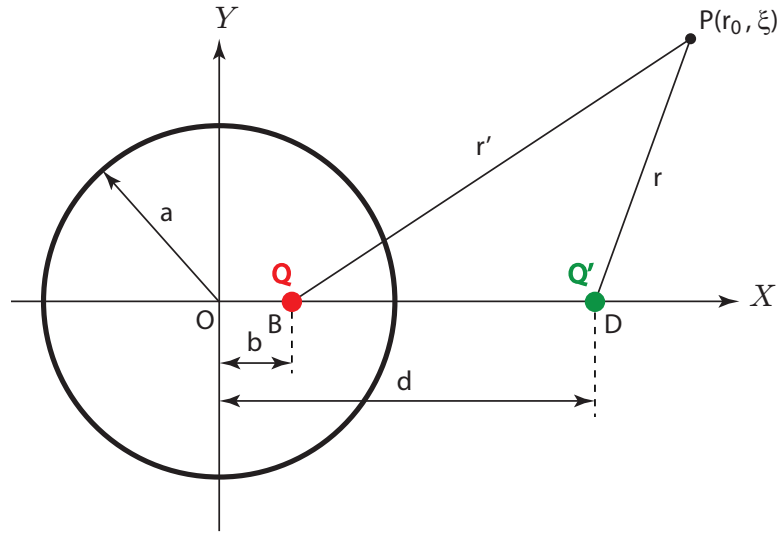
Figure 2.3: A multipole placed within a conducting circular arena.

Following analysis is obtained from [54, 55]. The image charge and its distance from the center of the arena are,

$$Q' = -\frac{a}{d}Q \qquad d = \frac{a^2}{b} \tag{2.4}$$

This means that the total voltage potential at point $P(r_0, \xi)$ is,

$$V_{sphere} = \frac{Q}{4\pi\epsilon\,r} + \frac{Q'}{4\pi\epsilon\,r'} \tag{2.5}$$

The variables r and r' are the distances of the pole from the point of interest as mentioned before and are the 2-norms of the following vector expressions.

$$
\begin{aligned}
\boldsymbol{r} &= \begin{bmatrix} r_0 \cos(\xi) \\ r_0 \sin(\xi) \end{bmatrix} - \begin{bmatrix} b \\ 0 \end{bmatrix} \\
\boldsymbol{r'} &= \begin{bmatrix} r_0 \cos(\xi) \\ r_0 \sin(\xi) \end{bmatrix} - \begin{bmatrix} d \\ 0 \end{bmatrix}
\end{aligned}
\tag{2.6}
$$

The reader is referred to [54, 55] for detailed derivations. The two examples provided in this Section prove to be the stepping stones for further analysis. The next section introduces the our sensor model.

2.3   Electric Image

An electric image is the modulation caused to the nominal spatial and temporal patterns of transdermal potentials of an electric fish due to the presence of an object near it. To introduce the mathematical expressions of electric image, consider the case of a single wall as shown in Figure 2.4A.

Assume a straight conducting wall at a position y relative to the center of the electro-sensor. Its effect on the electric field of the multipole can be reproduced by introducing another multipole at a position $-y$ and having opposite polarity. The secondary multipole is called an image multipole. The total potential at a point in space is the sum of those due to the source and the image multipoles as given by Eq. (2.7). The point of interest $P(r_0, \xi)$ is the location in space where the potential

18
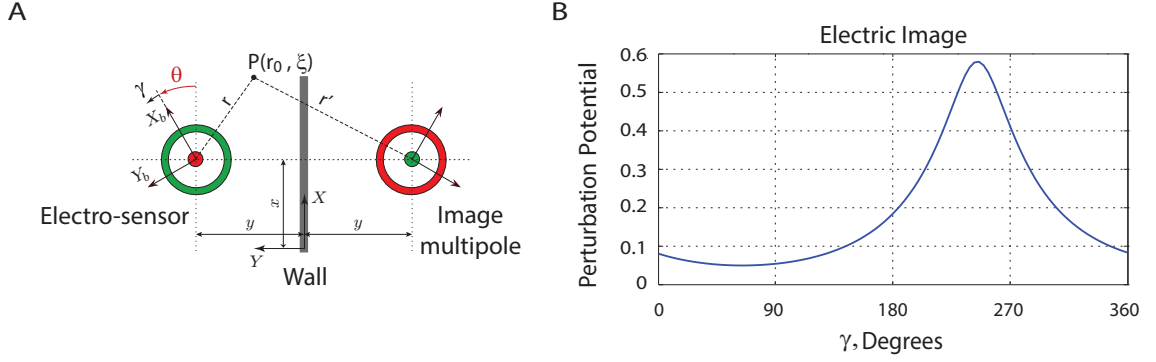
Figure 2.4: Electro-sensor multipole field perturbed by a straight wall. (A) The setup, (B) Electrostatic image formed

is computed. We have,

$$V_{wall}(\boldsymbol{q}, r, \xi) = \frac{Q}{4\pi\epsilon}\left[\frac{1}{r} - \frac{1}{r'} - \frac{1}{m}\sum_{k=1}^{m}\left(\frac{1}{r_{e,k}} - \frac{1}{r'_{e,k}}\right)\right] \tag{2.7}$$

Here, r and $r_{e,k}$ are the distances of $P(r_0, \xi)$ from the source and the m electro-receptors on the sensor, respectively. The distances r' and $r'_{e,k}$ pertain to the image multipole and are the counterparts of r and $r_{e,k}$. The subscript k above is stands for the image of the kth, $k = 1, ..., m$ electro-receptor. The variable m in the denominator of the summation term on the right hand side of the equation comes from the charge on each electro-receptor which is assumed to be $-Q/m$.

In the presence of a wall, two additional independent variables are included in the equation for electric image: the lateral offset, y, and orientation, θ, with respect to the wall. These two variables can be grouped as $\boldsymbol{q} = (y, \theta)$ giving the pose of the sensor with respect to the wall. It is assumed that the coordinate system is located on the wall with the positive X-axis directed forward along the wall and the positive Y-axis perpendicular to the wall so that the Z-axis is directed out of the plane of the

19

paper. The sensor is located at (x, y) with respect to the origin of the coordinate system. The distances, r, $r_{e,k}$, r' and $r'_{e,k}$ can be derived by computing the 2-norms of the following vector expressions.

$$
\begin{aligned}
\boldsymbol{r} &= \begin{bmatrix} r_0 \cos(\xi) \\ r_0 \sin(\xi) \end{bmatrix} - \begin{bmatrix} x \\ y \end{bmatrix} \\[2ex]
\boldsymbol{r}_{e,k} &= \boldsymbol{r} - \begin{bmatrix} R \cos\left(\frac{2\pi(k-1)}{m} + \theta\right) \\ R \sin\left(\frac{2\pi(k-1)}{m} + \theta\right) \end{bmatrix} \\[2ex]
\boldsymbol{r'} &= \boldsymbol{r} - \begin{bmatrix} 0 \\ -2y \end{bmatrix} \\[2ex]
\boldsymbol{r'}_{e,k} &= \boldsymbol{r'} - \begin{bmatrix} R \cos\left(-\frac{2\pi(k-1)}{m} - \theta\right) \\ R \sin\left(-\frac{2\pi(k-1)}{m} - \theta\right) \end{bmatrix}
\end{aligned}
\tag{2.8}
$$

In the above equations, $\gamma_k = \frac{2\pi(k-1)}{m}$ gives the locations of the electro-receptor $k = 1, ..., m$. The field of the source multipole is perturbed by the wall, the effect of which is replicated by introducing the image multipole, i.e., the effect on the source field is the field perturbation. Hence the potential due to the image multipole computed at the locations of the electro-receptors on the sensor gives the following expression for the electric image of a straight wall:

$$
\Phi_{wall}(\boldsymbol{q}, \gamma) = \frac{Q}{4\pi\epsilon} \left[\frac{1}{m} \sum_{k=1}^{m} \left(\frac{1}{r'_{e,k}} \right) - \frac{1}{r'} \right]
\tag{2.9}
$$

The variable Q stands for the magnitude of the total charge on the electro-receptors, thus giving the magnitude of the charge on each of the m electro-receptors as Q/m. Q is also the charge on the source pole of the multipole. This expression gives the value of the perturbation potential Φ at each of the m electro-receptors on the

20

electro-sensor located at a azimuthal spacing of γ between each other. The dependence of the electric image on γ is explicit from the expressions for the distances $r'_{e,k}$ and r' which are computed as given by Eq. (2.8) with the values for r_0 and ξ computed at the electro-receptors using the vector expression:

$$r_0 = \begin{bmatrix} R\cos(\gamma + \theta) \\ R\sin(\gamma + \theta) \end{bmatrix} + \begin{bmatrix} x \\ -y \end{bmatrix} \tag{2.10}$$

Figure 2.4B above shows the electric image for a particular pose where the vehicle is directed towards the wall. With an increase in the distance y, the magnitude of the electric image decreases. On varying the orientation of the sensor with respect to the wall, the peak of the electric image is shifted along the electro-receptors linearly. The variation in electric image with the lateral and angular offsets are illustrated in Figure 2.5A&B respectively. The offsets mentioned here are with respect to the wall or the coordinate system mentioned above.
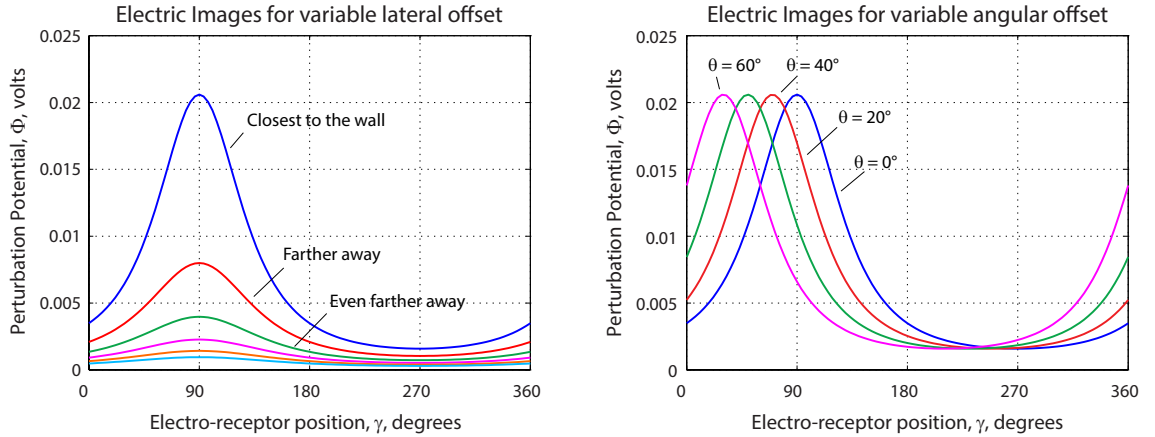
Figure 2.5: Variation of electric image due to a straight wall. (A) Effect of change in lateral offset, (B) Effect of change in angular offset.

2.3.1 Electric Image in a Straight Tunnel

The straight-tunnel case is a direct extension of the straight-wall problem. Hence, to study the electrostatics of a straight tunnel we introduce a second wall to the straight-wall case. Due to the inherent symmetry of the environment, the origin of the coordinate frame is shifted to the centerline of the tunnel. Proceeding with the straight-wall analysis, the boundary conditions imposed by the two walls are satisfied by one image multipole associated with each wall. But each image multipole will introduce one new boundary condition due the wall farther from it. So another set of two images arises due to each image in the first set. The process of formation of new image multipoles for satisfying the boundary conditions is repeated infinitely many times, which results in the formation of subsequent images. (It is analogous to placing an object in between two parallel mirrors to obtain an infinite number of mirror images.) Thus, when the electro-sensor is introduced between a set of parallel conducting walls, the method of images analysis leads to the formation of an infinite number of image multipoles as shown in Figure 2.6.
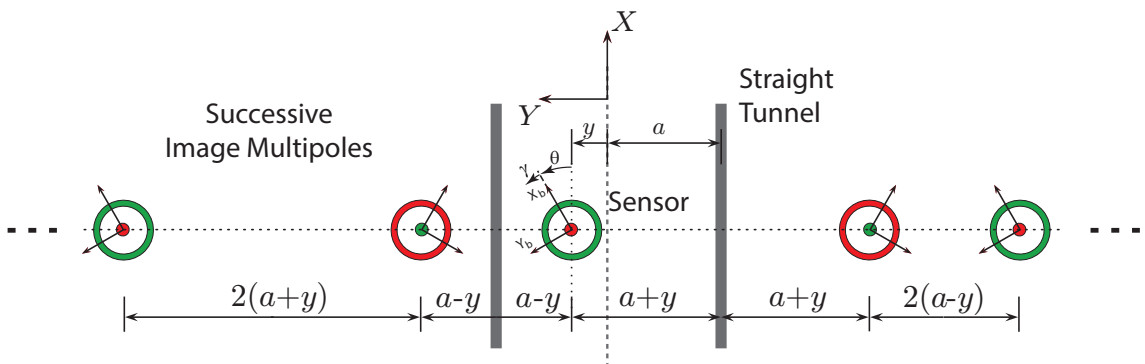
Figure 2.6: Electro-sensor introduced in a straight tunnel forming an infinite series of images.

It is assumed that the X-axis is aligned along the centerline of the tunnel and directed forward, while the Y-axis is perpendicular to the centerline. The sensor is located at coordinates (x, y). The images can be divided into two groups so that all the images in a group have the same orientation. One of the groups contains all image multipoles with the same heading as that of the source multipole; this group is assigned the subscript a and the other group is assigned the subscript b. The total potential at point $P(r_0, \xi)$ due to all of the image multipoles and the source multipole is,

$$V_{tunnel}(\boldsymbol{q}, r, \xi) = V + V' \tag{2.11}$$

As is the case with the single wall formulation, non-primed variables denote quantities due to the source multipole, whereas primed variables give the terms due to the image multipoles. Thus V' is the contribution due to the image multipoles. Both terms on the right-hand side of the above equation are defined as:

$$V = \frac{Q}{4\pi\epsilon}\left[\frac{1}{r} - \frac{1}{m}\sum_{k=1}^{m}\frac{1}{r_{e,k}}\right] \tag{2.12}$$

$$V' = \frac{Q}{4\pi\epsilon}\sum_{l=1}^{\infty}\left[\frac{1}{m}\sum_{k=1}^{m}\left(\frac{1}{r'_{b,e,k,l+}} + \frac{1}{r'_{b,e,k,l-}} - \frac{1}{r'_{a,e,k,l+}} - \frac{1}{r'_{a,e,k,l-}}\right)\right.$$
$$\left. - \left(\frac{1}{r'_{b,l+}} + \frac{1}{r'_{b,l-}} - \frac{1}{r'_{a,l+}} - \frac{1}{r'_{a,l-}}\right)\right] \tag{2.13}$$

The summation index k in Eq. (2.12) and Eq. (2.13) iterates over all of the m electro-receptors on source multipole and the image multipoles. The index l in Eq. (2.13) iterates all all of the infinite image multipoles. Only the first few of the infinite image multipoles are needed to provide satisfactory accuracy in the computed value of the potentials. As before, the terms r, $r_{e,k}$, $r'_{a,k,l+}$ etc. are the distances of point

P from multipole centres and receptors. The subscripts contain extra information about the particular multipole considered. Subscript e, k stands for electro-receptors and denote that the particular distance is measured between point P and the kth electro-receptor on that multipole. Subscripts a and b stand for the set of image multipoles as described earlier. All the image multipoles are considered to have formed on a line parallel to the Y-axis. The additional subscripts $l+$ and $l-$ stand for the lth image formed on the positive or negative side of the Y-axis. Thus, $r'_{a,e,k,l+}$ stands for the distance between point P and the kth electro-receptor on the lth image multipole that belongs to the set a of images and is formed on the positive Y-axis. Similarly, $r'_{b,l-}$ is the distance of point P from the center of the lth image multipole that belongs to the set b and is formed on the negative Y-axis. The distances in Eq. (2.12) and Eq. (2.13) are the 2-norms of the vector expressions given below:

$$
\boldsymbol{r} = \begin{bmatrix} r_0 \cos(\xi) \\ r_0 \sin(\xi) \end{bmatrix} - \begin{bmatrix} x \\ y \end{bmatrix}
$$

$$
\boldsymbol{r}_{e,k} = \boldsymbol{r} - \begin{bmatrix} R \cos\left(\frac{2\pi(k-1)}{m} + \theta\right) \\ R \sin\left(\frac{2\pi(k-1)}{m} + \theta\right) \end{bmatrix}
$$

$$
\boldsymbol{r}'_{a,l+} = \boldsymbol{r} - \begin{bmatrix} 0 \\ 4al \end{bmatrix}
$$

$$
\boldsymbol{r}'_{a,l-} = \boldsymbol{r} - \begin{bmatrix} 0 \\ -4al \end{bmatrix}
$$

$$
\mathbf{r}'_{b,l+} = \mathbf{r} - \begin{bmatrix} 0 \\ 2(a-y) + 4a(l-1) \end{bmatrix}
$$

$$
\mathbf{r}'_{b,l-} = \mathbf{r} - \begin{bmatrix} 0 \\ -2(a+y) - 4a(l-1) \end{bmatrix}
$$

$$
\mathbf{r}'_{a,e,k,l+} = \mathbf{r}'_{a+} - \begin{bmatrix} R\cos\left(\frac{2\pi(k-1)}{m} + \theta\right) \\ R\sin\left(\frac{2\pi(k-1)}{m} + \theta\right) \end{bmatrix}
$$

$$
\mathbf{r}'_{a,e,k,l-} = \mathbf{r}'_{a-} - \begin{bmatrix} R\cos\left(\frac{2\pi(k-1)}{m} + \theta\right) \\ R\sin\left(\frac{2\pi(k-1)}{m} + \theta\right) \end{bmatrix}
$$

$$
\mathbf{r}'_{b,e,k,l+} = \mathbf{r}'_{b+} - \begin{bmatrix} R\cos\left(-\frac{2\pi(k-1)}{m} - \theta\right) \\ R\sin\left(-\frac{2\pi(k-1)}{m} - \theta\right) \end{bmatrix}
$$

$$
\mathbf{r}'_{b,e,k,l-} = \mathbf{r}'_{b-} - \begin{bmatrix} R\cos\left(-\frac{2\pi(k-1)}{m} - \theta\right) \\ R\sin\left(-\frac{2\pi(k-1)}{m} - \theta\right) \end{bmatrix}. \tag{2.14}
$$

The perturbation potential recorded at the electro-receptors on the sensor constitutes the electric image. In this case, the perturbation due to the tunnel walls has been replaced by the image multipoles. Hence the electric image is the potential due to the image multipoles computed at the electro-receptors on the sensor and is given as,

$$
\Phi_{tunnel}(\mathbf{q}, \gamma) = V' \tag{2.15}
$$

For computing the electric image, V' is computed at the electro-receptor locations

γ. The values for r_0 and ξ in V' in Eq. (2.13) can be computed using:

$$ \boldsymbol{r}_0 = \begin{bmatrix} R\cos(\gamma + \theta) \\ R\sin(\gamma + \theta) \end{bmatrix} + \begin{bmatrix} x \\ y \end{bmatrix} \tag{2.16} $$

The tunnel electric image is similar in shape to that obtained in the straight-wall case. It tends to decrease in magnitude when the sensor is moved towards the centerline and the peak tends to shift laterally with the change in inclination θ. Additionally, the peak is formed on the region of the sensor that is closest to either of the walls. Similar to a straight wall, the electric image for a tunnel requires the knowledge of the pose of the sensor $\boldsymbol{q} = (y, \theta)$ with respect to the centerline of the tunnel. The variation in electric image with the lateral and angular offsets are illustrated in Figures 2.7A&B, respectively.
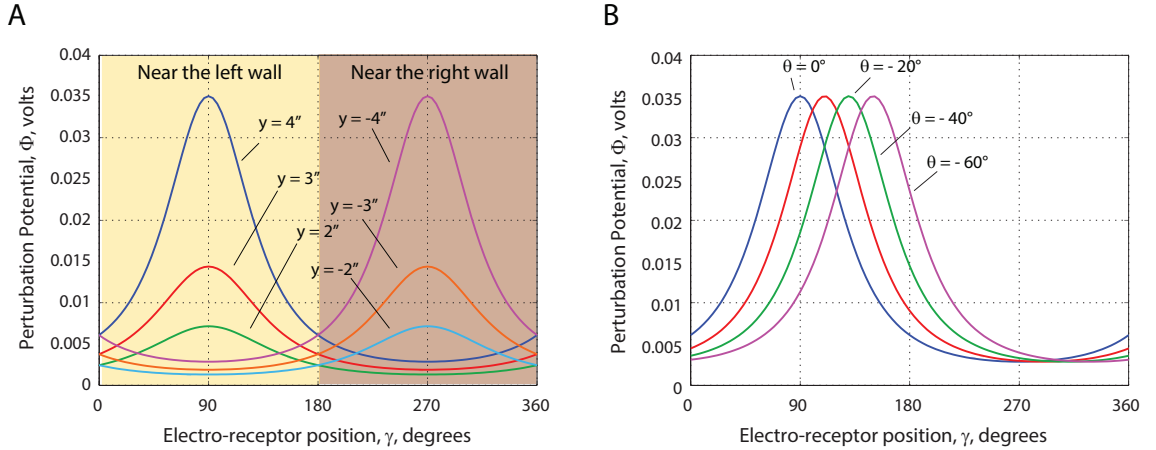
Figure 2.7: Variation of electric image in a 12 inch wide tunnel. (A) Effect of change in lateral offset, (B) Effect of change in angular offset.

26

2.3.2 Electric Image in a Circular Arena

The expression for the electric image in a circular arena is presented here to provide a complete procedure of formation of electric images using the method of images. The curvature of the arena shapes the equations in this problem. These equations are derived only for simulating wall-following behavior in such an environment. Experimental validation or FEM based simulations for this environment have not been performed.

Consider a circular arena of radius a within which a multipole is placed at a radial distance b from the center. As before, the source of the multipole carries a charge Q and each electro-receptor carries a charge equal to $-Q$. The coordinate system is assumed to have its origin at the center of the arena. Without loss of generality, assume the multipole is located on the radius vector of the arena along the X-axis as shown in Figure 2.8.
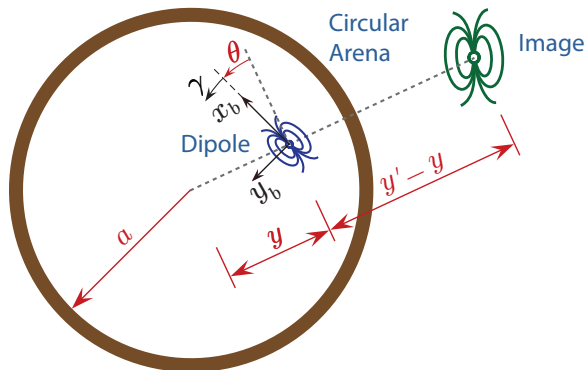
Figure 2.8: Electro-sensor in a circular arena.

Recall, an image of a pole with a charge Q is formed at a distance $d = \frac{a^2}{b}$ from the center of the arena and has a charge $Q' = -\frac{a}{d}Q$. The image of the central

pole of the multipole has a charge Q'. It is formed on the same azimuth as the original multipole at a distance d from the center of the arena. Each of the images of the m electro-receptors will have a charge $-Q'/m$. These images will be formed at distances proportional to the distances of the corresponding electro-receptors of the original multipole according to the relation between b and d above. The image multipole does not have a pole located exactly at the center of the ring of electro-receptor images, due to the curvature of the arena. Following Eq. (2.17) gives the expressions for the position vectors of the central poles and the electro-receptors of both the original and the image multipole:

$$
\begin{aligned}
\boldsymbol{\rho} &= \begin{bmatrix} b \\ 0 \end{bmatrix} \\
\boldsymbol{\rho}' &= \begin{bmatrix} \frac{a^2}{b} \\ 0 \end{bmatrix} \\
\boldsymbol{\rho}_{e,k} &= \boldsymbol{\rho} + \begin{bmatrix} R\cos\left(\frac{2\pi(k-1)}{m} + \theta\right) \\ R\sin\left(\frac{2\pi(k-1)}{m} + \theta\right) \end{bmatrix} \\
\boldsymbol{\rho}'_{e,k} &= \frac{a^2}{||\boldsymbol{\rho}_{e,k}||^2}\boldsymbol{\rho}_{e,k}
\end{aligned}
\tag{2.17}
$$

The actual distances of all the poles are the 2-norms of these position vectors.

The expressions for distances of the point $P(r_0, \xi)$ from the source as well as

image multipole can be derived as in Eq. (2.18). We have

$$
\begin{aligned}
\boldsymbol{r} &= \begin{bmatrix} r_0 \cos(\xi) \\ r_0 \sin(\xi) \end{bmatrix} - \boldsymbol{\rho} \\
\boldsymbol{r}_{e,k} &= \boldsymbol{r} - \boldsymbol{\rho}_{e,k} \\
\boldsymbol{r}' &= \begin{bmatrix} r_0 \cos(\xi) \\ r_0 \sin(\xi) \end{bmatrix} - \boldsymbol{\rho}' \\
\boldsymbol{r}'_{e,k} &= \boldsymbol{r}' - \boldsymbol{\rho}'_{e,k}
\end{aligned}
\tag{2.18}
$$

The expression for total potential is given by the sum of the contributions due to the source and the image multipoles, i.e., $V_{tunnel}(\boldsymbol{q}, r, \xi) = V + V'$, where,

$$
\begin{aligned}
V &= \frac{Q}{4\pi\epsilon} \left[\frac{1}{r} - \frac{1}{m} \sum_{k=1}^{m} \frac{1}{r_{e,k}} \right] \\
V' &= \frac{Q}{4\pi\epsilon} \left[\frac{1}{r'} - \frac{1}{m} \sum_{k=1}^{m} \frac{1}{r'_{e,k}} \right]
\end{aligned}
\tag{2.19}
$$

Finally, the electric image for a circular arena is,

$$
\Phi_{arena}(\boldsymbol{q}, \gamma) = V',
\tag{2.20}
$$

when computed at the locations of the electro-receptors on the source multipoles.

Chapter 3 delineates the procedure to extract relative states from the electric image equations using Wide-Field Integration processing. The relative states are then used to design the closed-loop control system that carries out autonomous navigation tasks.

Chapter 3

Wide-Field Integration and Autonomous Control

This chapter discusses the entire procedure to extract relevant information from electric images in the form of relative states using the electro-sensor model and the equation for electric image in a tunnel from Chapter 2. Wide-Field Integration (WFI) processing decomposes electric images into useful quantities contain the desired state information of the vehicle carrying the sensor. Optimal values of relative states are computed in order to form the feedback input to the vehicle actuation system. Simulations showing centering in a tunnel and wall-following behavior in a circular arena demonstrate the working of the signal processing routine and the controller. Finally, the robustness of the controller when the tunnel width is different from the nominal value is proven by providing a μ-analysis based argument.

3.1   Wide-Field Processing of Electric Images

Insects perceive their visual fields in the form of the relative speed of the environment with themselves instead of absolute distances of objects, a phenomenon called *optic flow*. Farther objects tend to move slower in comparison to closer objects, thus setting up a speed/distance relationship. For avoiding collisions with closer objects,

it is imperative to move away from fast-moving visual fields towards slow-moving fields. With a limited brain-size, it is necessary for these organisms to process optic flow efficiently. WFI is a mathematical analogue of the processing of optic flow by the tangential cells in insects [56].

For a planar tunnel geometry, an insect aligns with the centerline of the tunnel by equalizing the optic flow in their visual fields. The nominal optic flow pattern is generated during translation along the centerline of the tunnel. This pattern is roughly sinusoidal [45], with the peak and the trough sections indicating the presence of a wall on either side of the insect. The equal magnitude and zero spatial phase shift of the peak and the trough indicate that the walls are at an equal distance from the insect and parallel to its heading, respectively. A lateral offset from the centerline of the tunnel increases one half of the optic flow pattern while the other half diminishes. An angular offset produces a phase angle shift. Inner products of such perturbed patterns with appropriate basis functions increase or decrease in value accordingly. Thus, WFI can extract relevant information from the optic flow perturbations in the form of lateral or angular offsets.

There is no evidence that electric fish use this approach to extract information about their environments from electric images. However, electric images with the multipole model considered in Section 2.3 exhibit amplitude modulation and phase shift properties that can similarly provide lateral and angular offsets in a planar tunnel. Let F_i represent the ith basis function used to decompose the electric image to yield the ith WFI output v_i. The WFI equation for extracting similar information

31

from electric images is,

$$v_i(\boldsymbol{q}) = \langle \Phi(\boldsymbol{q}, \gamma), F_i(\gamma) \rangle \tag{3.1}$$

Recall from Figure 2.6, in a tunnel, small angular and lateral offsets from the centerline produce low frequency spatial changes in electric images. So low frequency harmonics of an electric image can capture all the information of the offsets that produce such changes in the electric image. Fourier basis functions are chosen for all the subsequent analysis due to their simplicity of implementation. Hence the functions F_i are selected to be $F_1 = \cos(\gamma)$, $F_2 = \sin(\gamma)$, $F_3 = \cos(2\gamma)$, $F_4 = \sin(2\gamma)$ and so on. The inner product for a continuous function, $f(\boldsymbol{x}, \gamma)$ with $g(\gamma)$ for $L_2[0, 2\pi]$ (space of a square-integrable function, integrable over the bounded interval $0, 2\pi$]) is,

$$h(\boldsymbol{x}) = \int_0^{2\pi} f(\boldsymbol{x}, \gamma) \, g(\gamma) \, d\gamma$$

The corresponding inner product relevant to this problem is obtained by substituting the electric image Φ for function f and various basis functions for function g. The basis functions can follow any orthonormal basis for $L_2[0, 2\pi]$. The above inner products are the projections of the electric image on the basis functions. These projections are responsible for decomposing the electric image in the desired direction of the basis function. To numerically integrate the electric image Φ, the integral is replaced with a summation, yielding the expression for WFI outputs,

$$v_i(\boldsymbol{q}) = \sum_{\gamma=0}^{2\pi} \Phi(\boldsymbol{q}, \gamma) \, F_i(\gamma) \, \delta\gamma$$

The above equation is supplied with a set of electric images computed for discrete poses on either side of the centerline. For instance, a possible set of lateral displace-

32

ments is $Y = \{y| - a/2 \leq y \leq a/2\}$ and $\Theta = \{\theta| - \pi/4 \leq \theta \leq \pi/4\}$.

The objective is to implement a linear or a computationally simple estimator to derive the vehicle states from electric images. Values on both the sides of the centerline are necessary for the linearization of the WFI outputs, $v_i(\boldsymbol{q})$. The WFI outputs were linearized in terms of the states $\boldsymbol{q} = [y, \theta]^T$ about the centreline of the tunnel, the desired steady state condition $\boldsymbol{q}_0$, using the multivariable Taylor series,

$$v_i(\boldsymbol{q}) \approx v_i(\boldsymbol{q}_0) + \nabla \boldsymbol{q}|_{\boldsymbol{q}_0} \cdot (\boldsymbol{q} - \boldsymbol{q}_0) \tag{3.2}$$

The gradient operator operates on a matrix of values of $v(\boldsymbol{q})$; it is numerically implemented using the five-point central finite difference formula for each variable. The constant terms arising from the 1st term in Eq. (3.2) are small enough to be neglected. In matrix form, Eq. (3.2) resemble the linear equation, $v = C\,\boldsymbol{q}$, which has the form of the output of a linear system:

$$\begin{bmatrix} v_1 \\ v_2 \\ \vdots \\ v_n \end{bmatrix} = \begin{bmatrix} C_{1y} & C_{1\theta} \\ C_{2y} & C_{2\theta} \\ \vdots & \vdots \\ C_{ny} & C_{n\theta} \end{bmatrix} \begin{bmatrix} y \\ \theta \end{bmatrix} \tag{3.3}$$

The matrix C contains the linearization coefficients of the Fourier harmonics with the sensor in its desired steady-state pose. For centering in a tunnel, the desired pose is when the sensor is perfectly aligned with the centerline and directed forward along it. C_y and C_θ provide the linearized Fourier coefficients to form linear combinations of the states $\boldsymbol{q} = [y, \theta]^T$.

3.2 Relative State Estimation

In this Section, the procedure to extract control relevant information from WFI outputs is described. The states computed using the formulation presented here are static in nature as opposed to dynamic. The approach of relative state estimation has the advantage of low computational effort and fast processing, as will be evident from the following formulation. The relative states of the system can be estimated by inverting $v = C\,\boldsymbol{q}$ as in Eq. (3.3). The residual errors in computation of the WFI equation from Eq. (3.3) with these state estimates is given as $e = v - C\boldsymbol{q}$, where v is the set of measured WFI outputs whereas $C\boldsymbol{q}$ is the set of estimated WFI outputs. The optimal solution that minimizes the summed squares of the residual errors given by the cost function $J = \frac{1}{2}e^T e$ is obtained from the principle of least squares [57],

$$\boldsymbol{q} = (C^T\,C)^{-1}\,C^T\,v \tag{3.4}$$

The matrix $C^\dagger = (C^T\,C)^{-1}\,C^T$ is the pseudo-inverse of the matrix of linearization coefficients C. The states estimated by Eq. (3.4) are not absolute states; they represent the sensor pose relative to the obstacles causing the perturbations to the electric field.

For n WFI harmonics, m electroreceptors and j states, the dimensions of C are $n \times j$, $C^\dagger$ is $j \times n$ and Φ is $m \times 1$. The set of Fourier harmonics F consists of n harmonics denoted by F_i, $i = 1, ..., n$, each having the dimensions $1 \times m$. Further examination of Eqs. (3.1–3.4)reveals that the pseudo inverse $C^\dagger$ can be pushed inside the inner product to form a compound term $C^\dagger\,F_i$ as shown below:

$$\begin{aligned} \boldsymbol{q}_j &= C_{ij}^{\dagger} v_i &&= C_{ji}^{\dagger} \langle \Phi, F_i \rangle \quad i = 1, ..., n \\ \boldsymbol{q}_j &= \left\langle \Phi, \sum_{i=1}^{n} C_{ji}^{\dagger} F_i \right\rangle && \end{aligned} \tag{3.5}$$

The state-estimation procedure is summarized by Algorithm 1.
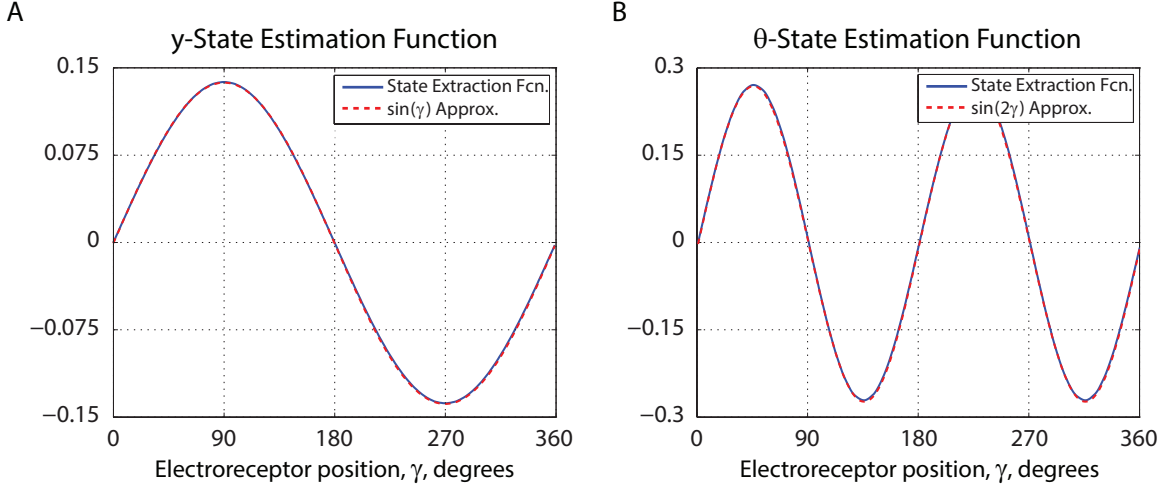
Figure 3.1: Optimal state extraction functions. (A) y-extraction function, (B) θ-extraction function.

The advantage of Eq. (3.5) is that the relative states $\boldsymbol{q} = [y, \theta]^T$ are estimated directly from the electric image Φ [46]. The functions $\sum_{i=1}^{n} C_{ji}^{\dagger} F_i$ used to estimate the states are *locally optimal state extraction functions*, henceforth called state extraction functions. For use with electric images, the state extraction functions resemble $\sin(\gamma)$ for y-estimation and $\sin(2\gamma)$ for θ-estimation. The $y-$ and $\theta-$ state extraction functions overlaid with their respective sinusoidal approximations are shown in Figure 3.1A and B respectively. These functions are pertinent to a conducting tunnel for which the inner products in Eq. (3.5) were numerically computed.

Algorithm 1: Relative State Estimation

Input: Electric images for different poses in a straight conductive tunnel,

$$\Phi = V'$$

. **Output**: Optimal state extraction matrix, $C^\dagger$

. **begin**

Compute a set of complex potentials for a tunnel, for various combinations

of lateral offset y and orientation θ with respect to the tunnel centreline.

for *Lateral offset $y \in Y$* **do**

    for *Orientation $\theta \in \Theta$* **do**

        $\boldsymbol{q} = (y, \theta), \quad \gamma = [0, 2\pi].$

        Numerically integrate to compute the inner products

        $v_i(\boldsymbol{q}) = \langle \Phi(\boldsymbol{q}, \gamma), F_i(\gamma) \rangle$ to obtain Fourier harmonics $a_0(\boldsymbol{q})$, $a_1(\boldsymbol{q})$,

        $b_1(\boldsymbol{q})$ etc.

Numerically linearise the harmonics about the desired steady state

condition.

Assemble the linearised WFI output equation $v = C\boldsymbol{q}$.

Find the pseudo-inverse of the matrix C using linear least squares

principle as $C^\dagger = (C^T C)^{-1} C^T$.

Estimate the states of the sensor at any location in a tunnel, relative to

the steady state condition, by performing the operation

$\boldsymbol{q}_j = \left\langle \Phi, \sum_{i=1}^n C_{ji}^\dagger F_i \right\rangle.$

3.2.1 Discussion

In the absence of any object, the electric image is equal to zero at all electro-receptor positions. When the sensor is introduced in a straight tunnel, a peak is developed in the electric image. The inner product of such an electric image with $\sin(\gamma)$ will be positive if the peak is in the $\gamma = (0, \pi)$ range and will be negative if the peak is in the $\gamma = (\pi, 2\pi)$ range. A peak is formed in the $\gamma = (0, \pi)$ range if the sensor is closer to the left wall or, in other words, a positive lateral offset is provided with respect to the centreline. Similarly, a peak in the $\gamma = (\pi, 2\pi)$ range indicates that the sensor is closer to the right wall as a negative lateral displacement is provided. Thus the sign of the inner product is indicative of the nature of the lateral offset provided. Additionally, the magnitude of the inner product is useful in judging the amount of lateral offset: a smaller magnitude corresponds to smaller offset and vice-versa. Along similar lines, the angular offset can be estimated by examining the inner product between an electric image and $\sin(2\gamma)$. When the sensor is traveling parallel to either of the walls, the peak of the electric image is formed symmetrically about the $\pi/2$ or $3\pi/2$ sensor depending on the side to which the closest wall is. Thus the inner product yields a zero output and we get the estimate for angle θ as zero. In the case when the sensor is directed into a wall closer to it, the peak is formed in one of the four quadrants. By computing the inner product, it is possible to find out the quadrant in which the peak of the electric image occurs. The value of the inner product is positive in the region where $\sin(2\gamma)$ has a positive polarity and is negative where the $\sin(2\gamma)$ function has negative polarity. The relative states

are employed in forming a feedback input to the system, as explained in the next section.

3.3   Static Output Feedback Control

In this section, a controller is designed to perform centering behavior in a straight tunnel and its robustness properties are checked for application in other similar environments. We assume a linearized unicycle-style kinematics model for the vehicle similar to [45]. The controller is required to be simple and easy to implement in order to consume limited computational capability. Due to the availability of the relative state estimates from the electric image, a natural choice of a controller is output feedback. The idea is to form the input from linear combination of the estimates using the desired gain values. On closing the feedback loop by utilizing the estimated relative states in Eq. (3.5), suitable motion commands can be supplied to the vehicle to perform obstacle avoidance. These commands will be equal to zero when the vehicle aligns with the desired steady state condition. Also, the characteristics of the trajectory like settling time, overshoot etc. can be modified by noting that the kinematic model of the vehicle is a second order system. Thus the two gains that are used to form the feedback input are in fact similar to stiffness and damping in a spring–mass–damper system.

3.3.1 Control Strategy for Centering Behaviors

The goal of WFI-based control is to navigate a sensing vehicle to the desired steady state condition. In a tunnel, the steady state condition is the centerline, heading straight ahead. For other corridor-like environments, the steady state condition is the line equidistant from the boundaries formed by the objects on the either side of the corridor.

The schematic for the control loop is shown in Figure 3.2. The optimal state
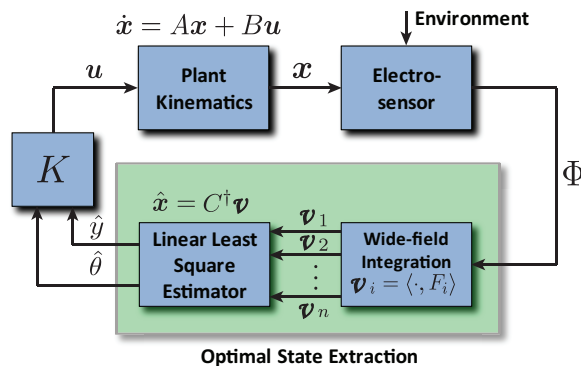
Figure 3.2: Feedback control system for performing obstacle avoidance

extraction operation in Eq. (3.5) is depicted by combining the WFI and the Linear Least Squares Estimator (LLSE) blocks together.

A planar linearized unicycle model is assumed for the vehicle kinematics, based on the behavioral observations of fish in general. The simplest maneuvers exhibited by fish in response to an obstacle consist of continued straight-line motion and a yawing action similar to a unicycle [58]. Coupled kinematics from other out of plane degrees of freedom are small enough to be neglected [58]. In addition, the non-holonomic constraint $\dot{x} \sin \theta - \dot{y} \cos \theta = 0$ is enforced so that the body-frame

velocities become $\dot{y}_b = 0$ and $\dot{x}_b = U$. This constraint prescribes a motion to the model such that there is no motion perpendicular to the vehicle X_b axis, thereby preventing side-slip motion. The unicycle kinematics in the inertial frame are

$$
\begin{aligned}
\dot{x} &= U \cos \theta \\
\dot{y} &= U \sin \theta \\
\dot{U} &= u_y \\
\dot{\theta} &= u_\theta
\end{aligned}
\tag{3.6}
$$

Here, u_y and u_θ are the control inputs provided to the plant.

For a vehicle having a constant forward velocity U, we have $\dot{U} = u_y = 0$ and the linearized open-loop kinematics are

$$
\begin{aligned}
\dot{x} &= U \\
\begin{bmatrix} \dot{y} \\ \dot{\theta} \end{bmatrix} &= \begin{bmatrix} 0 & U \\ 0 & 0 \end{bmatrix} \begin{bmatrix} y \\ \theta \end{bmatrix} + \begin{bmatrix} 0 \\ 1 \end{bmatrix} u
\end{aligned}
\tag{3.7}
$$

Here, the matrices can be put in a standard state space form to yield the matrices A and B as under.

$$
\begin{aligned}
A &= \begin{bmatrix} 0 & U \\ 0 & 0 \end{bmatrix} \\
B &= \begin{bmatrix} 0 \\ 1 \end{bmatrix}.
\end{aligned}
\tag{3.8}
$$

Output feedback is provided to the system using the control law $u_\theta = K \, [\hat{y}, \hat{\theta}]^T$, i.e.,

$$
u = K_y \, \hat{y} + K_\theta \, \hat{\theta}.
\tag{3.9}
$$

40

In the case of zero estimate error, i.e., $\hat{y} = y$ and $\hat{\theta} = \theta$, the closed-loop system is

$$\begin{bmatrix} \dot{y} \\ \dot{\theta} \end{bmatrix} = \begin{bmatrix} 0 & U \\ K_y & K_\theta \end{bmatrix} \begin{bmatrix} y \\ \theta \end{bmatrix} \tag{3.10}$$

As mentioned earlier, this is a second order system similar to a spring-mass-damper system. The characteristic equation for this closed loop system is $s^2 - s\,K_\theta - U\,K_y = 0$ and eigenvalues are given as $s_{1,2} = \frac{K_\theta \pm \sqrt{K_\theta^2 + 4U\,K_y}}{2}$. It is clear from the characteristic equation and the eigenvalues that K_y corresponds to the stiffness term while K_θ to the damping term. For the roots s to lie in the left half plane, we select $K_\theta < 0$ and $K_y < 0$. On further analysis it is revealed that $K_\theta^2 < |4U K_y|$ yields complex roots whereas $K_\theta^2 > |4U K_y|$ yields real roots. For $K_\theta^2 = |4U K_y|$, the meaningless solution of two unique and real roots is obtained. We selected the gains using $K_y = -\frac{K_\theta^2}{4U}$ (second condition above) so that real roots are obtained. Stability as well as the desired performance can be achieved by carefully selecting the value for K_y. Simulations with electrostatic images in some environments having simple geometries can be found later in this chapter as well as in previous work by the authors [59].

It is worth mentioning that the controller designed for a straight conductive tunnel with a half width $a = 6$ inches (15 cm) will be shown via simulationto work for environments made up of objects of different conductivities and geometries.

3.3.2 Robust Stability Analysis of the Controller

In this Section, we analyze the robustness properties of the designed controller. The controller is intended to perform satisfactorily in various environments. In a

straight tunnel, the controller is expected to work flawlessly as it is designed for such an environment. For environments with complex geometries, we assume that the obstacles look like local tunnels and hence the same controller can be implemented. This assumption is verified in the following study.

The C matrix is parametrized in terms of the tunnel width parameter a. Thus C matrices are computed for various tunnel widths. A curve can then be fit to all the values of each of the elements in the C matrix by assuming a suitable trendline. We use a power fit $Y = AX^B$ for this purpose. The resulting parametrized C matrix, which we call C matrix itself for convenience, is given below.

$$C = \begin{bmatrix} 3.66 \times 10^{-3}a^{-5.14} & 0 \\ 0 & 3.49 \times 10^{-5}a^{-5.16} \\ -4.33 \times 10^{-6}a^{-6.96} & 0 \\ 0 & -2.83 \times 10^{-8}a^{-7.22} \end{bmatrix} \tag{3.11}$$

The elements in the above matrix originate from the b_n Fourier harmonics of electric images. The a_n harmonics are negligible are hence not included. High frequency harmonics are not included as the values of successive harmonics decrease significantly, as can be seen from the coefficients of the elements in the C matrix above. As a result, only the first four b_n harmonics are found in the above parametrization. For performing the parametrization itself, the Curve Fitting Toolbox in MATLAB is used. The power fit is selected owing to the quality of fit it provides for the available data and the inherent simplicity of representing these fits as closed form equations. The options selected in the toolbox settings are `NonlinearLeastSquares`, `Bisquare` (for robust fits) and `Levenberg-Marquart` (curve fitting algorithm). This combina-

tion is found to give lowest residuals for the fits.

The Curve Fitting Toolbox also yields the 99% confidence bounds of the fits. Of all the data points 99% will always lie within these bounds. These bounds are useful in computing the allowed perturbations δ_n to each of the element in the C matrix given above. The δ_n bounds found for above fits are as shown below.

$$C_{1,1} \Rightarrow \delta_1 = \pm 0.5075$$

$$C_{2,2} \Rightarrow \delta_2 = \pm 0.0041$$

$$C_{3,1} \Rightarrow \delta_3 = \pm 0.0161$$

$$C_{4,2} \Rightarrow \delta_4 = \pm 0.0002 \tag{3.12}$$

If we assume that a 20% uncertainty exists in estimating each of the curve fit coefficients, then the corresponding element in the C matrix can be multiplied by a factor $(1 + 0.2\delta_n)$. The sign of δ_n is irrelevant in this formulation. The C matrix therefore changes to,

$$C = \begin{bmatrix} 4.03 \times 10^{-3}a^{-5.14} & 0 \\ 0 & 3.493 \times 10^{-5}a^{-5.16} \\ -4.34 \times 10^{-6}a^{-6.96} & 0 \\ 0 & -2.83 \times 10^{-8}a^{-7.22} \end{bmatrix}. \tag{3.13}$$

As expected, the C matrix does not change significantly due to the better quality of fits obtained using the settings mentioned above. Following this, we dissociate the tunnel width parameter a as $a_m + \Delta a$, where a_m is the nominal tunnel width for which the controller is intended for and Δa is the uncertainty in the tunnel width. The uncertainty in a is defined as the ratio $\frac{\Delta a}{a_m}$ or the change in tunnel width Δa with

respect to the nominal tunnel width, a_m. Similarly, the C matrix can be written as $C_m + \Delta C$, due to a_m and Δa above. The theoretical proofs for above procedure can be found in [60, 61]. C_m is given as,

$$C_m = \begin{bmatrix} 4.03 \times 10^{-3} a_m^{-5.14} & 0 \\ 0 & 3.493 \times 10^{-5} a_m^{-5.16} \\ -4.34 \times 10^{-6} a_m^{-6.96} & 0 \\ 0 & -2.83 \times 10^{-8} a_m^{-7.22} \end{bmatrix}. \quad (3.14)$$

ΔC is obtained by differentiating C with respect to a_m as follows.

$$\Delta C = \begin{bmatrix} -5.14 \times 4.03 \times 10^{-3} a^{-5.14} \frac{\Delta a}{a_m} & 0 \\ 0 & -5.16 \times 3.493 \times 10^{-5} a^{-5.16} \frac{\Delta a}{a_m} \\ 6.96 \times 4.34 \times 10^{-6} a_m^{-6.96} \frac{\Delta a}{a_m} & 0 \\ 0 & 7.22 \times 2.83 \times 10^{-8} a_m^{-7.22} \frac{\Delta a}{a_m} \end{bmatrix} (3.15)$$

Rearranging Eq. (3.15) we have,

$$\Delta C = \begin{bmatrix} -5.14 & 0 & 0 & 0 \\ 0 & -5.16 & 0 & 0 \\ 0 & 0 & 6.96 & 0 \\ 0 & 0 & 0 & 7.22 \end{bmatrix} \begin{bmatrix} \Delta a & 0 & 0 & 0 \\ 0 & \Delta a & 0 & 0 \\ 0 & 0 & \Delta a & 0 \\ 0 & 0 & 0 & \Delta a \end{bmatrix}.$$

$$\begin{bmatrix} 4.03 \times 10^{-3} a^{-5.14} & 0 \\ 0 & 3.493 \times 10^{-5} a^{-5.16} \\ 4.34 \times 10^{-6} a_m^{-6.96} & 0 \\ 0 & 2.83 \times 10^{-8} a_m^{-7.22} \end{bmatrix} \quad (3.16)$$

The first matrix in Eq. (3.16) is a matrix of weights, W, and the second matrix is the uncertainty matrix Δ. The remaining third matrix is the nominal matrix C_m

from Eq. (3.14). Substituting in $C = C_m + \Delta C$ we have,

$$
\begin{aligned}
C &= C_m + \Delta C = C_m + W\Delta C_m \\
\Rightarrow C &= C_m \left(I + W\Delta \right) \tag{3.17}
\end{aligned}
$$

For this C matrix an $M - \Delta$ structure can be formulated as prescribed by [60]. The robust stability of such a plant is guaranteed if and if the following condition is satisfied.

$$
RS \Leftrightarrow \mu \left(M(j\omega) \right) < 1, \qquad \forall \omega \tag{3.18}
$$

In the above equation μ is the structured singular value for the $M - \Delta$ form. It is found that this condition is satisfied an uncertainty in the tunnel width a,

$$
RS \Leftrightarrow \Delta \leq \frac{\Delta a}{a_m} = \frac{1}{7.3393} = 13.63\%. \tag{3.19}
$$

The following plot shows the variation of μ with respect to frequency. Analysis was
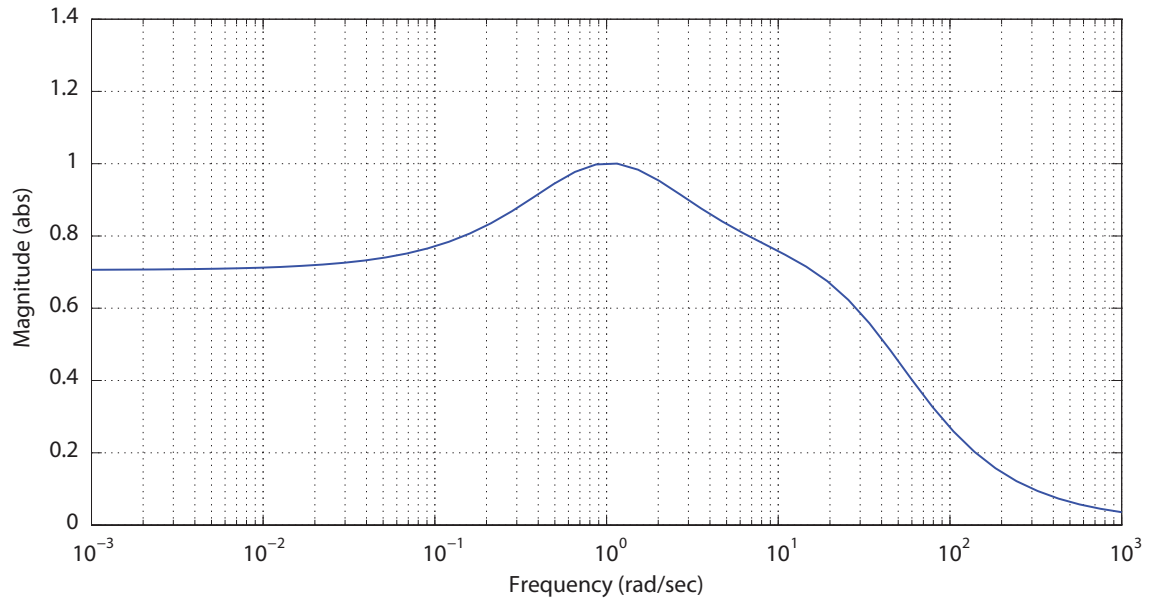
Figure 3.3: Variation of structured singular value, μ with respect to frequency.

performed to obtain similar plots for other uncertainty values for δ_1, δ_2, δ_3 and δ_4. In all the cases the allowed uncertainty was found to be almost the same. This is an indicator of the high accuracy of the curve fits.

Thus, the robust stability of the controller is guaranteed if the variation in tunnel width is less than 13.63% with respect to the nominal tunnel width a_m. This implies that the assumption of a local tunnel in place of objects with complicated geometries should hols as long as the lateral separation between them is less than 13.63% from the designed tunnel width. The simulations in the next section confirm the validity of this assumption.

3.4   Control Strategy for Wall Following Behaviors

The next objective is to manipulate a sensing vehicle in order to traverse a path along a wall (a circular arena or a straight wall) while maintaining a fixed distance from it. Here, we consider the desired steady state of the vehicle to be at the required offset from the wall and heading parallel to it.

For a circular arena, the steady state is achieved when the vehicle moves along a circle of radius equal to 80% of the arena radius and concentric to it. Thus the offset clause is met by traveling at a fixed distance of 20% of the radius from the wall and the parallel trajectory clause is met by traversing along a concentric circle. Consider the electric image equation for a circular arena given by Eq. (2.20). The procedure to find the state extraction functions is similar to those for the centering case in Section 3.3.1. As before, the state extraction functions are $\sin(\gamma)$ for estimating the

46

y-state and $\sin(2\gamma)$ for estimating the θ-state.

3.5   Simulation Results

This Section presents simulation results demonstrating obstacle avoidance in a straight tunnel and a circular arena using WFI processing and controller strategy explained in Sections 3.1–3.3. The basic assumption in these simulations is that the electric image is exactly given by the analytical equations given by Eq. (2.15) and Eq. (2.20). Thus, the estimated relative states are absolute and exactly correspond to the electric image. Another implicit assumption is the absence of sensor and actuator noise. The presence of such noise will corrupt the signal to some degree which will require additional filtering and signal processing, which is not performed here. We demonstrate centering response in a straight tunnel and wall-following behavior in a circular arena from multiple initial conditions.

3.5.1   Centering in a Straight Tunnel

In a straight tunnel, it is expected that the vehicle will eventually move away from walls and align itself with the centerline of the tunnel. We chose a 1 foot (30 cm) wide tunnel with conductive walls. Several starting locations and orientations were simulated in order to illustrate the response of the algorithm to variation in initial conditions. The state extraction functions for estimating the y and θ states were $\sin(\gamma)$ and $\sin(2\gamma)$ as prescribed in Section 3.2. The velocity U of the vehicle was assumed to be equal to 6 inches/sec (15 cm/sec). From Eq. (3.9) it can be seen
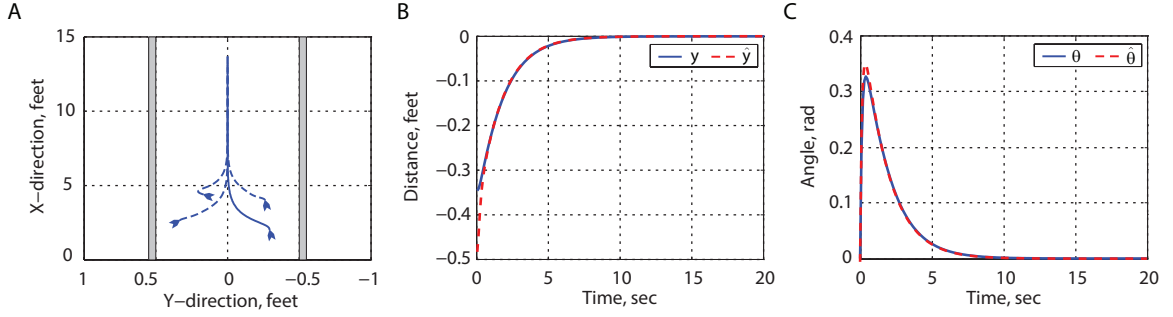
Figure 3.4: Simulations demonstrating centering behavior in a straight tunnel. (A) Trajectories, (B) Actual and estimated lateral offsets, y and $\hat{y}$,(C) Actual and estimated angular offsets, θ and $\hat{\theta}$.

that the feedback input is large when the vehicle has a larger offset with respect to the centerline of the tunnel (either a large lateral offset or a large angular offset). Thus, when the steady-state condition is achieved i.e., the vehicle is aligned with the centerline of the tunnel, the feedback input is equal to zero. Figure 3.4A shows the environment and the trajectories generated in the simulations. The arrows on each trajectory indicate the respective initial condition. Figure 3.4B plots the time traces of the relative $y-$estimates and the actual lateral offset y. Similar plots for the relative $\theta-$estimate and the actual angular estimate θ are plotted in Figure 3.4C. These traces correspond to the solid line trajectory in Figure 3.4A.

Observe that irrespective of the initial conditions the desired steady state is achieved eventually. The response to the obstacles depends on the gain values selected, thus deciding the values for overshoot, settling time and oscillations of the trajectory about the steady state. The selected gains provide a consistent performance with negligible overshoot and less setting time. The gains for forming the

48

feedback input u_θ were selected using a trial and error procedure to be $K_y = -20$ and $K_\theta = -40$. Convergence of trajectories is observed along the steady-state condition within the first few seconds. This behavior suggests the usefulness of the WFI-based control strategy in corridor-like environments.

3.5.2 Wall Following in a Circular Arena

Similar to the straight tunnel case, simulations were performed to demonstrate wall following behavior in a circular arena of diameter 3.3 feet (1 m) using the control strategy described in Section 3.4. The vehicle was expected to align with a circular trajectory of 2.6 feet (0.8 m) diameter, concentric to the arena. Consistent with the straight-tunnel case, multiple initial conditions were considered. The linear offsets in this case were defined with respect to the steady state circular trajectory, whereas the angular offsets were defined with respect to the perpendicular to the radius vector on which the vehicle is located at the particular instance. The controller tries to drive these offsets (states) to zero. This condition set by the controller was automatically satisfied when the vehicle traveled along the steady state trajectory. Figure 3.5A shows the trajectories originating from different initial conditions. The arrowheads on each trajectory indicate the initial conditions. In all the cases, it was observed that the controller successfully drove the vehicle to the desired steady-state condition. The gains $K_y = -20$ and $K_\theta = -40$ were selected by trial and error to limit the trajectory overshoot and settling time. The forward velocity of the vehicle was 6 inches/sec (15 cm/sec). If allowed to continue, all the trajectories
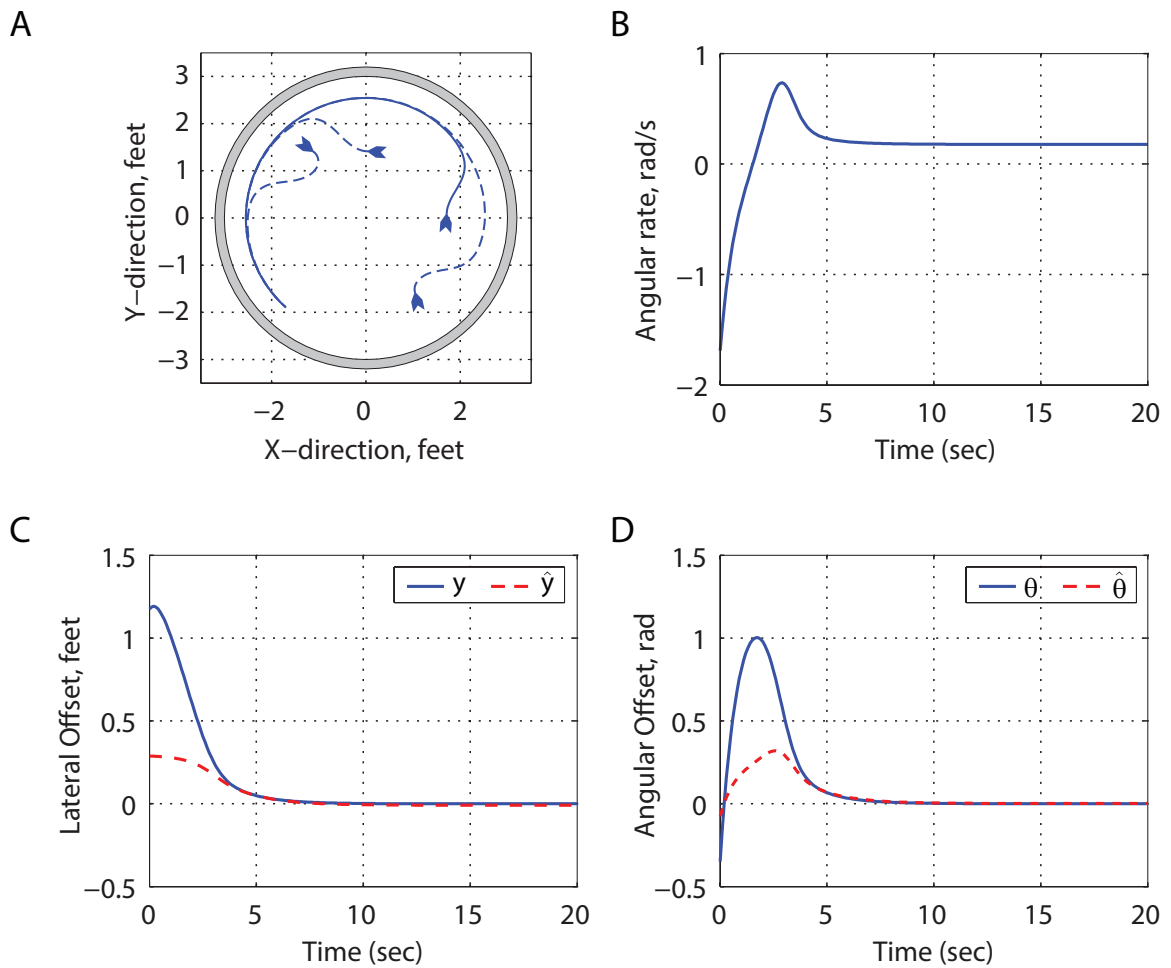
Figure 3.5: Simulations demonstrating wall following behavior in a circular arena. (A) Trajectories, (B) Angular rates, (C) Actual and estimated lateral states, y and $\hat{y}$, (D) Actual and estimated angular states, θ and $\hat{\theta}$.

continue along the circular trajectory. Figure 3.5B shows the time trace of the angular velocity of the vehicle. The vehicle shows high angular rate in the beginning which corresponds to the window when the vehicle approaches the desired steady state offset from the wall rapidly. Once the vehicle has aligned itself with this offset trajectory, the angular velocity is held constant to continue along the circular path. The steady state offset observed here is due to this reason. Figures 3.5C shows the time traces of actual and estimated lateral offset of the vehicle. Similarly, the time traces for the actual and the estimated angular offsets are shown in Figure 3.5D. In both the plots showing the offsets, the vehicle states and the state estimates converged when the steady state condition was attained.

3.6 Modifications for Non-conductive Objects

The entire algorithm discussed thus far is based on the premise that the perturbing objects are conductive in nature. Electric images due to such objects exhibit positive peaks. According to [26] the electric images due to similarly sized non-conductive objects is negative in polarity as compared to that due to a conductive objects. In addition, these electric images are smaller in magnitude (nearly half) than their conductive counterparts. There is also a phase shift in time involved in non-conductive electric images due to their capacitive qualities [19]. However the phase-shift property is not considered in this work.

3.6.1 Non-conductive Obstacles

To produce control inputs from electric images of negative polarity and reduced magnitude, it is required to negate the gains K_y and K_θ in Eq. (3.9) and increase their magnitudes. This negation does not however destabilize the system. The state extraction functions used are the ones that were derived for metallic corridors. These functions hence yield negative state estimates from the negative electric images of non-conductive objects. Thus by using negative gains the sign of the control input is guaranteed to have the right sign as in the metal corridor case. This approach is however only valid for environments constructed entirely out of non-metallic objects. When there is mix of conductive and non-conductive obstacles, a different strategy is used as shown next.

3.6.2 Mix of Conductive and Non-conductive Objects

This analysis is relevant for FEM simulations and experiments. The electric image has a definite positive peak for conductive objects and negative peak for non-conductive objects. The controller, with prescribed gains, can be used as defined by Eq. (3.9) when all the objects are positive, whereas negated gains as explained above can be used when all the objects are non-conductive. For environments with a mix of these two types of objects, the same controller cannot be used directly. This is because the controller needs to decide from the electric image, whether the obstacle was conductive or non-conductive and apply appropriately signed gains. It can be possible to do this by looking at the signs of the peaks of the electric

images. In simulations, where noise is assumed to be absent, the electric images of small or distant objects possess the right polarities for the peaks. So it is possible to use this method to tell the two types of materials apart, in that case. However, in experiments, with noise corrupting low magnitude signals due to small or distant objects, this method may or may not work. So a more robust method is sought.

The absolute value of an electric image due to a conductive object will look similar to that of a non-conductive object as is depicted in Figure 3.6. The procedure in Algorithm 1 to determine the state extraction function from the absolute-valued electric images can still be followed. In this procedure, absolute values of electric images of a conductive tunnel are used. State extraction functions so obtained extract states from electric images due to either conductive or non-conductive objects. It is known from [26], that electric images due to non-conductive objects are about half the magnitude of those due to conductive objects. Thus the above state extraction functions will yield lower state estimates for non-conductive objects. Note the pro-
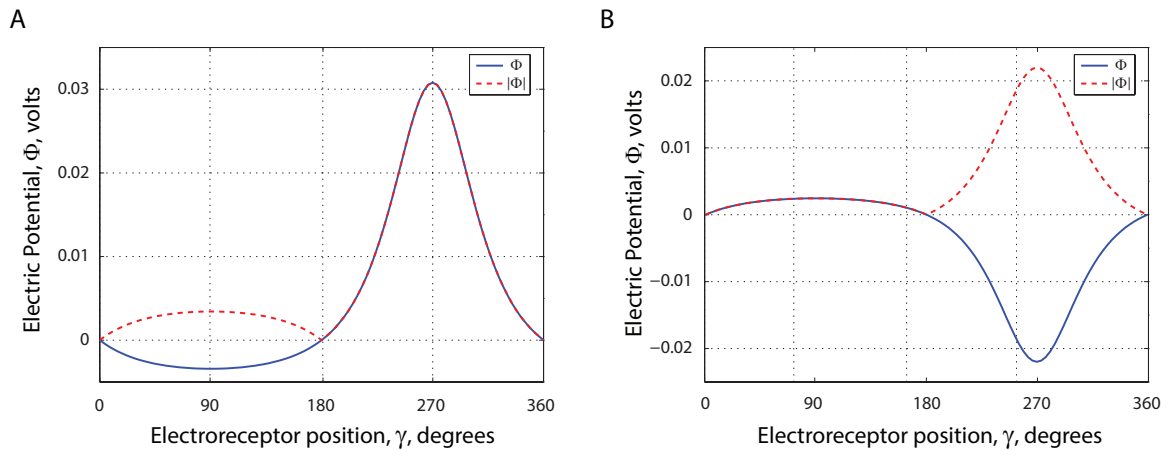
Figure 3.6: Absolute values of electric images. (A) Conducting objects, (B) Non-Conducting objects

cedure is expected to yield state extraction functions with higher frequency content in them due to the presence of the discontinuity at the zero crossing. The state extraction functions for this mixed environment case are plotted in Figure 3.7. The
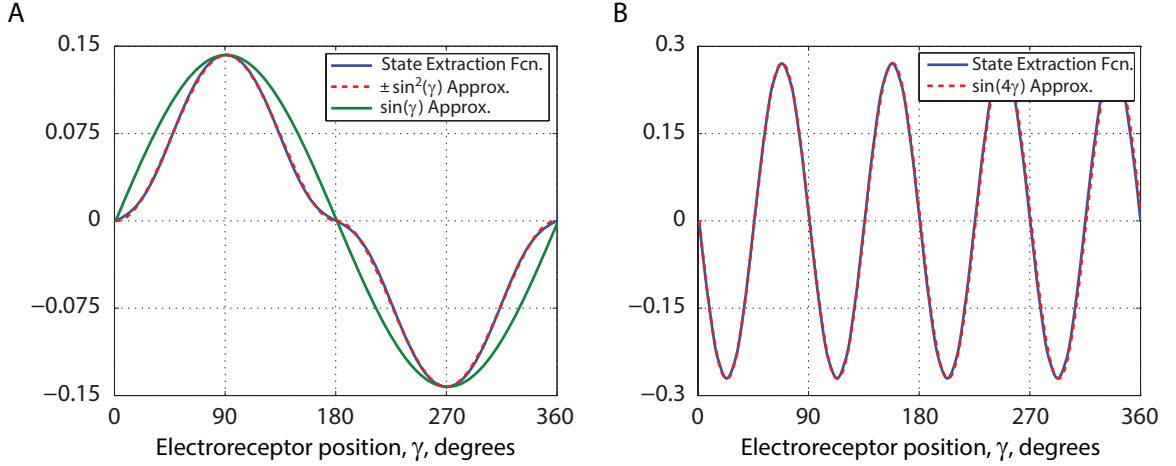
Figure 3.7: Optimal state extraction functions for mixed conductivity environments. (A) y-extraction function, (B) θ-extraction function.

state extraction function for the y state, shown in Figure 3.7A can be approximated by a $\sin^2(\gamma)$ for $0 \leq \gamma < \pi$ and $-\sin^2(\gamma)$ for $\pi \leq \gamma < 2\pi$ or by the sum of sines of higher frequencies. We use an approximation for this function given by $\sin(\gamma)$. The $\sin(\gamma)$ approximation has the advantage that it provides a stronger response near small angles to accelerate the vehicle to the steady state faster. The θ state estimation function involves higher frequencies and is given by $\sin(4\gamma)$ as shown in Figure 3.7B.

Consider the linearized unicycle kinematics in Eq. (3.10). As before, for the mixed tunnel case the characteristic equation for the closed loop system is $s^2 - s\,K_\theta - U\,K_y = 0$ and eigenvalues are given as $s_{1,2} = \frac{K_\theta \pm \sqrt{K_\theta^2 + 4U\,K_y}}{2}$. The signs of

the relative states estimated in this case are the same as their exact counterparts. So to the same argument that was true for selecting the gains in the conductive tunnel case holds for this problem as well, i.e., $K_\theta < 0$ and $K_y < 0$ for stability. Further, the gains are selected using $K_y = -\frac{K_\theta^2}{4U}$ so that real valued roots are obtained and desired performance is achieved.

The advantage of using this approach is that, it is not required to distinguish between conductive and non-conductive materials. Direct application of these state extraction functions to absolute-valued electric images yields the required states irrespective of the nature of the perturbing object. In the following chapters, more complex simulation problems and experiments are presented in order to demonstrate the usefulness of the control strategy. These problems will test the algorithm against change in material properties, shape of objects and complexity of the environment. In all of these problems, the control strategy developed in this chapter is used.

Chapter 4

Quasistatic Analysis and Simulations

This chapter describes simulation problems for demonstrating reflexive obstacle avoidance in unmapped environments of complicated geometries. Such geometries are comprised of multiple, staggered obstacles that are either conductive or non-conductive. In addition, the source of the electro-sensor is made oscillatory for achieving a higher degree of bio-mimicry. For solving the obstacle-avoidance problem in such environments, the control method developed in Chapter 3 is used.

4.1   Motivation

The control strategy in Chapter 3 navigates a sensing vehicle in a straight tunnel with conductive walls. In more realistic situations, the environment can be lined with complex-shaped objects of different conductivities. Electrostatics falls short on two counts in analyzing these situations. Firstly, electrostatics cannot handle non-conductive objects very efficiently. Secondly, method of images type analysis for a complex shaped object is extremely difficult. In order to compute electric images in such a case, a full electromagnetic analysis by solving the general Maxwell's equations in Table 4.1 can be performed. But doing so is almost always a very

tedious assignment. There are methods to solve the problems involving dielectric walls and slabs. So potentially solving such a problem could possibly yield an analysis similar to the method of images analysis in Chapter 2. However, there are quite a few issues involved in this approach.

The most common method involves solving an integral called Sommerfeld's formula [62, 63]. Such integrals are generally impossible to solve either analytically or numerically due to their oscillatory nature. Some solutions that have been proposed by making some crucial asymptotic assumptions are still very oscillatory and slow converging. This is not a favorable situation if such computations are to be performed during simulations involving multiple iterations. Another popular method to solve electromagnetic problems is by using Green's functions. This has been demonstrated in many works like [64, 65, 66]. However, with the addition of boundary conditions and singularities, the solution of a Green's function gets complicated and computationally heavy. All such methods involve the electric field as the solution. To arrive at the electric potential, which is the variable of interest, the gradient equation $E = -\nabla \Phi$ is to be solved. Here, E is the electric field and Φ is the potential. Integrating a 3D gradient equation is generally a difficult task. Moreover, such an intensive computation where the solution is computed for the entire spectrum of wavelengths is not required in our case. This work attempts to mimic the electrolocation observed in wave-type electric fish, which produce low frequency quasi-sinusoidal electric fields. Hence, the full electromagnetic approach is not pursued.

So to simulate obstacle avoidance in such environments, a different approach

is required. Finite Elements Methods (FEM) for quasistatic problems tends to address all of the shortcomings of electrostatics mentioned previously while avoiding the cumbersome approach of a full electromagnetic study. FEM tools provide the ability to model objects of complex shapes and assign to them different electrical properties. The prime objective of this project is to mimic electrolocation in electric fish. Electrostatics, with a static electric field source, is not the absolute way to explain electrolocation. With FEM through quasistatic analysis it is possible to consider a sinusoidally varying source, which is a very close approximation of the electric field source in electric fish. Hence, the quasistatic approach is consider here.

If the velocity of propagation of the source electromagnetic wave is negligible with respect to the speed of light, then the problem can be treated as a quasistatic problem and the time variance of the current density in Maxwell's equations can be neglected [55]. Table 4.1 shows the comparison between the general Maxwell's electromagnetic equations and quasistatic versions of them. The notation used

Table 4.1: Comparison of Maxwell's general and quasistatic electric field equations

	General Maxwell's equations	Quasistatic field equations
Faraday's Law	$\nabla \times \mathbf{E}(r,t) = -\frac{\partial \mathbf{B(r,t)}}{\partial t}$	$\nabla \times \mathbf{E}(r,\omega) = -j\omega\mathbf{B}(r,\omega)$
Ampere's Law	$\nabla \times \mathbf{H}(r,t) = \mathbf{J}(r,t) + \frac{\partial \mathbf{D}(r,t)}{\partial t}$	$\nabla \times \mathbf{H}(r,\omega) = \mathbf{J}(r,\omega) + j\omega\mathbf{D}(r,\omega)$
Gauss's Law	$\nabla \cdot \mathbf{D}(r,t) = \rho_v(r,t)$	$\nabla \cdot \mathbf{D}(r,\omega) = \rho_v(r,\omega)$
No monopoles	$\nabla \cdot \mathbf{B}(r,t) = 0$	$\nabla \cdot \mathbf{B}(r,\omega) = 0$

in the general Maxwell's equations is the standard one, where $\mathbf{E}$ is the electric field intensity, $\mathbf{B}$ is the magnetic flux density, $\mathbf{H}$ is the magnetic field intensity,

$\mathbf{J}$ is the current density, $\mathbf{D}$ is the electric flux density and ρ_v is the (volumetric) charge density. In general, all the quantities in the general Maxwell's equations are arbitrary functions of position r and time t, and hence time-dependent. For quasistatic equations, we assume that the quantities evolve sinusoidally in time and are functions of r and the frequency of the sinusoid ω. The relation between $\mathbf{B}$ and $\mathbf{H}$ and $\mathbf{D}$ and $\mathbf{E}$ are given by the constitutive relations,

$$\mathbf{B} = \mu\mathbf{H}$$
$$\mathbf{D} = \epsilon\mathbf{E} \tag{4.1}$$

More explanation can be found in [55]. Additionally, in quasistatic field equations $j = \sqrt{-1}$ and ω is the frequency of the sinusoidally varying source electric field.

It can be seen that the general Maxwell's equations are grossly simplified due to the assumption that the electric field is produced by a source varying sinusoidally at low frequencies. Due to these simplifications, the quasistatic equations behave similar to their static counterparts by satisfying Laplace's and Poisson's equations. Further, many methods and ideas that are valid for electrostatics problems, which are otherwise void for electromagnetic problems defined by the general Maxwell's equations, can be extended to the quasistatic equations. Thus in our case, the quasistatic approximation not only simplifies the problem, but is a good way to mimic electrolocation in fishes by including a slowly varying electric field.

For implementation in simulations, the process of solving the quasistatic Maxwell's equations is required to be quick and fairly accurate. Hence an FEM-based approximation using ANSYS was used to solve the problem and generate the electric images.

The quasistatic electric images resemble electrostatic images with the additional ability to resolve objects of different materials into conductive or non-conductive. For in-depth study of electromagnetic principles, the reader is referred to [55, 54].

4.2   Finite Elements Analysis

Finite Elements Analysis is a tool to find approximate solutions to boundary value problems for differential equations. The solution is found using numerical methods by solving for small subdomains making up the entire domain of the problem. The equations solved for the subdomains are simpler than the differential equation that applies to the entire domain as a whole. The final result is obtained by systematically combining, or performing a summation of the results of all the subdomains. We used the ANSYS program to perform these simulations. The FEM simulation process involves the following steps.

- Modeling the geometry

- Meshing

- Application of loads and boundary conditions

- Solution and postprocessing

Here, all these steps are explained in the context of the quasistatic simulations performed to demonstrate electrolocation.

4.2.1   Modeling of geometry

The environments in which the obstacle avoidance is performed either consist of straight tunnels or a corridor constructed from complex-shaped objects or a structured obstacle field. All commercially available FEM tools possess a capability to draw shapes either by defining the geometry or by providing coordinates of points on the boundary of the objects. Thus geometrically simpler obstacles like straight walls and circles were drawn accordingly. But when complex shaped objects were involved, a different approach was used. A bitmap image file was drawn for such environments. A MATLAB script was used to extract the coordinates of the points on the boundaries of the objects. These coordinates were then input to the FEM program to form the environment. Three different environments, shown in Figures
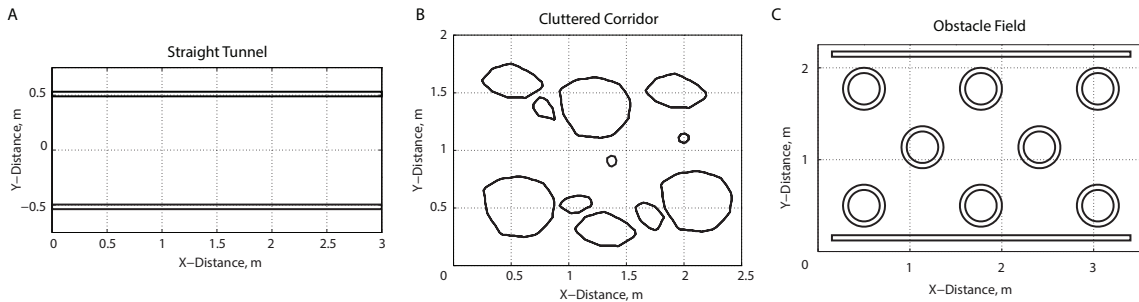
Figure 4.1: Different environments used for simulations. (A) Straight tunnel, (B) Cluttered corridor, (C) Obstacle field.

4.1A–C were modeled in ANSYS for performing the simulations. The first environment was a basic straight tunnel (Figure 4.1A), the second one contained a cluttered corridor (Figure 4.1B) and the third one had an obstacle field of cylinders (Figure 4.1C). For each type of environment, three cases were considered wherein the con-

ductive properties of the objects were changed. The first case was designed to have all the obstacles to be conductive, the second case with all non-conductive objects and the third with a mix of conductive and non-conductive objects.

After drawing the geometries of the environment and obstacles, different regions are assigned material properties. The three materials that have been considered in these simulations are detailed in Table 4.2 below. Relative permittivity of a

Table 4.2: Materials used in simulations

Material name	Relative Permittivity, ϵ_r	Loss Tangent, $\tan\delta$	Application
Water	80	5.542×10^{-8}	The environment
Aluminum	1.3×10^{14}	3×10^{12}	Conductive obstacles
Wood	5	0.04	Non-conductive obstacles

material defines its degree of conducting an electric field in comparison to vacuum. Loss tangent, on the other hand, is the property that defines a material's rate of dissipation of electromagnetic energy. As can be seen from the table, metals possess very high permittivity and high loss tangent values as compared to non-metals. Loss tangent is convenient in that it relates the conductivity and the permittivity of a material with the wave frequency [55]. Both, relative permittivity and loss tangent depend on the frequency of the wave. We have considered the values for these variables at 100 Hz, which is the desired frequency of our electric field source in simulations. These two material properties are sufficient for ANSYS to perform quasistatic analysis.

4.2.2 Meshing the environment

Meshing the environment splits it into discrete elements which obey the same differential equations as the entire environment. However, due to some simplifications and assumptions made during splitting the environment, it is possible to apply a simplified set of equations to each element in lieu of the original more complicated equations. On connecting the solutions obtained for all the elements, an approximate solution to the complete domain is obtained. The accuracy of the approximate solution depends on the average size of the segments or the quality of the meshing: The smaller the size, the more accurate the solution, in general.

Thus, meshing forms a very important part in the FEM procedure. Ideally, it is desirable to make the mesh size or the element size as small as possible to arrive at an accurate solution. This kind of a mesh is called a fine mesh. However, this approach has some limitations. Smaller element size implies more elements. Consequently, more computations are to be performed, which makes the entire process slow and computationally very demanding. However, making the mesh coarse sacrifices the accuracy of the solution. Therefore, there should be a good compromise between the number of elements and the desired accuracy of the solution. There are various mesh-size optimization algorithms that are useful in computing the right degree of meshing [67, 68, 69]. In contrast, a brute force approach of local refinement of a coarse mesh is also very popular [70, 71]. (The popularity of this approach is also due to the availability of this capability built into most commercially available FEM software like ANSYS.) The three scenarios mentioned above are depicted in Figure
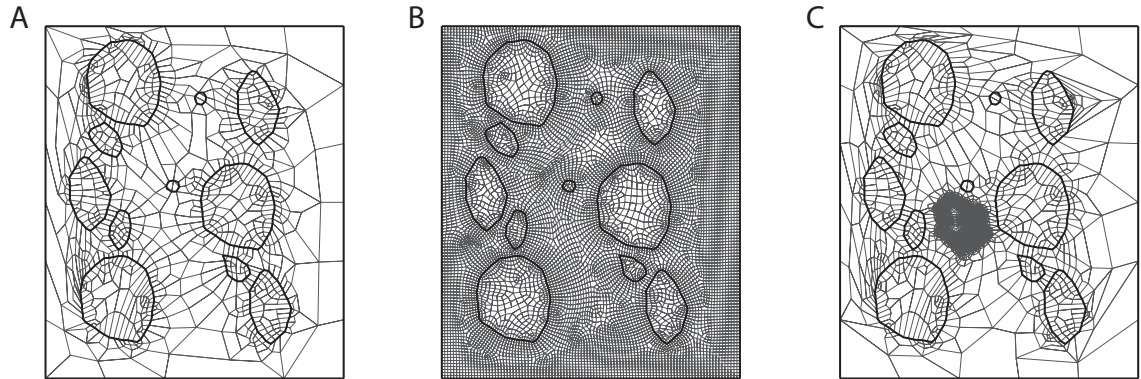
Figure 4.2: Mesh quality choices for simulations. (A) Coarse mesh, (B) Fine mesh, (C) Locally refined mesh.

The approach of local mesh refinement is used here where the mesh is refined in the prime region of interest, i.e. in the vicinity of the sensor. The electric image is computed at the sensor and, with a refined mesh, the accuracy of the solution is increased. The remaining regions with a coarse mesh yield a less accurate solution. However, these regions contribute little towards the electric image. In fact, the less computational effort required for obtaining the solutions in these regions is a very desirable quality.

4.2.3   Application of Loads and Boundary Conditions

An FEM problem consists of the environment and the load set applied for specified boundary conditions. These load sets in electromagnetic problems typically include voltages, charges, currents, magnetic fields etc. Whereas, boundary conditions include the materials and geometry of objects in the environments and impedance of

the contact surfaces between different objects in the environment.

In most commercially available FEM software, the boundary conditions can be set through built-in tools. The assignment of materials and geometry to the objects in the environments was explained in the previous two steps. In addition to these, contacts are created between water and all the objects, as required by ANSYS. ANSYS provides the required tool to do so. The contacts were configured to have high conductivity or very low impedance for both conductive and non-conductive objects. Doing so ensures computing the correct effect of the electric field on both type of objects.

In the simulations in this work, the load applied was of the voltage type. The source of the multipole is defined as a 3 volt peak-to-peak, 100 Hz, sinusoidally varying voltage waveform. In addition, the outermost boundary of the environment is grounded by the program by default. This boundary condition does not affect the simulation since the boundaries of the environment are maintained sufficiently far from the objects to avoid their effect on the electric field of the sensor.

The three steps mentioned so far are grouped under a process called preprocessing.

4.2.4   Solution and Postprocessing

Once the preprocessing steps are carried out, the simulation is ready to be solved. On issuing the solve command, ANSYS solves the quasistatic problem as per the variables defined during preprocessing, like mesh size, loads, contacts etc. Depending

on the mesh size the solution time varies. As is true with any FEM program, ANSYS performs successive iterations to arrive at a solution by minimizing the relative error. It does so by combining solutions for all the elements starting from the outermost elements to the innermost elements and vice versa in alternate iterations. The theory governing this procedure can be found in any standard FEM textbook [72, 73].

Voltages at all the element nodes are obtained as the solution to the simulated problem. The values at the nodes in the vicinity of the source are of particular interest. The fine mesh size in this region is important for converging to accurate solutions. The values at the locations of the electro-receptors are computed by interpolating within the set of the nodal values in their vicinity. By concatenating voltage values at all the electro-receptors, the required electric image is obtained. On implementing the WFI processing and controller subroutines using the simulated electric images, the next position of the sensor is computed. This new position is computed with the objective of moving the sensor to a position where the perturbations on both the sides of the sensor are equalized.

4.2.5   Linking of ANSYS with MATLAB

To automate the process of FE simulation discussed above, it was felt necessary to bypass the ANSYS GUI and perform the tasks. In addition, this was meant to be done iteratively to perform autonomous navigation in such environments. The signal processing and control loop were implemented in MATLAB for the electrostatics study and it was decided to port the same code to the quasistatic simulations.

Owing to these reasons, ANSYS and MATLAB were operated jointly.

ANSYS is capable of running batch files that are written in the ANSYS programming language. A Macro was written in MATLAB to perform the tasks listed below.

- Write an ANSYS batch file.

- Send the file to ANSYS server.

- Send an instruction to the ANSYS server to run the batch file

- Interpolate the nodal solutions at the positions of the electro-receptors to obtain the electric image.

- Relay the electric image back to MATLAB for further processing.

The simulations are carried out in the background thus saving a plenty of computational resources.

4.3   Simulation Results

Four environments, namely straight tunnel, variable width corridor and an obstacle field, are used in simulations. The objective in all the simulations is to navigate within the obstacle while avoiding all the collisions. The following results for different test cases show composite figures containing the trajectories, the time traces of actual states and the relative state estimates. For some problems, the time traces of body velocities in the inertial frame are plotted as well. Trajectories due to different initial conditions are included. The time traces are plotted for the case for

which the trajectory is plotted using a continuous line. The arrowheads at the beginning of each trajectory indicate the initial conditions, position and orientation, for that particular trial. The control strategy developed in Chapter 3 was used. In all the figures that follow, conductive objects are shown in grey color, whereas non-conductive objects are shown in brown.

4.3.1   Straight Tunnel

A straight tunnel consisting of conductive walls was considered in Chapter 3. Here, two additional cases are considered, one with both the walls being non-conductive and the other with one conductive and one non-conductive wall. In each of the three cases, four trajectories corresponding to four initial conditions have been plotted. The objective was to center between the two walls thus demonstrating the centering behavior.

4.3.1.1   Conductive Walls

As expected, the results obtained here were similar to those obtained using electrostatics. A 1 meter (3.3 feet) was used with both the walls being conductive. The sensor disc radius was taken to be 75 mm (3 inch). The electric field source on the sensor was set to generate a sinusoidal waveform of 3 volt peak-to-peak at 100 Hz frequency. ANSYS solved the quasistatic problem and an iterative control scheme was implemented via MATLAB. It can be seen from Figure 4.3A that, irrespective of the initial conditions, the vehicle carrying the electro-sensor was able to converge

to the desired steady-state condition by aligning with the centerline and heading straight down the tunnel. The feedback gains $K_y = -20$ and $K_\theta = -40$ were used. The magnitude of the forward velocity of the vehicle was maintained to be 0.5 m/sec (3.3 ft/sec). Figures 4.3B&C show the time traces of the actual and relative states
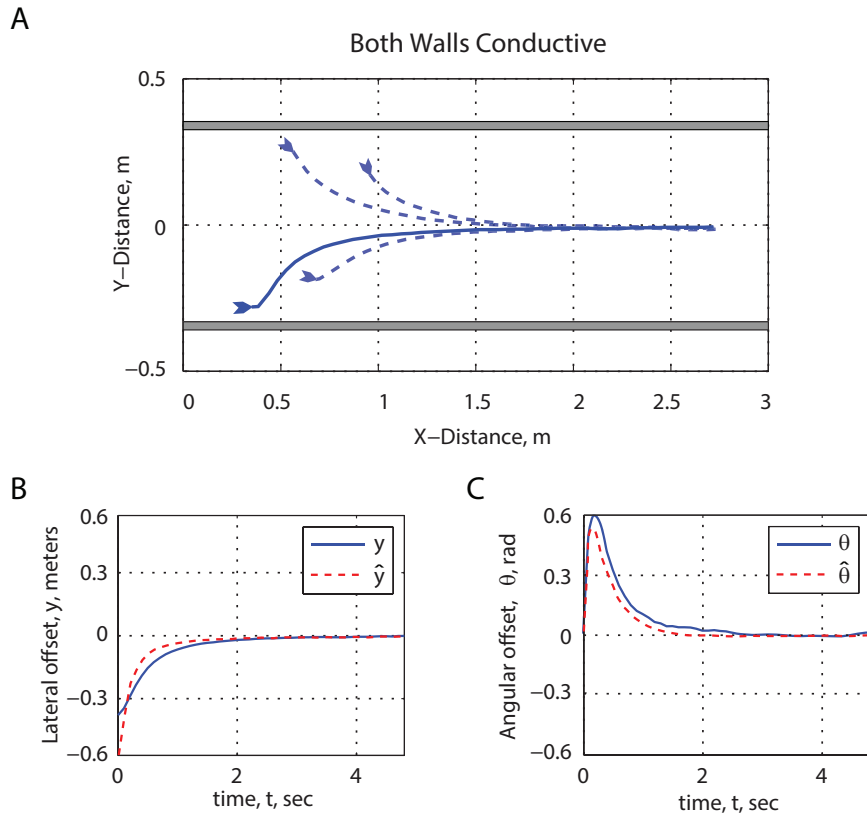
Figure 4.3: Simulation results for a straight tunnel with conductive walls. (A) Trajectories, (B) Actual and estimated lateral offsets, y and $\hat{y}$,(C) Actual and estimated angular offsets, θ and $\hat{\theta}$

for the trajectory drawn using a continuous line in Figure 4.3A. A general agreement in terms of nature and shape is observed between the actual states, y and θ, and relative state estimates, $\hat{y}$ and $\hat{\theta}$, as expected for the control strategy.

4.3.1.2   Non-conductive Walls

This case is analogous to the previous one with both the walls being non-conductive in nature. The tunnel was 1 meter (3.3 feet) wide. The controller gains were changed to $K_y = 30$ and $K_\theta = 60$ in this case. All the trajectories showed convergence with the steady state condition. The time traces of the actual and relative states exhibited
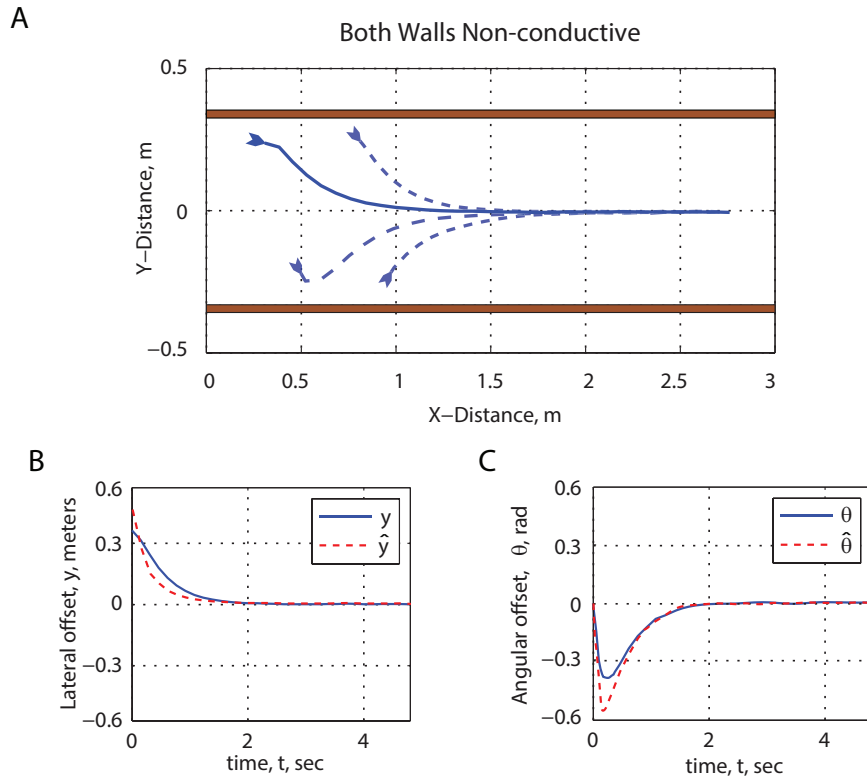
Figure 4.4: Simulation results for a straight tunnel with non-conductive walls. (A) Trajectories, (B) Actual and estimated lateral offsets, y and $\hat{y}$,(C) Actual and estimated angular offsets, θ and $\hat{\theta}$.

behavior similar to the conductive wall case above.

4.3.1.3 One Conductive and One Non-conductive Wall

We implement the modified controller to achieve obstacle avoidance in the case of one conducting and one non-conducting wall. Accordingly, $\sin(\gamma)$ and $\sin(4\gamma)$ were used as the optimal state extraction functions, with controller gains $K_y = -20$ and $K_\theta = -40$. All of the variables, including tunnel width, sensor radius, forward velocity etc., the same as the other tunnel simulations described above. The results are shown in Figure 4.5. The trajectories originating from different initial conditions exhibited convergence but not to the centerline of the tunnel, because of the steady state error in the y state. This behavior can be explained as follows.

Originally, the control strategy to navigate through such a hybrid tunnel was designed by taking absolute values of electrostatic electric images for a conductive tunnel because electrostatic equations to compute the electric image due to the non-conductive wall were not available. It was assumed that the electric image due to a conductive wall is comparable to that due to a non-conductive wall. However, this assumption is not accurate according to [26]. In this problem, the modified electric image is obtained by taking the absolute value of the FEM generated electric image. Such an image due to a non-conductive wall is smaller in magnitude than its conductive counterpart. In other words, the non-conductive wall produced smaller perturbations to the electric field of the sensor. This made the algorithm believe the wall to be farther away than it actually is. The objective of WFI based control strategies i.e., to equalize the perturbations on both the sides of the sensor. In this case, this condition is satisfied when the sensor moves closer to the non-conductive

71
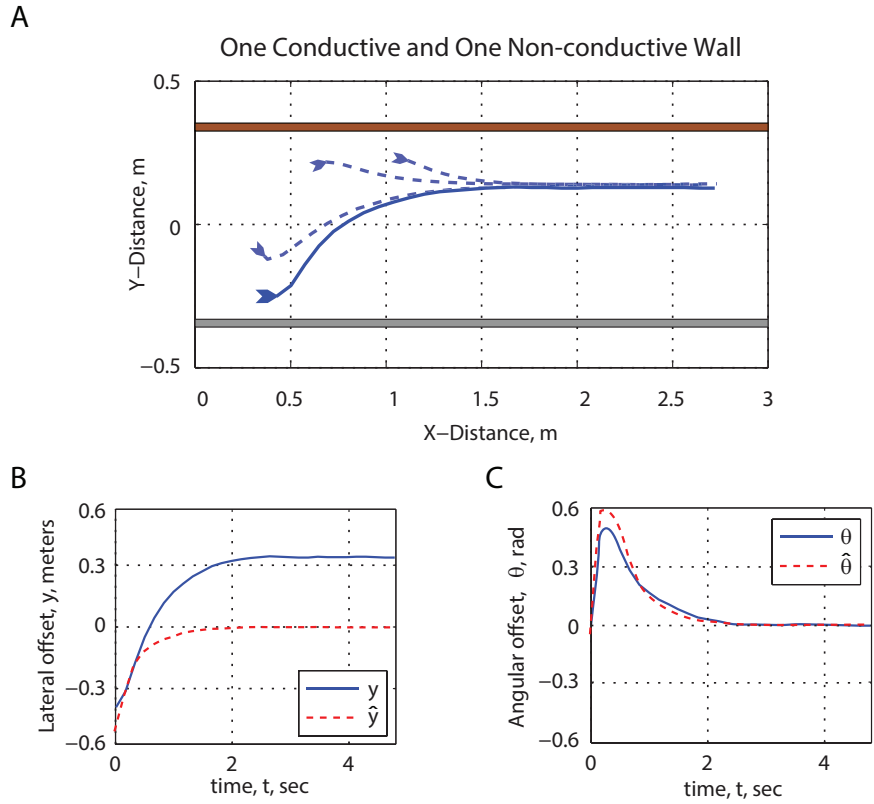
Figure 4.5: Simulation results for a straight tunnel with one wall each of conductive and one non-conductive properties. (A) Trajectories, (B) Actual and estimated lateral offsets, y and $\hat{y}$,(C) Actual and estimated angular offsets, θ and $\hat{\theta}$.

wall to balance the perturbations. Hence the steady-state offset is encountered.

In general, in the presence of two walls or objects of different electrical properties on either side of the sensor will produce a steady state offset towards the one with lower conductivity.

4.3.2   Cluttered Corridor

A cluttered environment is constructed by filling the sides of a curved corridor with objects of complex geometries. Care was taken while constructing these environments to not to create gaps between objects that were wide enough for the vehicle to take an alternative path and escape. To the vehicle, the randomly shaped obstacles look like walls forming a local tunnel at every instance and the straight tunnel algorithm is followed. The vehicle is repelled away strongly by objects of large size. Corrections are made to the trajectory after this behaviour and the vehicle is subsequently brought near the center of the corridor. This continues until the vehicle has traversed until the end of the corridor. Three cases have been considered as before. The first one had all conductive objects, whereas the second one had all non-conductive objects. The third case is the one where all the objects on one side of the corridor were non-conductive and those on the other were conductive. Four trajectories originating due to four initial conditions have been plotted for each of the three cases.

4.3.2.1 Conductive Objects

Here all the objects were defined to be conductive in the FEM meshing step. The width of the tunnel varied between 0.7 m to 1.1 m (2.8 ft to 3.6 ft). The steady-state trajectory for this corridor was found by simulating at different locations in the tunnel and gathering those which yielded zero relative state estimates using the state extraction functions mentioned in Chapter 3. The process is summed up in Algorithm 2.

The resulting steady-state trajectory is shown in Figure 4.6. The steady states are not unique as the vehicle can find steady-state paths on the both sides of the small objects in the corridor. The paths B and (C) in the figure show these alternate steady state conditions. For computing the actual states of the vehicle, the appropriate patches of the steady-state trajectories shown above is used.

In the simulations to generate trajectories originating at various initial conditions the forward speed of the vehicle was maintained to be constant at 0.5 m/s (1.65 ft/s). Four trajectories due to as many initial conditions are shown in figure 4.7A. The gains of $K_y = -5$ and $K_\theta = -10$ were used in all the simulations. It was observed that the vehicle was repelled away strongly by objects of large size, e.g. the objects labeled L1 and L2. Following these large perturbations, the vehicle adjusted to the steady state condition by generating large control inputs formed by amalgamating large relative state estimates. It is interesting to note that the two small obstacles in the corridor present a situation where the vehicle can proceed from either side of the object, thus causing the variability in the resultant trajectories.

Algorithm 2: Steady-state estimation for cluttered corridors.

Input: Cluttered Corridor

. **Output**: Steady-state location in the corridor

. **begin**

for *Inertial frame x-coordinate $x_n \in X$ (X is a linear space of x-coordinates)* **do**

Select a y_0-coordinate and orientation θ_0 (in the inertial frame)

Compute electric image at (x_n, y_0, θ_0).

Compute relative-state estimates, $\hat{y}_0$ and $\hat{\theta}_0$.

if $|\hat{y}_0| > 1 \times 10^{-4}$ *and* $|\hat{\theta}_0| > 1 \times 10^{-4}$ *(convergence limits)* **then**

$y_1 = y_0 + \hat{y}_0$

$\theta_1 = \theta_0 + \hat{\theta}_0$

Compute electric image at (x_n, y_1, θ_1).

Compute relative-state estimates, $\hat{y}_1$ and $\hat{\theta}_1$.

k = 1

while $|\hat{y}_k| > 1 \times 10^{-4}$ *and* $|\hat{\theta}_k| > 1 \times 10^{-4}$ **do**

$y_k = -\hat{y}_{k-1} \frac{y_{k-1} - y_{k-2}}{\hat{y}_{k-1} - \hat{y}_{k-2}} + y_{k-1}$

$\theta_k = -\hat{\theta}_{k-1} \frac{\theta_{k-1} - \theta_{k-2}}{\hat{\theta}_{k-1} - \hat{\theta}_{k-2}} + \theta_{k-1}$

(Linear extrapolations assuming $(\hat{\cdot}_k) = 0$)

Compute electric image at (x_n, y_k, θ_k).

Compute relative-state estimates, $\hat{y}_k$ and $\hat{\theta}_k$.

$k = k + 1$

Assign steady state location $x_{ss_n} = x_n$, $y_{ss_n} = y_k$, $\theta_{ss_n} = \theta_k$

Figure 4.6: Steady-state trajectory for the cluttered corridor consisting of conducting objects.
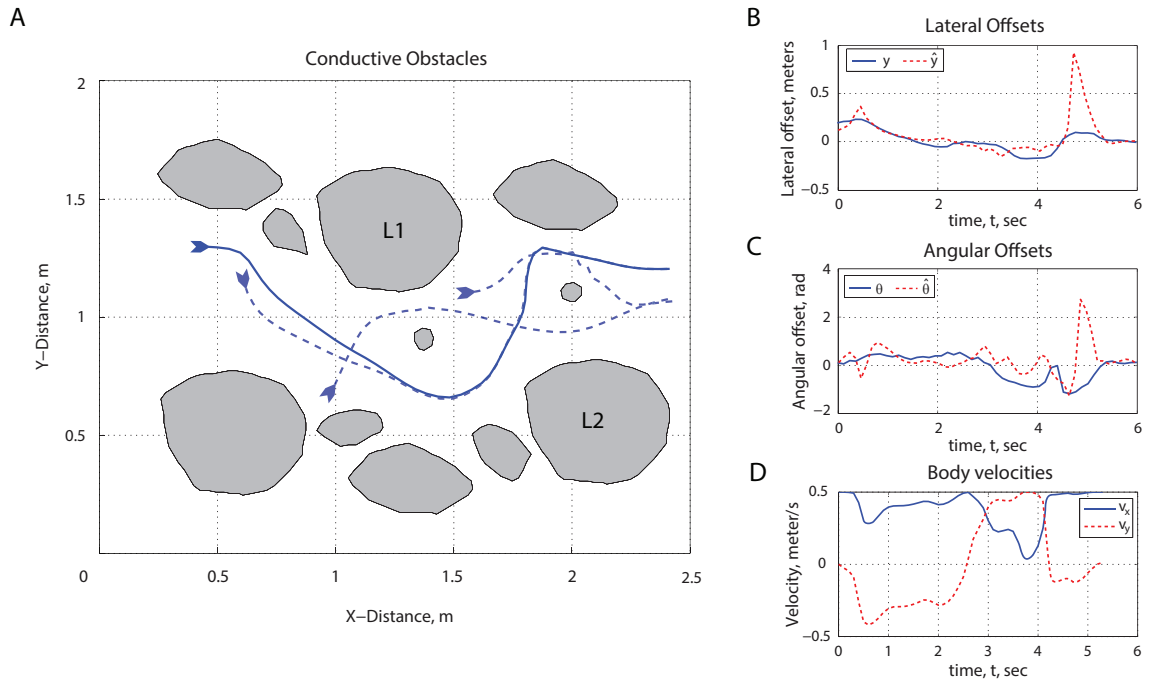
Figure 4.7: Simulation results for a corridor with all conducting objects. (A) Trajectories, (B) Time traces of actual and estimated lateral offset, y and $\hat{y}$, (C) Time traces of actual and estimated angular orientations, θ and $\hat{\theta}$, (D)Time traces of the velocity components of the vehicle in the inertial frame.

The actual states of the vehicle are the difference between the inertial frame coordinates of the trajectories traversed by a vehicle and the steady-state trajectory. Plots for actual and estimated states are shown in figure 4.7B and C. The large peak in the relative states plots towards the end is due to the large adjustment the controller makes to bring the vehicle back towards the steady-state. The evolution of velocity components of the vehicle in the inertial frame is shown in figure 4.7D. The resultant velocity components of the vehicle (or the body frame velocity) at all times was 0.5 m/s (1.65 ft/s) as specified in the beginning.

4.3.2.2 Non-conductive Objects

The steady-state trajectory for this case is exactly the same as that for the conductive obstacles case shown in Figure 4.8. the procedure mentioned in Algorithm 2 is followed here.

The behavior of the vehicle in a corridor with all the objects being non-conductive, was similar to the previous case. By modifying the gains as $K_y = 5$ and $K_\theta = 10$, the vehicle showed similar responses to the objects in the corridor as illustrated in figure 4.9A. It was provided a large perturbation signal by each of the large objects L1 and L2 from which it recovered by making appropriate changes to the the control input. The relative states showed convergence with the steady state around 1 second after the start of the simulation as can be seen from figure 4.9B and C. The actual states of the vehicle are the difference between the inertial frame coordinates of the trajectories traversed by a vehicle and the steady-state
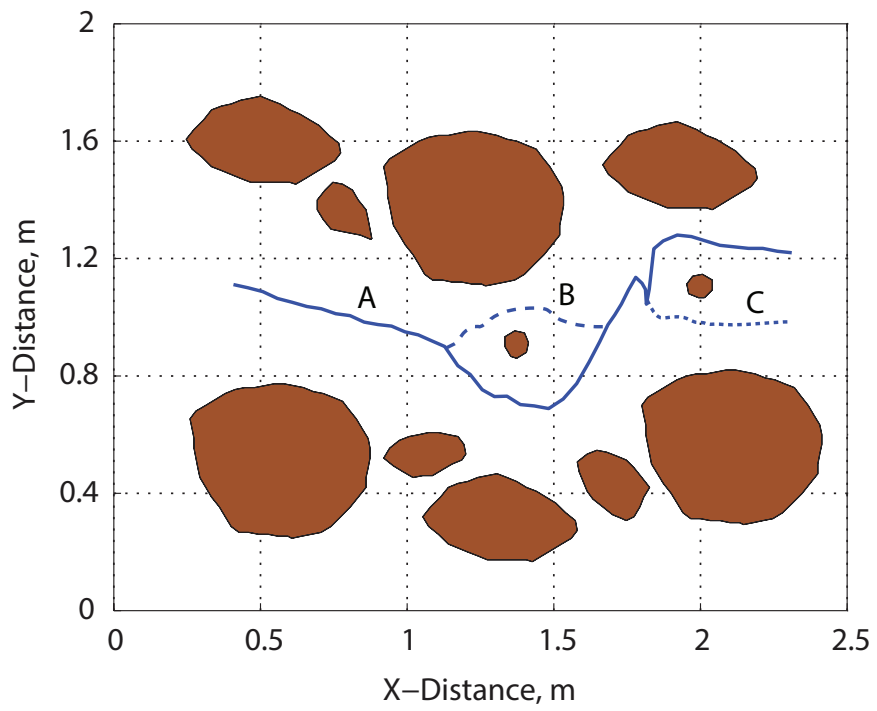
Figure 4.8: Steady-state trajectory for the cluttered corridor consisting of non-conducting objects.

Figure 4.9: Simulation results for a corridor with all non-conducting objects. (A) Trajectories, (B) Time traces of actual and estimated lateral offset, y and $\hat{y}$, (C) Time traces of actual and estimated angular orientations, θ and $\hat{\theta}$, (D)Time traces of the velocity components of the vehicle in the inertial frame.

80

trajectory. The sudden peaks in the relative states between 4 and 5 seconds into the simulation are due to the adjustment the controller makes to the trajectory in order to converge with the steady-state. The velocity profiles in figure 4.9D are the velocity components of the inertial frame velocity of the vehicle. The total velocity of the vehicle is specified and maintained to be constant at 0.5 m/s (1.65 ft/s).

4.3.2.3 Conductive and Non-conductive Objects

Among all the cases considered under the cluttered corridor problem, the case involving conducting and non-conducting objects simultaneously is the most challenging. It was shown in [52] that the composite electric image of two or more objects in juxtaposition is considerably different from a simple addition or superposition of their individual electric images. This deviation depends on a lot of factors like, distance between the objects, material and the geometry of the objects.

A corridor with objects on one side being all conductive and the other side being all non-conductive was considered here. The steady-state trajecory for this kind of an environment is computed using the procedure mentioned in Algorithm 2 and is shown in Figure 4.10.

In simulations demonstrating obstacle avoidance, the objects were assumed by the controller to be a local tunnel at any given instance. The results are presented in figure 4.11A–D.

The state extraction functions $\sin(\gamma)$ and $\sin(4\gamma)$ were used to generate the y and θ relative estimates. $K_y = -20$ and $K_\theta = -40$ were used as control gains.
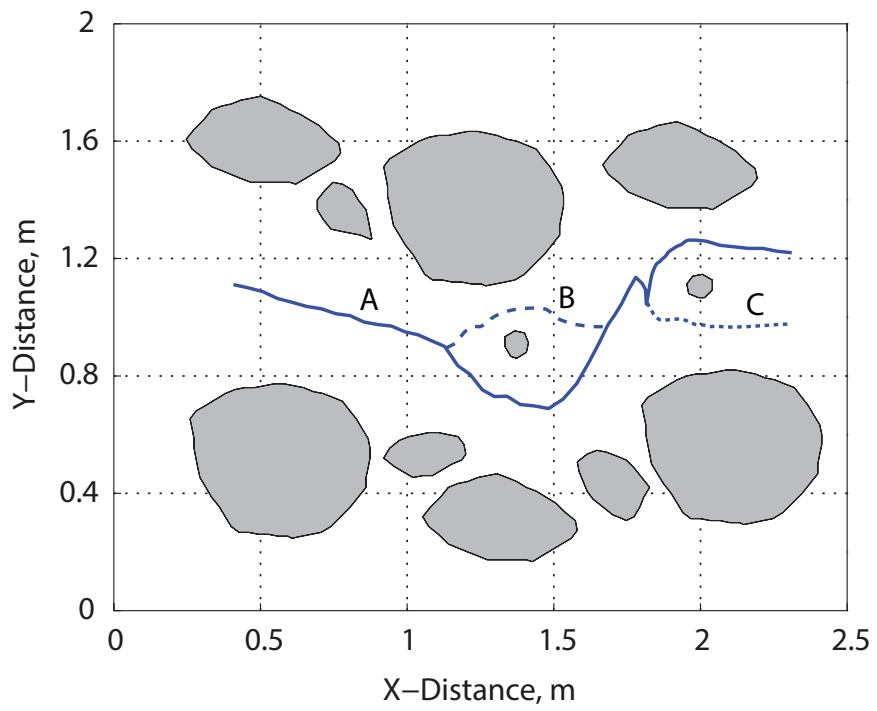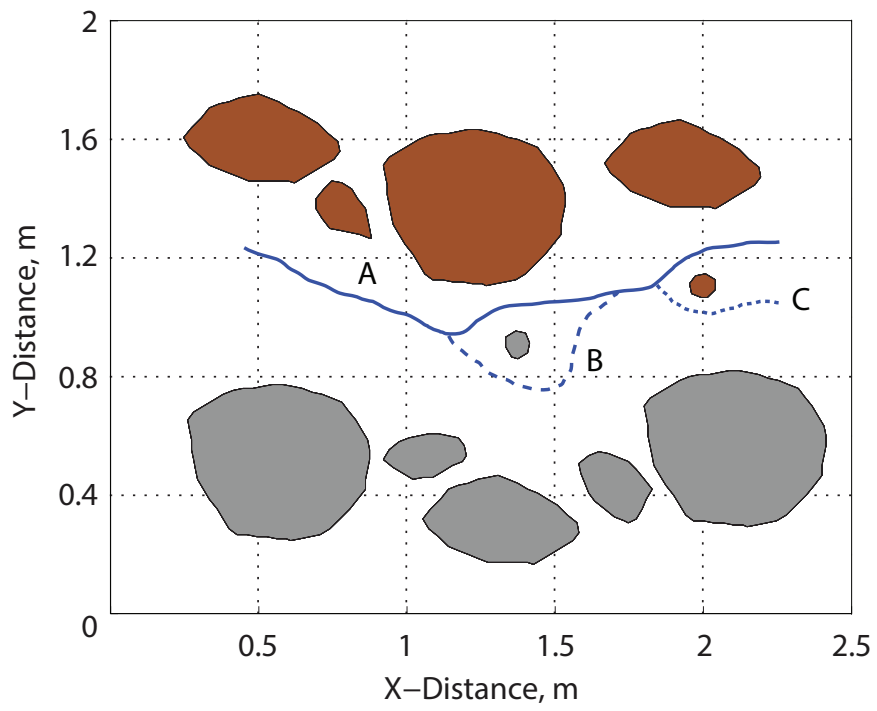
Figure 4.10: Steady-state trajectory for the cluttered corridor consisting of conducting and non-conducting objects.
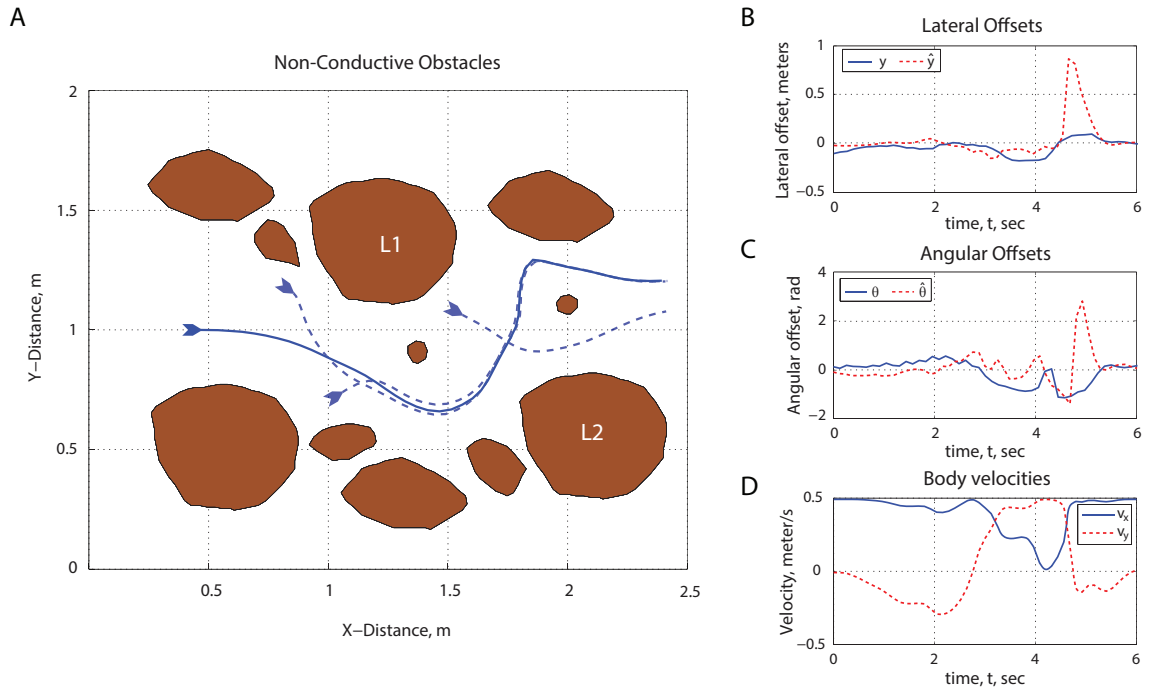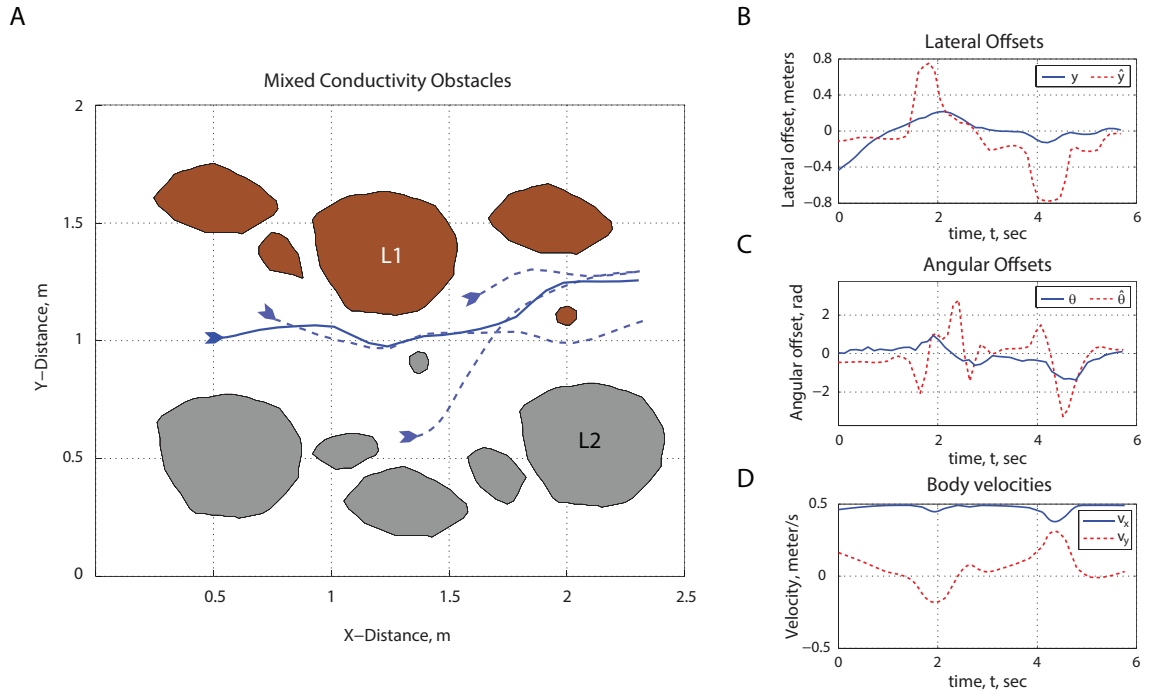
Figure 4.11: Simulation results for a corridor with conducting and non-conducting objects. (A) Trajectories, (B) Time traces of actual and estimated lateral offset, y and $\hat{y}$, (C) Time traces of actual and estimated angular orientations, θ and $\hat{\theta}$, (D)Time traces of the velocity components of the vehicle in the inertial frame.

The trajectories are shifted towards the non-conductive (top) side of the corridor, consistent with the mixed tunnel case. The time traces of the actual states, relative state estimates and body velocities have the same explanation as before. There was a steady state error in the value of the relative y estimate as the vehicle stabilizes away from the pseudo-center of the tunnel. The bumps at 2 sec and 4.5 sec instant in figures 4.11B–D occurred when the vehicle passed close to the smaller objects in the corridor.

4.3.3   Obstacle Field

An obstacle field is an environment with multiple obstacles that do not form a corridor. An obstacle field can give rise to multiple possible paths that the vehicle can take in order to avoid collisions. Here, an obstacle field was chosen to have a structured pattern of cylinders of same size. Each of the cylinders was placed roughly at an equal distance from its closest neighbors. Two walls were placed on the farthest sides of the environment to form barricades so that the vehicle does not escape from the sides. Due to the small sensing range of the sensor, these walls do not perturb the field of the sensor to induce a modulation in the electric image due to the cylinders. These walls were also selected to be of the same material as the cylinders near it. Depending on the initial conditions the trajectory which provides least obstruction was taken, out of the presented choices. Cases involving all conductive, all non-conductive and a mix of conductive and non-conductive cylinders were considered. Four trajectories originating due to four initial conditions have been plotted for

each of the three cases. Additionally, the time traces for actual states, relative state estimates and body velocities have also been plotted.

4.3.3.1   Conductive Cylinders

In this case, all the cylinders in the environment were conductive. They were arranged as shown in figure 4.12A. Conductive walls were placed as barricades at outer edges of the environment. The trajectories originating from 4 different initial conditions are plotted above. For the trajectory plotted in continuous line, the time traces of the actual states, relative state estimates and body velocities are plotted alongside. Here, the gains were selected to be $K_y = -20$ and $K_\theta = -40$. The state extraction functions for a 1 meter (3.3 ft). All the trajectories converged with the steady state condition after the initial adjustment phase. For this case where all the cylinders were conductive, the steady state condition loci were equidistant from the cylinders on either of its sides. The vehicle passed from either sides of the central cylinders in different iterations to demonstrate obstacle avoidance. Due to absence of a unique steady-state trajectory, actual states were not computed in these simulations. The relative state estimates are shown in Figure 4.12B and C. The plots in Figure 4.12D show the evolution of the inertial frame velocity components with time. The body velocity at all times was maintained constant at 0.5 m/sec (1.65 ft/sec). The trajectories arriving from either side of the central object towards the end did not converge afterwards and continued their course since there were no more objects present to induce a turn in the trajectories to initiate convergence.
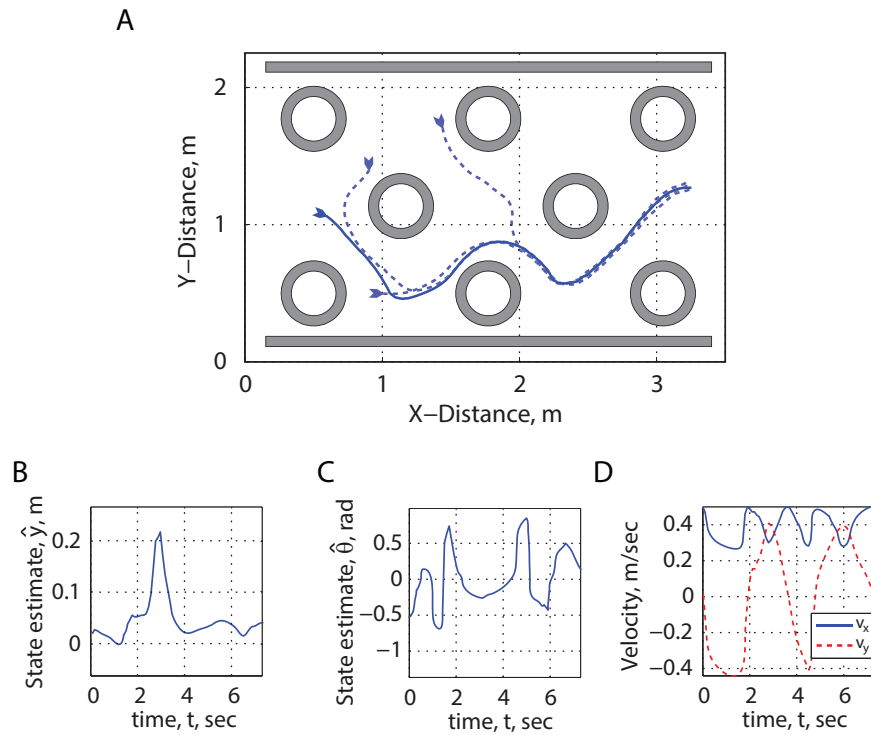
Figure 4.12: Simulation results for an obstacle field with all cylinders being conductive. (A) Trajectories, (B) Time traces of estimated lateral offset $\hat{y}$, (C) Time traces of estimated angular orientation $\hat{\theta}$, (D)Time traces of the velocity components of the vehicle in the inertial frame.

4.3.3.2 Non-conductive Cylinders

This case is similar to the conductive cylinders case above except that the value of the gains selected here were $K_y = 30$ and $K_\theta = 60$. The trajectories generated from 4 different initial conditions are shown in Figure 4.13A. Irrespective of the initial position, all the trajectories converged together and were completed without any collisions with the cylinders. The estimates states $\hat{y}$ and $\hat{\theta}$ are plotted in Figure 4.13B
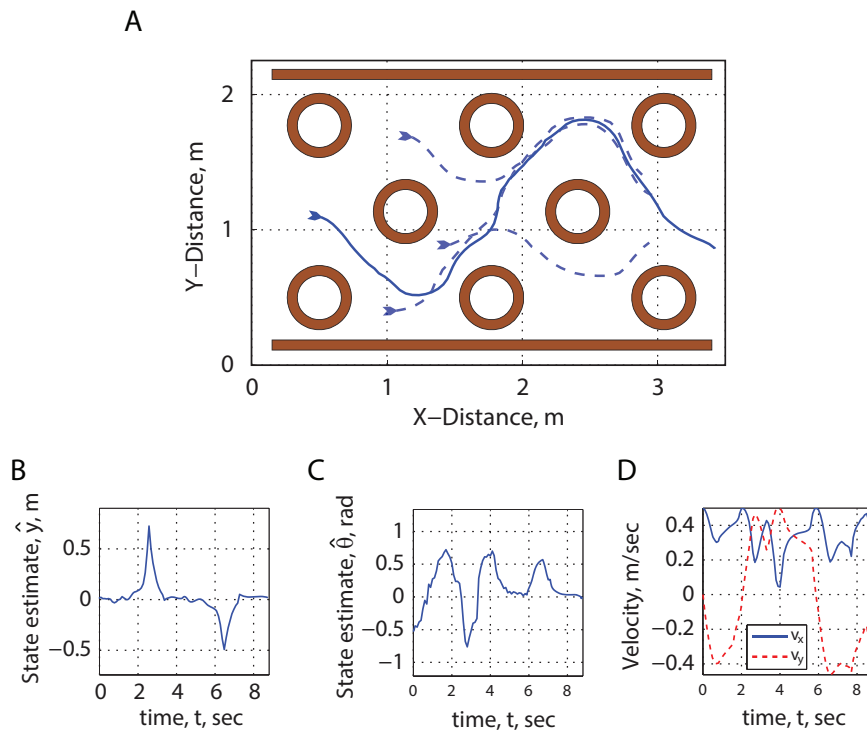
Figure 4.13: Simulation results for an obstacle field with all cylinders being non-conductive. (A) Trajectories, (B) Time traces of estimated lateral offset $\hat{y}$, (C) Time traces of estimated angular orientation $\hat{\theta}$, (D)Time traces of the velocity components of the vehicle in the inertial frame.

and C. Figure 4.13D shows the evolution of the inertial frame velocity components of the vehicle with time.

4.3.3.3 Conductive and Non-conductive Cylinders

The arrangement of the cylinders to form the obstacle field is shown in Figure 4.14A. The controller gains of $K_y = -20$ and $K_\theta = -40$ were used. It can be observed that all of the 4 trajectories were biased towards the non-conductive cylinders. This can be attributed to the perturbations of smaller magnitude due to the non-conductive cylinders in comparison to the conductive cylinders.
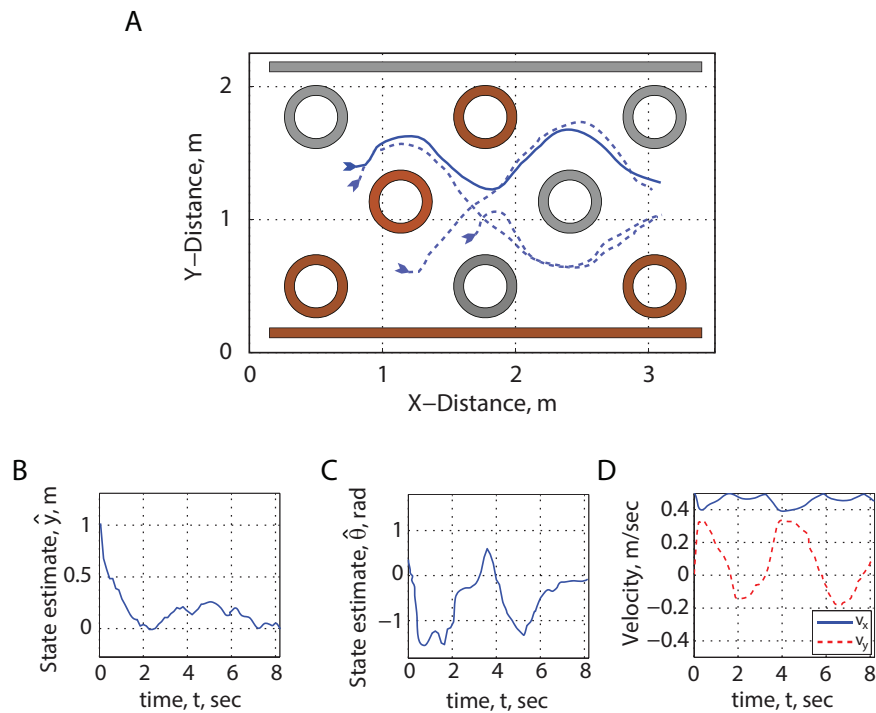
Figure 4.14: Simulation results for an obstacle field with conductive and non-conductive. (A) Trajectories, (B) Time traces of estimated lateral offset $\hat{y}$, (C) Time traces of estimated angular orientation $\hat{\theta}$, (D)Time traces of the velocity components of the vehicle in the inertial frame.

The relative states in 4.14B and C show peaks that were a result of the controller making adjustments to the trajectory in order to avoid collisions with any of

the cylinders. The inertial velocity components of the vehicle are plotted in 4.14D. The total velocity was maintained at a constant value of 0.5 m/sec (1.65 ft/sec).

From the simulations, it was realized that electrolocation can be used to perform reflexive unmapped obstacle avoidance with WFI based electric image processing. Assumptions like absence of noise and infinite sensor resolution are unrealistic in real world implementation. But for simulation purposes, these assumptions are useful since the viability of the algorithm could be tested. It is interesting to note that the control strategy derived using electrostatics equations worked well for these simulations. This proves that the WFI processing is efficient at computing navigational parameters from perturbation signals, electric images in this case. The quasistatic simulations provided a basis for designing the hardware for performing experimental autonomous navigation using electrolocation. In the next chapter, the details of the experimental setup and the electro-sensor hardware are provided. Additionally, the signal processing routine to form electric image signals resembling quasistatic electric images is also mentioned. The experimental results obtained using the electro-sensor and the signal processing routine are similar to the ones obtained here.

Chapter 5

Experimental Validation

In this Chapter, the experimental implementation of electric image acquisition and processing, Wide-Field Integration (WFI) based control and reflexive unmapped obstacle avoidance is described in detail. This includes an overview of the construction and operation details of the experimental setup. The electro-sensor design is motivated from the sensor model in Chapter 2. From the acquired signal, an electric image resembling a quasistatic image is generated. For this purpose, various digital signal conditioning routines were used, which have also been described. Finally, experiments were performed to demonstrate centering, clutter navigation and general obstacle avoidance. Results to these experiments are also reproduced here.

The experimental setup consists of an X-Y positioning gantry robot constructed above a glass water tank. For consistency, the environments used for performing experiments were a straight tunnel, a cluttered environment and an obstacle field, similar to the simulations in Chapter 4. For each environment three cases were considered, first with all objects being conductive, second with all non-conductive objects and third with a mix of conductive and non-conductive objects.

5.1 Experimental Setup

The experimental setup consists of two components. The first component is a large water tank that holds water for building different underwater environments. The second component is a gantry system to move the electro-sensor to positions computed by the controller. While the tank was obtained from a commercial vendor, the gantry and rest of the structure was custom-built in-house. Figure 5.1 shows the overall setup.
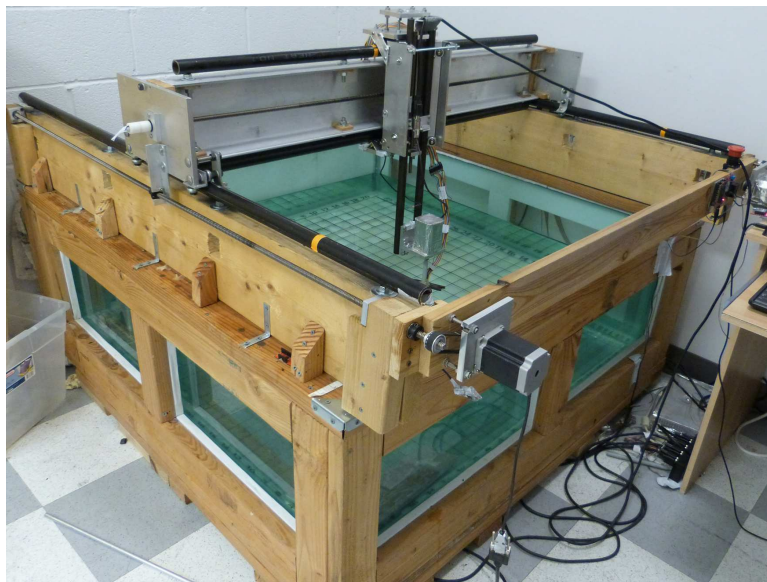
Figure 5.1: Experimental Setup consisting of glass tank and gantry.

5.1.1 The Tank

The tank measures 4 feet × 4 feet × 1.5 feet (1.2 m × 1.2 m × 0.45 m) and is made up of 0.75 inch (2 cm) glass. A sturdy wooden frame for the tank was constructed for additional structural strength and with an intent of installing wheels for ease

of motion. The tank was fitted with a 3 inch (7.5 cm) diameter drainage in one of its corners. A grid of resolution 2 inches × 2 inches (5 cm × 5cm) was drawn on the floor of the tank and sprayed on with clear acrylic spray. A 1/16 inch (0.16 cm) thick plexiglass sheet was laid on the floor for protecting the grid from being scraped off. The edges of the plexiglass were sealed using a silicone sealant.

5.1.2 The X-Y Gantry Robot

The electro-sensor is desired to be navigated between obstacles while the controller computes its motion. Here, the demonstration of the effectiveness of the WFI based electric image processing for extraction of proximity information of obstacles was the goal. This information was used to perform obstacle avoidance in different environments.

The X-Y gantry robot moves the electro-sensor from one location to the next as commanded by the controller. The design of the gantry was based on the XY robot design available on the website http://www.solsylva.com/. It is constructed on the water tank and is an integral part of the experimental setup. It consists of a horizontal beam that can move along the X-axis of the tank on leadscrews. Another carriage which is capable of moving along the Y-axis is mounted on a leadscrew on the beam. For Z-axis motion, another leadscrew driven carriage is mounted on the Y-axis carriage. All the leadscrews are driven by stepper motors for accurate motion. In addition to these motions, yaw rotational motion is added to the setup by adding a stepper motor directly on the Z-axis carriage. The electro-sensor is mounted on

a long rod which is coupled with the spindle of the yaw stepper. Thus a motion in X,Y,Z and yaw can be prescribed to the sensor. Since this work concentrates on a planar electrolocation problem, the Z-axis motion is not used. However, it is available for any future experiments which may possibly include more DOF motion of the sensor.

All the leadscrews have 4-starts, with a maximum diameter of 3/8 inch (~10 mm), a pitch of 0.375 inch (~10mm) and are made up of stainless steel. A multistart leadscrew translates the parts coupled to it farther in fewer rotations. Thus, the stepper motors are made to rotate fewer number of times thus increasing their overall life. Most of the components required to build the gantry robot were machined in the machine shop facilities available. These parts included, brackets, carriage structures, bearing flanges and other additional parts. Remainder of the parts including, fasteners, bearings, and other supplementary hardware were procured form commercial sources.

Generic High-torque Nema 23 380 oz-in stepper motors were used to drive the leadscrews through toothed belts and pulleys. The stepper motors are controlled using the Geckodrive G540 4-axis motor controller and powered by a 48 volt, 12.5 ampere switching power supply. The G540 receives CNC commands directed to all the steppers in parallel from a Linux based system running on a 3 GHz Core 2 Duo processor and 4 GB RAM. The gantry has a positioning accuracy of 0.001 inches (0.025 mm) and a workspace that covers an area of 42 inches × 42 inches (~1 m × 1 m) in the X-Y plane. Additional 15 inches (38 cm) motion along the Z-axis plane can be added if necessary in future. The gantry is programmed to move at a

nominal forward speed of 2 inches/s (0.05 m/s). and maximum rotational speed of 90°/s. However it can be configured to operate at other values.

5.1.2.1 Electromagnetic Noise from Stepper Motors

It was realized after beginning experimentation, that the stepper motors from the gantry robot induce high frequency electromagnetic noise to the electric field of the sensor. The consequence of this is that the electric image generated were extremely noisy and unworkable at times. Various analog and digital filtering techniques were used to mitigate this noise, but results did not improve. Multiple layers of high order digital filters could clean up the signal to a satisfactory level. We used two layers of a 9th order digital filter for this purpose. However, such high order filtering introduced considerable time delay to the filtered output. Thus, first few wavelengths of the captured signal were to be neglected in order to compute RMS value of the filtered signal. This called for capturing more data at every iteration and for performing such heavy filtering. This slowed the process significantly and a continuous operation of the gantry by updating the controller at high rates was not viable any more.

This prompted us to use a different approach at capturing electric images. The algorithm is now modified to momentarily shutdown the motors completely while the sensor readings are acquired. Following this the motors are started again to perform the motion as dictated by the controller. This algorithm sacrifices the ability to perform a continuous motion in an environment due to the starting and stopping of motors. But it is believed that this approach is better than acquiring noisy

readings, spending significant amount of resources at filtering them and updating the actuators at a slow rate.

5.2 Electro-sensor

The electro-sensor used in the experiments is directly adapted from the electro-sensor model used in the simulations as shown in Chapter 2. It is constructed in a manner similar to that explained by MacIver and Nelson [22] using EKG sensors with the difference being the shape of the electro-receptor array being circular instead of linear and the location of the source being at the center of the array. A total of 16 electro-receptors were used. The CAD model for this construction and the electro-sensor hardware are shown in figure 5.2. The conical projections from the

A   B
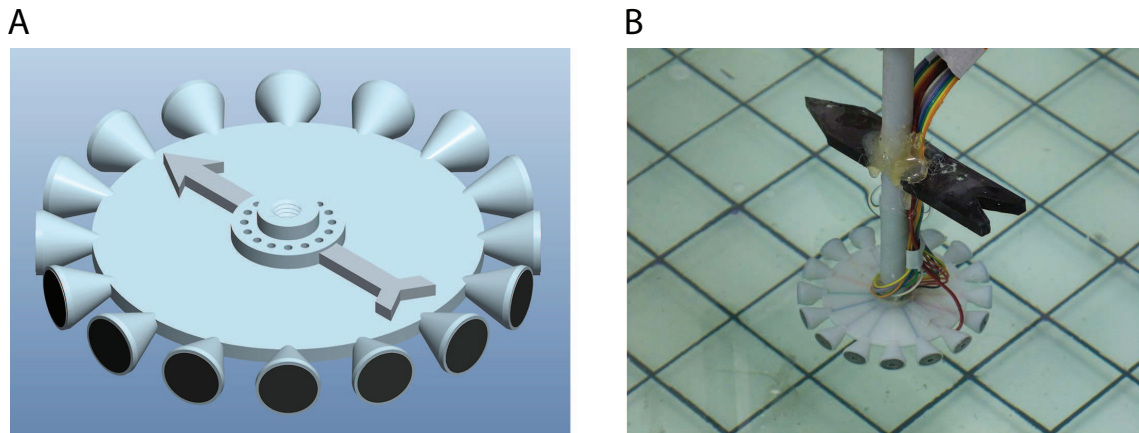
Figure 5.2: Electro-sensor in experiments. (A) CAD model, (B) Electro-sensor assembled on the setup.

sensor disk are the fixtures to hold the EKG electrodes and the source electrode is placed at the center underneath the disc of the sensor. The sensor was designed with a maximum diameter of 3 inches (75 mm) in which the actual solid disc occupied

a diameter of $2\frac{5}{8}$ inches (~65 mm) and the conical projections were 3/8 inches (~10 mm) long. Each EKG sensor used as electro-receptors had a diameter of 3/8 inches (~10 mm). The source is supplied with a 3 V peak-to-peak, 100 Hz sinusoidal voltage. This source was selected in order to mimic wave-type weakly-electric fish, which generate electric fields similar to the one used here. The sensor body is built using a rapid prototyping machine and is held on the yaw axis motor on a shank and kept immersed at least 8 inches (0.2 m) below the surface of water in the tank to avoid any effects due to the ripples generated at the water surface. Each of the sixteen electro-receptors on the periphery of the sensor is connected to ground through a 10 kΩ resistor. These resistors mimic the fish's skin resistance. For a fish the voltage drop across the skin is the electric image. In this electro-sensor the potentials measured at the electro-receptors are the voltage drops across the 10 kΩ resistors which constitute the electric image. The electro-sensor is capable of measuring the effect of the resistance of an object (amplitude modulation of signal) on the electric field and not the complex impedance (phase shift) as observed in electric fish [19]. Conductive as well as non-conductive objects can be detected using this electro-sensor.

The electric images similar to the ones described in Section 2.3 are obtained by unwrapping the electric potential profile formed at the electro-receptor locations starting at the electro-receptor located at $\gamma = 0$. This interpretation of the electric image is relevant to the controller design explained in Chapter 3. Thus, the state extraction functions described there, can also be applied to the electric images so obtained. However, it should be noted that the electric potential sensed

at the electro-receptors is not static but sinusoidal in nature due to a sinusoidal source voltage. Hence, to acquire electric images similar to the quasistatic images in Chapter 4, a signal processing routine is employed as mentioned below.

5.3   Signal Processing

The signal processing step is made up of two parts, signal acquisition and the processing of the acquired data to form a quasistatic image. Two prerequisites of the signal processing routine are that the signal should be acquired at high sampling rates and that the metric used to compute the quasistatic image from the dynamic data should be easy to implement in realtime. With high sampling rates, various operations like selecting a viable sample for analysis, filtering the sample etc. can be computed in realtime. Hence, a high sampling rate Data Acquisition (DAQ) system is used. Due to a simple metric to convert the data into quasistatic electric image, extra computational effort is not wasted in carrying out the computation. For this purpose, the root-mean-square (RMS) of the acquired sample is considered as the potential value. It is not only a straightforward computation, but it has a practical similarity to the quasistatic potential.

5.3.1   Signal Acquisition

With a sinusoidally varying source, the signal sensed at each electro-receptor is a sinusoid. This sensed signal is significantly lower in magnitude as compared to the source potential. The reason behind this is that the electric field of the source

attenuates with increasing distance from it. The equipotential lines at the distance of the electro-receptors are considerably lower in magnitude due to low conductivity of water. In addition, the sensed signal is the voltage drop across the 10 kΩ resistors in series with the electro-receptors symbolizing the skin voltage. The total effect of these two factors decrease the magnitude of the sensed potentials. For this reason a data acquisition system which has a digitization resolution high enough to resolve potentials of this order is required.

The signals from all of the 16 electro-receptors were acquired using National Instruments PCI-6224 Data Acquisition board. This board has a 16 bit analog to digital conversion (ADC) resolution. With this sort of a resolution and a 5 volt basis used for the ADC, an accuracy of $\frac{5}{2^{16}} = 76\mu V$. Such an accuracy is extremely high even for our purposes, but is a very desirable quality of the DAQ system. The particular DAQ board has a maximum sampling rate of 250 kS/s. This provides a sensing bandwidth of 15.625 kS/sec for each receptor, which imparts a very high sampling rate to the acquired signal. Thus the DAQ board is an extremely good choice to acquire the level of accuracy desired for this setup.

We acquire 5 cycles every iteration at each receptor. The frequency of the sensed signal at each receptor is the same as that of the source frequency of 100 Hz. With a sampling rate of 15.625 kS/sec, there will be $\frac{5}{100} \times 15.625 \times 10^3 \approx 781$ samples in the recorded 5 seconds of data. This large number of data points recorded in 0.05 seconds is helpful in implementing a lowpass filter to attenuate the sensor noise. An example of filtering is shown in figure 5.3. A digital lowpass filter of 1st order with the cutoff frequency of 500 Hz was used. Higher order filters could yield better

results, but they impart time delays due to which the first few cycles of the filtered data are not useful for computation of RMS. So 1st order filter was considered to be sufficient for this problem. This filtered signal is then further processed to compute
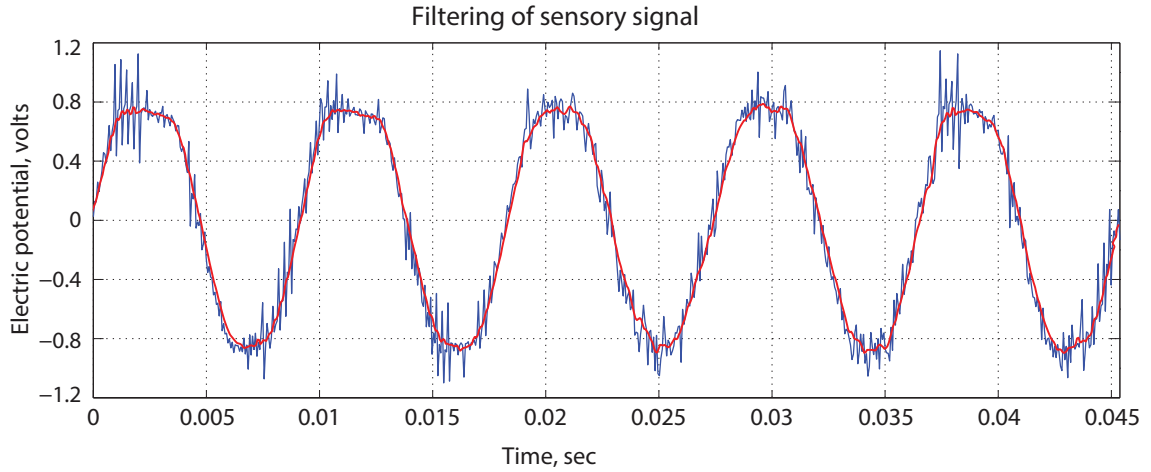
Figure 5.3: Filtering of the sensory signal.

the RMS value. This is repeated for each of the 16 electro-receptors. The code to acquire data and process it digitally employs multithreading to perform this task faster in parallel for all the receptors.

5.3.2 Quasistatic-like Approximation

It was mentioned earlier that a property of the acquired signal at each receptor similar to a quasistatic value was sought. This quasistatic approximation enables in application of the previously developed control strategy. a quasistatic approximation takes into account the dynamic nature of the field by performing the computations in frequency domain and hence treating the field as static in frequency. However, this is an artificial method of simplifying the computations. However nature does

not follow this method even if the source is oscillating at a single frequency, in these experiments for instance. The electric potential values that are read at each electro-receptor are arrived at by performing the full electromagnetic computations by nature. Thus the signal available for measurement is oscillatory and in time domain. However, if the RMS value of the sensed signal over a few cycles is computed, it can act as a representative for entire sensed data. The RMS takes into account the magnitude and the frequency of oscillation of the signal. Thus it is analogous to a quasistatic measurement. Continuing with the same example as before, the filtered
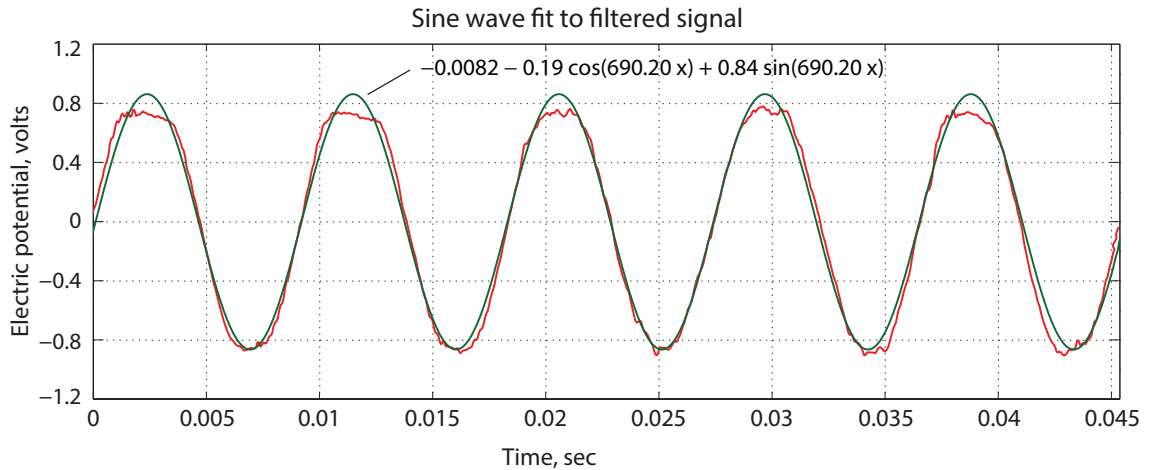
Figure 5.4: Fitting a sine wave to the filtered signal.

data can be seen to have a sinusoidal shape. It is known [22] that this filtered data should in theory be perfectly sinusoidal since the source signal is sinusoidal. The distortions in the sensed signal are caused due to various noise sources. To stay consistent with the theory, a sine wave could be fitted to the sensed signal as shown in figure 5.4 above. Once we have a sine wave fitted to the data, we can easily compute the RMS voltage of the wave. Two points are to be noted here. We fit

the sine wave to the filtered data and not the raw data since the noise present in the sensor data tends to make the fitted sine wave larger in magnitude and thus it does not represent the real data. Secondly, we do not compute the RMS off of the filtered data as we would need exactly full cycles. Thus fractional wavelengths of data will not give the correct RMS value unless the number of recorded cycles is very large. More cycles will however increase the time required for data acquisition and processing. So computing RMS off of filtered data is not considered and a sine wave it fitted to the data for this purpose.

We implement a least-squares four-parameter sine wave fitting [74] routine for this purpose. This algorithm yields an equation of the form $c + a_1 \cos(bx) + a_2 \sin(bx)$. In the above example, the fit to the filtered data is given as $-0.0082 - 0.19 \cos(690.20x) + 0.84 \sin(690.20x)$ where x is the time after start at any given instance. Three of the parameters yielded by this algorithm are useful in constructing a zero-mean sine function fit to the dataset. The fourth parameter provides the value of the DC shift of the entire dataset. It was observed that DC shift varies and drifts over time. To reject this drift, we ignore the fourth parameter of the sine-fit routine to get a zero-mean sine wave every time. Thus, in the above example $c = -0.0082$ can be ignored. The RMS value of the fitted wave is then easy find using the discrete values of the rest of the equation.

Performing this sine wave fitting for each sensor in parallel yields the quasistatic-type potentials at the electro-receptors, $V_{pert.}$. A precomputed set of such potentials, $V_{nom.}$ for the nominal case where no perturbing obstacles are present is available a priori. The electric image is then given as the difference between the potentials in

101

the presence of the obstacles and in the nominal case.

$$\Phi = V_{pert.} - V_{nom.}$$

The control strategy derived in Chapter 3 can be applied to an electric image so obtained.

5.4 Operation Sequence

The entire sequence of operations is summarized below:

1. Stop the motors.

2. Acquire readings.

3. Process readings and Start motors.

4. Move according to received commands.

Out of these, steps 1–3 are completed within 0.1–0.15 sec. The actual motion of the gantry adds another 0.25–0.3 sec. since the algorithm advances the gantry by about half an inch (1.25 cm) at a configured forward speed of 2 in/sec (5 cm/sec). Thus the total time per iteration is 0.35–0.45 sec.

All the above operations are performed on the same computer that controls the gantry motion. For starting and stopping the motors, instructions are sent by the computer over an XBee module attached to it to another of such module attached to gantry. These instructions are read by an Arduino board which operates a relay circuit to start and stop the motors all at once. Following the stopping of motors, the

computer instructs the DAQ board to read all the 16 sensors at once. The motor are instructed to start up as soon as all the readings are acquired to minimize the downtime. The acquired readings are processed in parallel to perform WFI from which relative states are obtained. The parallel processing is achieved by implementing 16 threads simultaneously. The controller then computes the control input to the actuators which is further processed to compute the next location of the sensor. A CNC command is then issued via a parallel port to the motor controller facilitating the motion of the gantry. This entire chain of events is executed by a single code written in Python.

In the following Section, the results to experiments in different environments are presented.

5.5   Experiments

Experiments were conducted on the lines similar to the quasistatic simulations. Experiments demonstrating tunnel centering, clutter response and obstacle field navigation were performed in environments having all conductive, all non-conductive or a mix of conductive and non-conductive objects. Conductive objects had aluminum plates to form a straight tunnel and steel pipes to form cluttered and obstacle field environments. Among non-conductive objects were wooden boards for the tunnel and PVC pipes for the remaining two types of environments. Example setup of each of the three types of environments can be seen in figure 5.5. A total of nine sets of experiments were performed. Three for conductive environments, three for
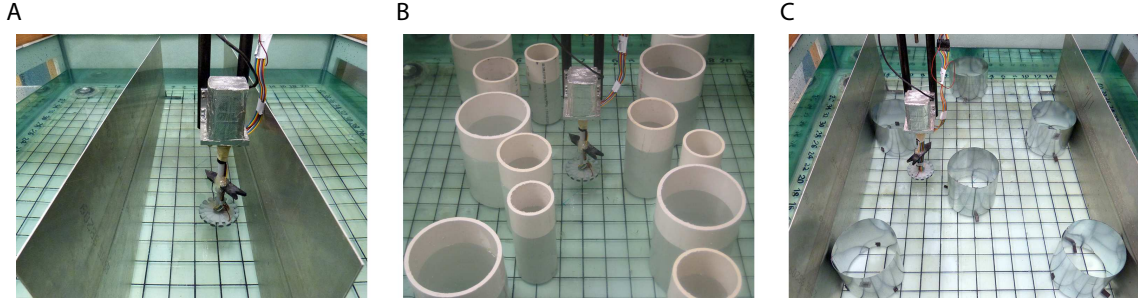
Figure 5.5: Environments for experimentation (A) Tunnel, (B) Clutter, (C) Obstacle field

non-conductive and another three for mix conductivity type environments. Each set was further divided into two subsets, each arising due to changing either the initial lateral offsets or the initial angular orientations, keeping the other initial condition constant. Also included is a selected trial among these for which actual and relative states along with body velocities are plotted. In the plots that follow, conductive objects are shown in grey color while non-conductive objects are shown in brown. The arrowheads on each trajectory indicate the initial position for that particular trial.

5.5.1 Straight Tunnel

The expected behavior of the vehicle carrying the sensor in a straight tunnel was to center itself along the centerline of the tunnel and directed forward. Through experiments, this particular behavior has been demonstrated in tunnels made out of conductive and non-conductive walls. We have used the control strategy developed in Chapter 3 for this purpose.

5.5.1.1 Both Walls Conductive

In this setup, two aluminum plates were used to form a 9 inch (23 cm) tunnel. The plates were 1/16 inch (1.6 cm) thick, 36 inches (91 cm) long and 12 inches (30 cm) tall. Figure 5.6B shows the experimental setup.
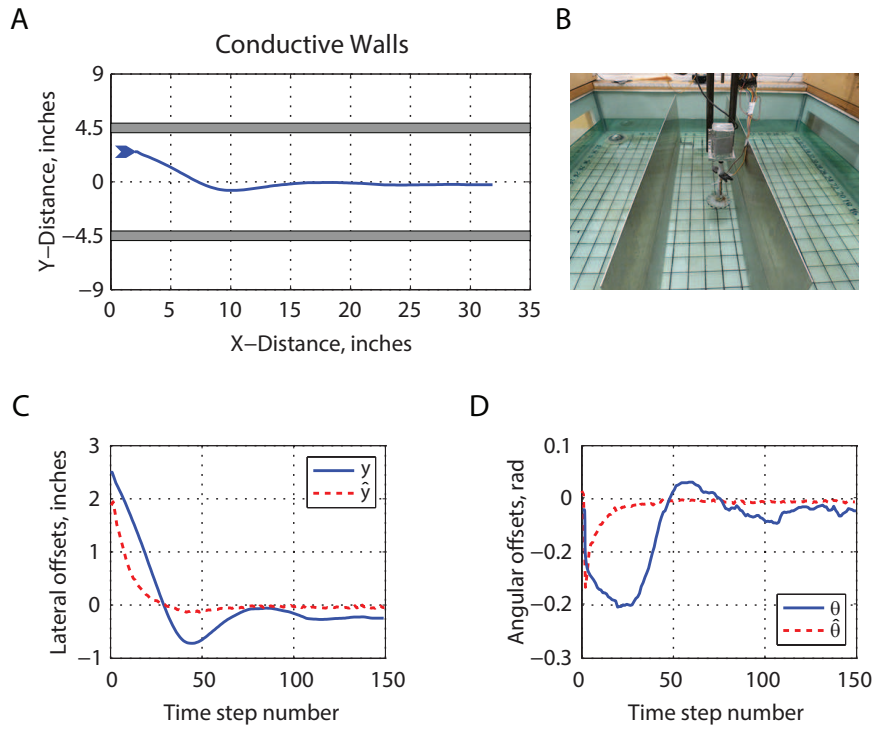
Figure 5.6: Experiment demonstrating centering in a straight tunnel having conductive walls (A) Trajectory, (B) Experimental setup, (C) Time traces of actual and estimates lateral offsets, y and $\hat{y}$, (D) Time traces of actual and estimated angular orientations, θ and $\hat{\theta}$

The trajectory in figure 5.6A indicates that the vehicle was centered in the tunnel soon after start and was maintained in that condition afterwards. Gains of $K_y = -20$ and $K_\theta = -40$ were used in this experiment. The controller designed in Chapter 3 was used. As was also seen in simulations, the objective of the controller

is to drive the relative states, $\hat{y}$ and $\hat{\theta}$ to zero. The relative states plots in Figure 5.6C and D confirmed this behavior of the controller. In contrast to the simulations for the tunnel problem, the actual states did not resemble the relative states exactly. A slight overshoot and a small steady state error in the lateral offset was observed as illustrated in Figure 5.6C and D. The overshoot was due to the gains not being good enough to damp out the oscillations in the trajectory. The steady state error can be attributed to misalignment in the tunnel and possible presence of exogenous electric field perturbations. The controller tries to balance the electric image perturbations in the right half with those in the left half of the electric image at all times. This balancing is interpreted by the controller as the achievement of the steady state condition and results in the relative states going to zero. However, in the presence of misalignment in tunnel geometry and exogenous perturbations, a bias is introduced which misguides the controller in thinking of a non-steady state condition as being a steady state one. This results in a steady state error. Since the error in the above trial was constant, the exogenous perturbation if present must have existed constantly throughout the length of the tunnel.

The controller was tested for variations in either one of the two initial conditions y_0 and θ_0 to test it for repeatablity and adaptability as shown in Figure 5.7. When the initial lateral offset was varied within the tunnel, the initial effort required to approach steady state was varied in proportion of the offset. After this initial stage, all the trajectories converge with the centerline of the tunnel. Similar behavior is observed when the initial angular offset is varied and the initial lateral offset is held constant. All the trajectories make initial turn maneuvers based on

106

Figure 5.7: Effect of variation in initial conditions on trajectories in a tunnel with conductive walls, (A) Variation in initial lateral offset, (B) Variation in initial angular offset

the initial angular offset and merge together to center in the tunnel. It is interesting to note that the overshoot was consistently observed in all the cases.

5.5.1.2   Both Walls Non-conductive

In this problem the tunnel was constructed out of two wooden walls that were 0.75 inch (1.9 cm) thick, 8 inches (20 cm) tall and 36 inches (91 cm) long. The experimental setup can be seen in Figure 5.8B.

The controller used in this trial is the same as that used for the conductive walls case. The only difference is the gains that need to be negated for the reasons explained in Section 3.6. In addition, electric images due to non-conducting walls are smaller in magnitude than due to their conductive counterparts. So the estimated states are of lower magnitude as well, requiring higher gains. Accordingly, the gains that were used in the experiment were $K_y = 30$ and $K_\theta = 60$. These gains do not cause instability as they multiply relative states that opposite in sign as that for

107

A Non-conductive Walls

B

C

D
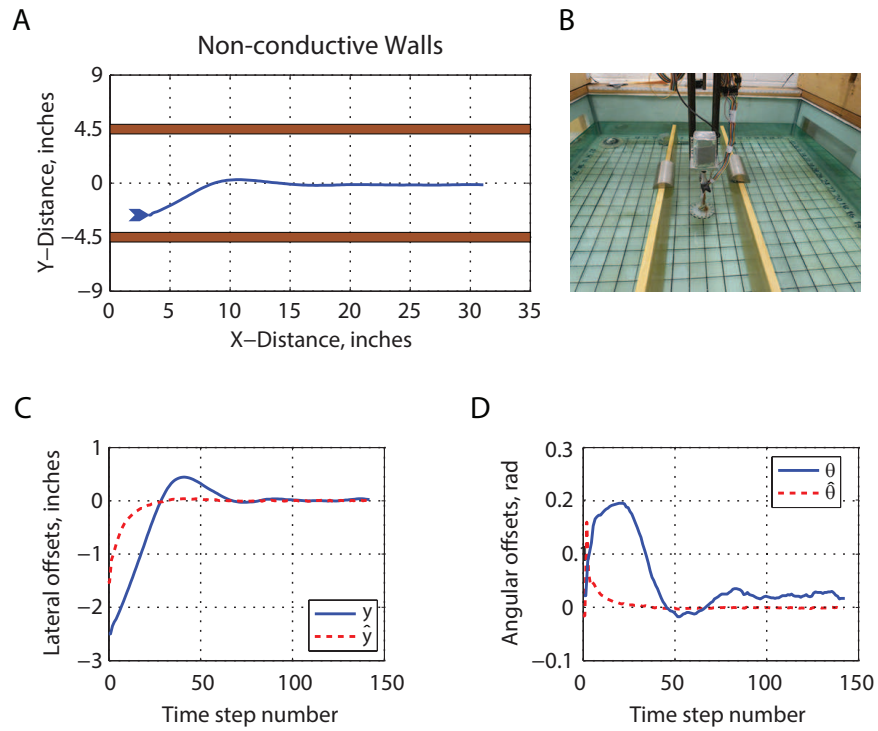
Figure 5.8: Experiment demonstrating centering in a straight tunnel having non-conductive walls (A) Trajectory, (B) Experimental setup, (C) Time traces of actual and estimates lateral offsets, y and $\hat{y}$, (D) Time traces of actual and estimated angular orientations, θ and $\hat{\theta}$

.

the conduucting tunnel case. Centering was achieved in the tunnel with negligible steady state error as can be seen in Figure 5.8A. Overshoot was observed in the trajectory and the relative state $\hat{y}$ due to the particular choice of the gains.
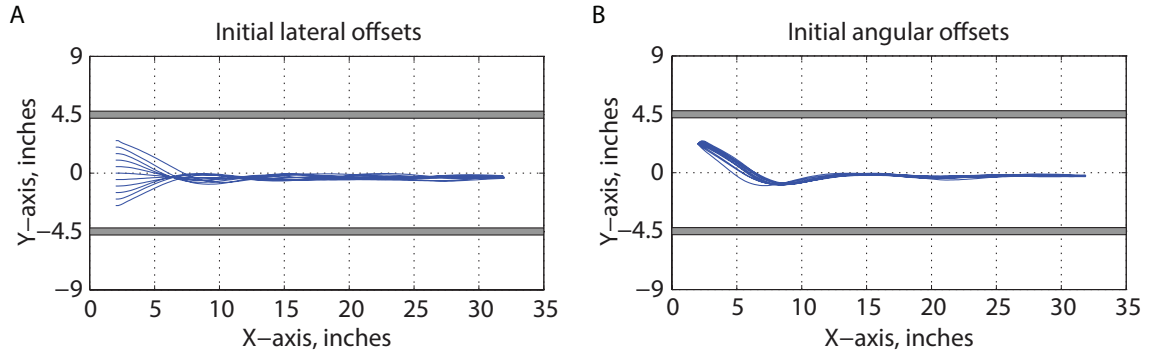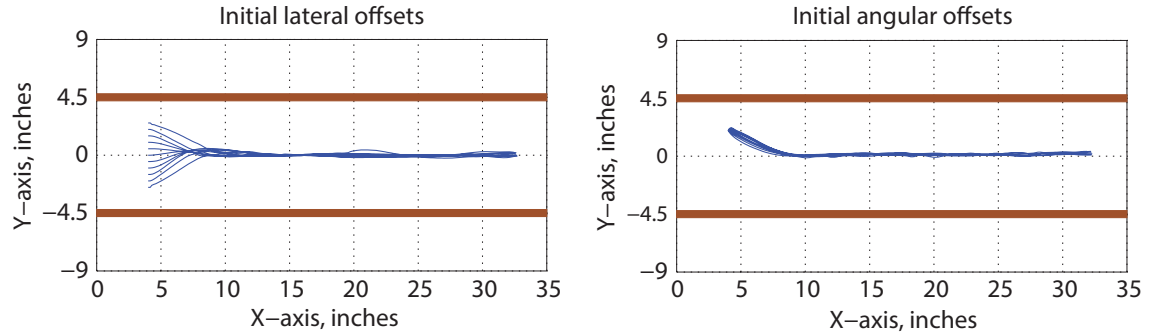

Figure 5.9: Effect of variation in initial conditions on trajectories in a tunnel with non-conductive walls, (A) Variation in initial lateral offset, (B) Variation in initial angular offset

On changing exactly one initial condition out of two, the control signal to the vehicle is varied accordingly to center itself in the tunnel. Convergence of trajectories was observed when initial lateral as well angular conditions were varied as seen in Figure 5.9.

5.5.1.3   One Conductive and One Non-conductive Wall

A tunnel was constructed with one aluminum wall and another with a wooden wall. At each iteration, absolute value of electric image was computed. State extraction functions of $\sin(\gamma)$ and $\sin(4\gamma)$ were used as per the discussion in Section 3.6. These functions were computed for a conductive walled tunnel but were used in this case nonetheless. The experimental setup is shown in Figure 5.10B.
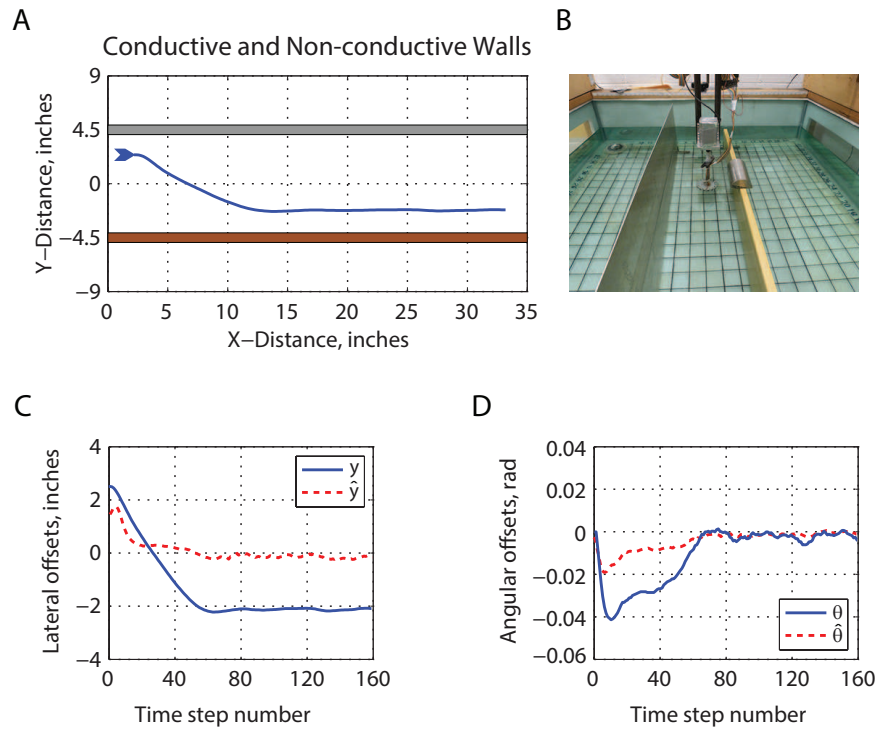
Figure 5.10: Experiment demonstrating centering in a straight tunnel having one conductive and one non-conductive wall (A) Trajectory, (B) Experimental setup, (C) Time traces of actual and estimates lateral offsets, y and $\hat{y}$, (D) Time traces of actual and estimated angular orientations, θ and $\hat{\theta}$

.

Interestingly, the vehicle did not align with the centerline but with a line 2 inches (5 cm) offset from it, as shown in the trajectory plot in Figure 5.10A. This behavior is in fact a very good result and informative result. With the above mentioned state extraction functions, the controller would center the vehicle perfectly if both the walls were made up of aluminum. However, a wooden wall generates perturbations that are smaller in magnitude than that of an aluminum wall. In a tunnel with one aluminum wall and one wooden wall, the perturbation due to one wall was lower than other. The controller tries to balance the electric field perturbations on right and left sides recorded by the electro-sensor. This balance is achieved at a position closer to the wooden wall and not at the center of the tunnel. The offset is also apparent in the plots for actual states in Figure 5.10C where the lateral offset y settled at a steady state value of -2. The relative states however settled at zero as shown in Figure 5.10D. This confirms that the controller worked as expected.
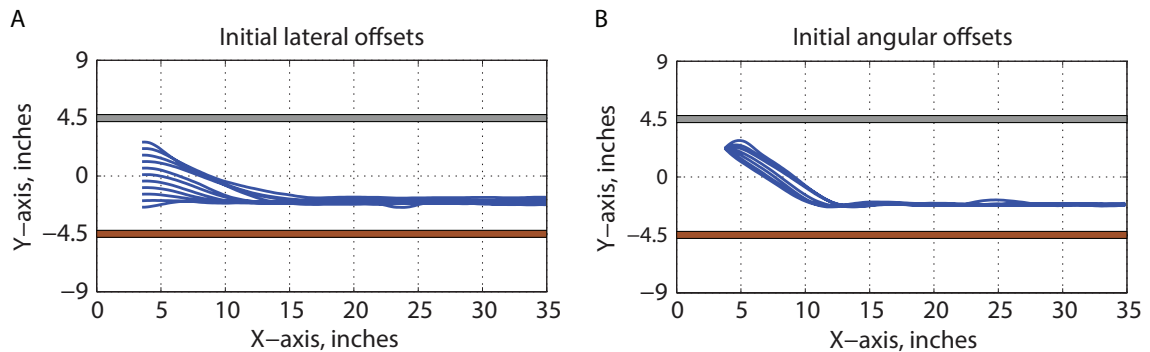
Figure 5.11: Effect of variation in initial conditions on trajectories in a tunnel with one conductive and one non-conductive wall, (A) Variation in initial lateral offset, (B) Variation in initial angular offset

When the experiment was repeated for multiple initial conditions where only

one variable out of two was varied at a time, consistent results were observed. Trajectories originating from different locations but with zero initial orientation values all converged to align with the line offset from the centerline. Same is also observed when the initial lateral offset was maintained constant and the the initial angular offset was varied. In both the cases, the steady state offset was found out to be the same. The results are plotted in Figure 5.11.

5.5.2   Cluttered Corridor

A cluttered corridor is formed when objects of complex geometries are placed in water to form a corridor, not necessarily straight. However, objects of such random shapes are not easily found commercially. Therefore, steel and PVC cylinders of different diameters were used to form this kind of environments. Cylinders of 3,4 and 6 inches (7.5, 10 and 15 cm) diameters were used. There was no particular template that was used to form these environments. The only care that was taken while forming these environments was to not to leave gaps of more than 5 inches (13 cm) between cylinders to prevent the vehicle from escaping the corridor. A small cylinder was placed midway in the corridor near the center to act as a local perturbation. This cylinder was small enough to not to be sensed by the sensor from far away. This cylinder was intended to induce a sudden reaction and trajectory correction by the vehicle. Three different cases were studied as before, first when all the cylinders were made up of steel, second when only PVC cylinders were used and third when a mix of the two types of cylinders were used. The steady state

trajectory similar to the one in the quasistatic simulations was not computed here. As a result, the actual states are not available.

5.5.2.1 Conductive Cylinders

In this case only steel cylinders were used to form the corridor. The steel cylinders were each 8 inches (20 cm) tall and made up of 1/32 inch (0.8 mm) thick steel sheet. Three cylinder sizes (diameters) were used, 3,4 and 6 inches (7.5, 10 and 15 cm). The arrangement if the cylinders is shown in Figure 5.12B.

As is seen in Figure 5.12A, the vehicle navigated between the obstacles without any collisions. The corridor had a varying width. Gains of $K_y = -20$ and $K_\theta = -40$ were used. On encountering the small object placed between the two sides of the corridor towards the end of the corridor, the vehicle made a sharp turn away from it in order to avoid collision.

This turn maneuver is seen in the relative states plot in Figure 5.12C and D when a sudden jump in the estimates occurs. For all other times, the estimates are seen to have values close to zero after the initial adjustment. On varying the initial conditions, one variable at a time, convergence of trajectories was observed. Both the cases when linear and angular offsets were varied separately, are shown in Figure 5.13.

Figure 5.12: Experiment demonstrating obstacle avoidance in a cluttered corridor constructed with conducting cylinders, (A) Trajectory, (B) Experimental setup, (C) Time trace of relative state, $\hat{y}$, (D) Time trace of relative states, $\hat{\theta}$
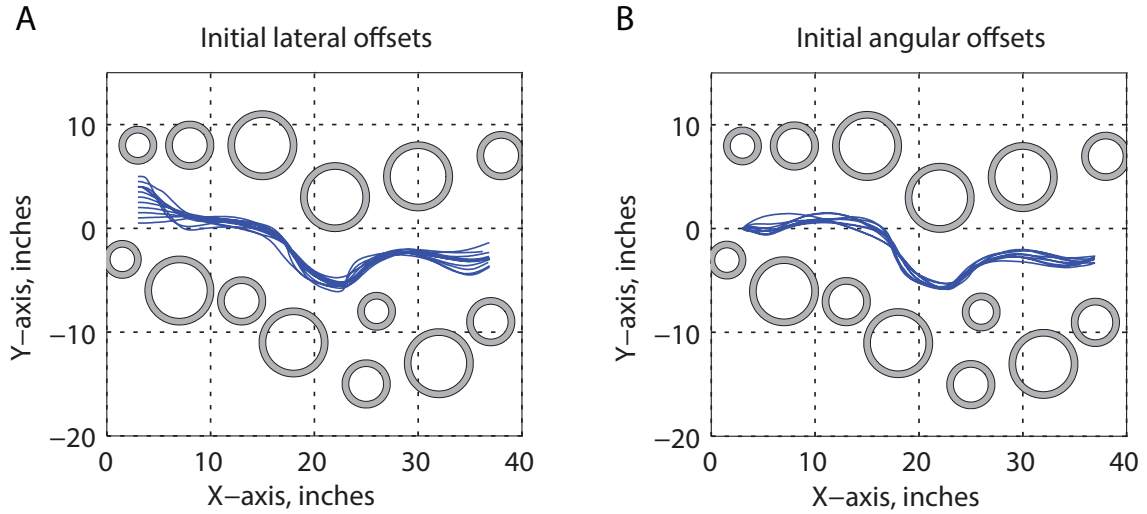
Figure 5.13: Effect of variation in initial conditions on trajectories in a cluttered corridor comprising of conductive cylinders, (A) Variation in initial lateral offset, (B) Variation in initial angular offset

5.5.2.2 Non-conductive Cylinders

In this set of experiments, the corridor is created using cylinders made out of PVC. Each cylinder was 1 foot (30 cm) in height. The arrangement of cylinders was not repeated from the one with conductive cylinders but a completely new one was used. However, a cylinder was placed in the corridor towards the end to produce a rapid correction in the trajectory by the vehicle similar to the conductive cylinders problem. The arrangement is shown in Figure 5.14B.

The gains used here were $K_y = 30$ and $K_\theta = 60$. The change in sign and higher magnitude in comparison to the previous case can be noticed. These changes were made in order to work with non-conductive cylinders due to the electric images resulting from them as explained in Section 3.6. The vehicle navigated between the
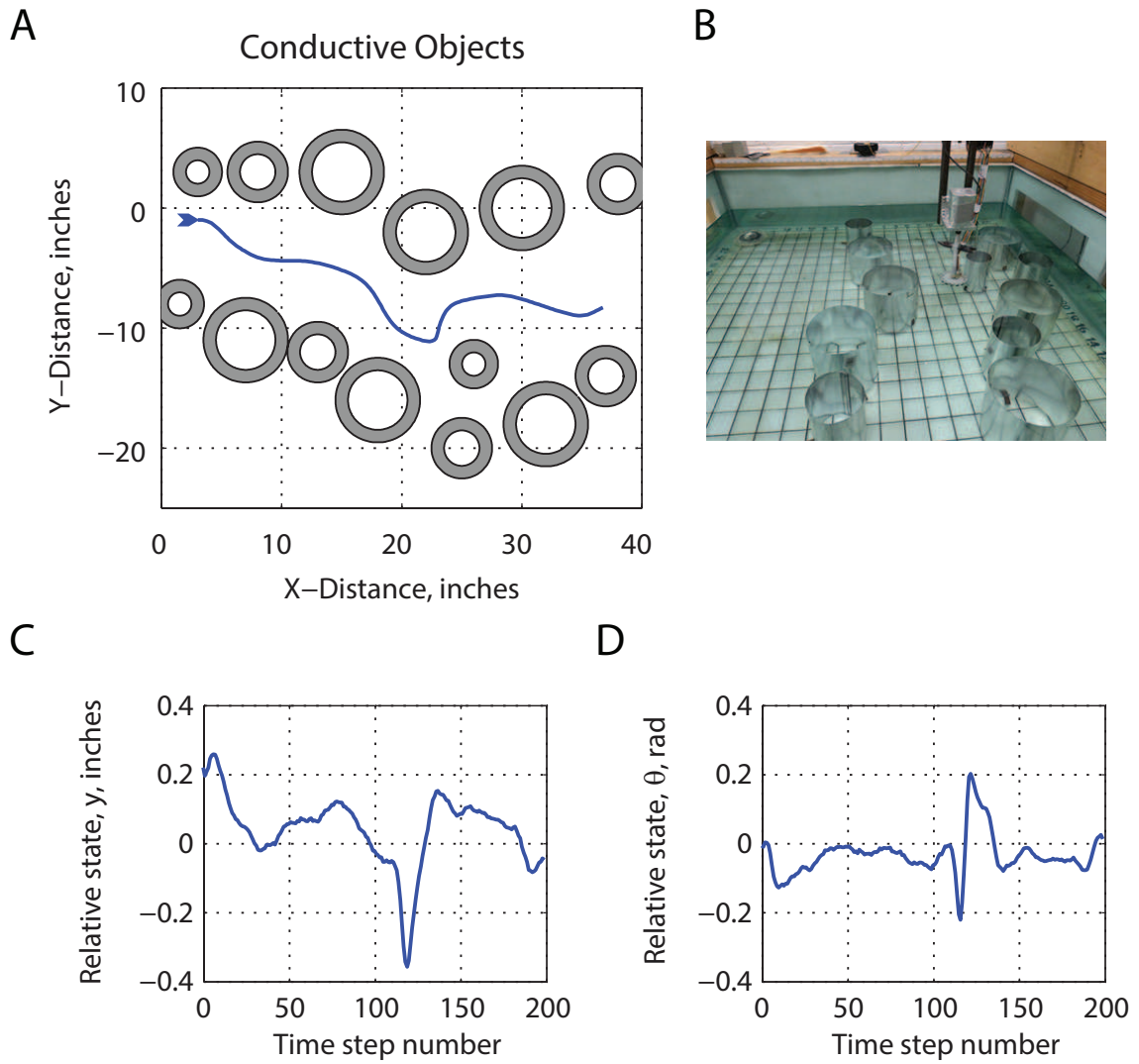
Figure 5.14: Experiment demonstrating obstacle avoidance in a cluttered corridor constructed with non-conducting cylinders, (A) Trajectory, (B) Experimental setup, (C) Time trace of relative state, $\hat{y}$, (D) Time trace of relative states, $\hat{\theta}$.

cylinders without any collisions as is evident from Figure 5.14A. Near the small cylinder in the corridor acting as a small obstacle, the vehicle made a sharp turn away in order to avoid colliding with it. The relative states plotted in Figure 5.14C and D stay close to zero after the initial adjustment except for the time when the vehicle encounters the small cylinder in its course. At this point, a large correction is made by the controller due to the occurrence of the peak in the state estimates.

A

B

Figure 5.15: Effect of variation in initial conditions on trajectories in a cluttered corridor comprising of non-conductive cylinders, (A) Variation in initial lateral offset, (B) Variation in initial angular offset

The consistency and repeatability of the controller was tested by varying the initial conditions, one variable at a time. In all the cases, convergence of trajectories was observed irrespective of the initial conditions which can be seen in Figure 5.15.

5.5.2.3 Conductive and Non-conductive Cylinders

In this case, both types of cylinders, steel and PVC, were used. It was realized that any random arrangement of the cylinders would not work. If a conductive and a non-conductive cylinder were placed next to each other, the resulting electric image was observed to be smaller in magnitude and wider. These images would fool the controller in thinking that the vehicle was away from the objects and it would move the vehicle close to them. In many cases, the vehicle would simply collide with the objects due this misinterpretation by the controller. Hence, after a lot of failed attempts to use a random arrangement of cylinders, a simpler arrangement was finalized. Here, the corridor was formed with all the conductive cylinders on its one side and non-conductive cylinders on the other. This arrangement is analogous to the tunnel case with one conductive wall and one non-conductive wall. The arrangement is shown in Figure 5.16B.

The trajectory is shown in Figure 5.16A. It can be seen to approach the non-conductive cylinders in the initial stage of its journey. This behavior is consistent with the results from the mixed conductivity tunnel case. However, on getting very close to such a cylinder, the controller made a big correction to avoid colliding. This correction made the vehicle traverse a path which goes close to the conductive cylinders. However, the vehicle can be seen to move away from the conductive cylinders by the end of its journey. The gains of $K_y = 20$ and $K_\theta = 40$ were used. The big correction made by the controller is a result of higher values of relative estimate $\hat{y}$ near the start of the trial as seen in Figure 5.16C. This relative state
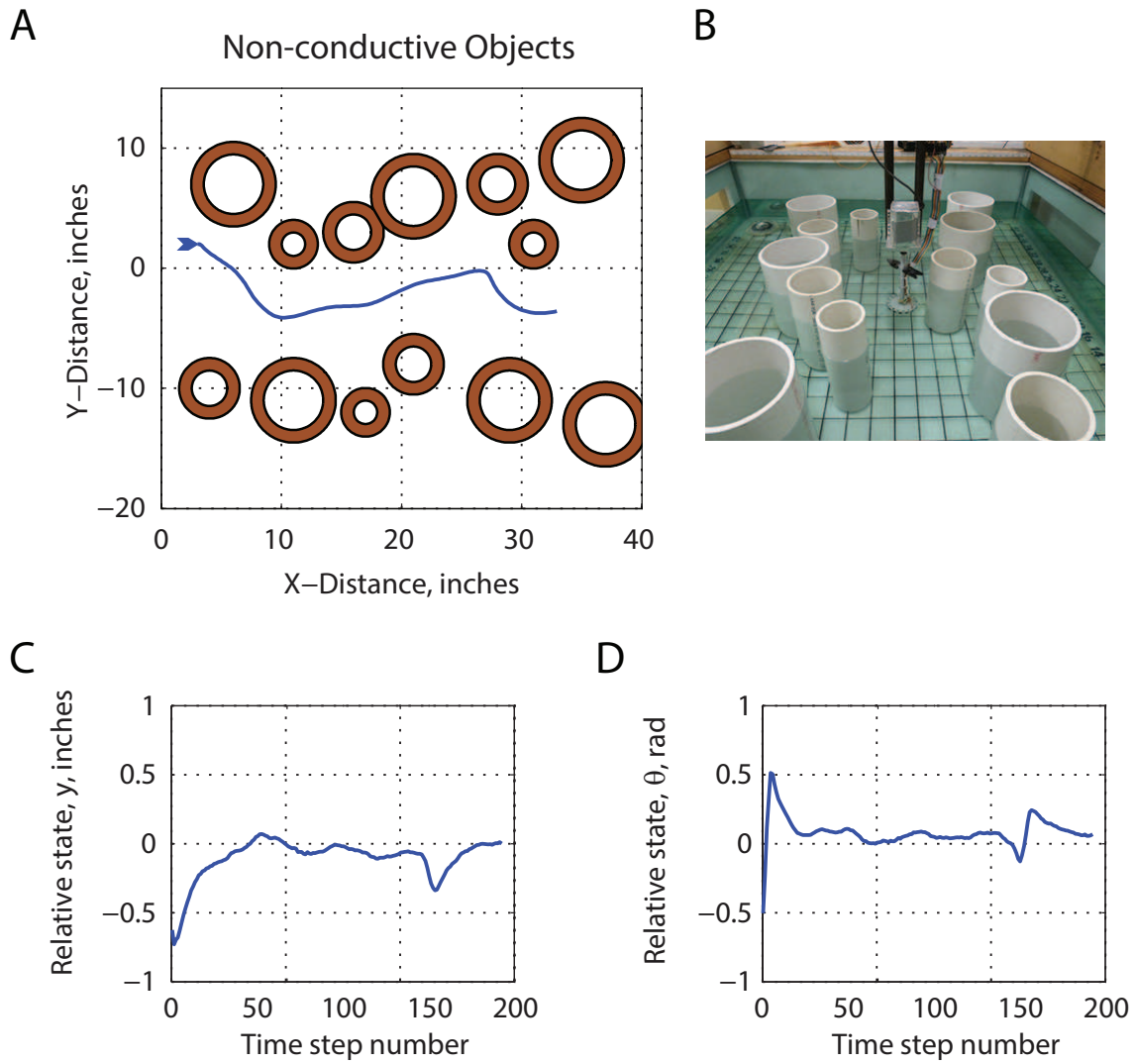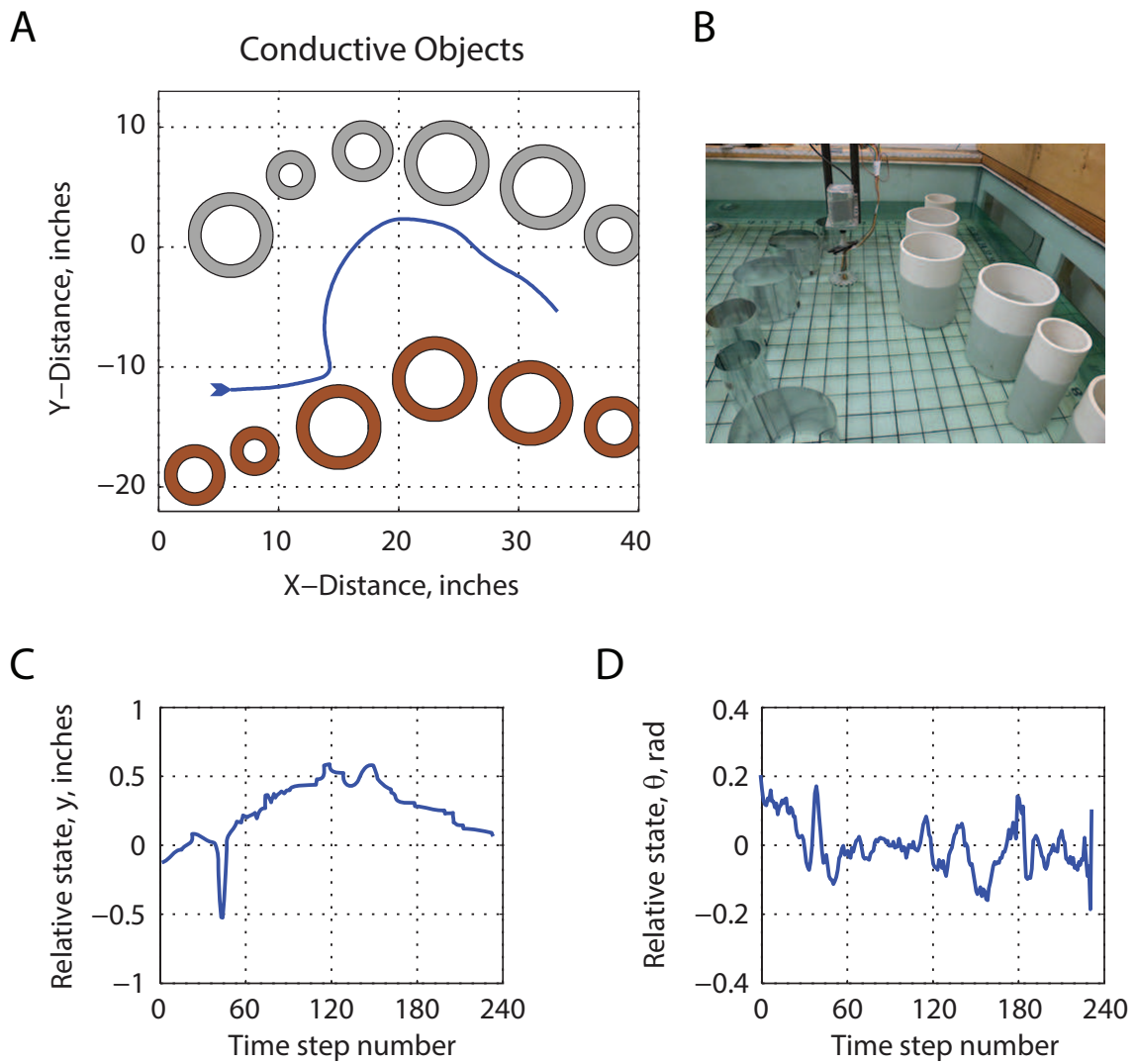
Figure 5.16: Experiment demonstrating obstacle avoidance in a cluttered corridor constructed with conductive cylinders on one side and non-conductive cylinders on the other, (A) Trajectory, (B) Experimental setup, (C) Time trace of relative state, $\hat{y}$, (D) Time trace of relative states, $\hat{\theta}$

stays positive for the rest of the experiment which indicates locations closer to the conductive cylinders. Towards the end of the experiment, it is seen to decrease to zero indicating the attempt made by the controller to move closer to the non-conductive cylinders.
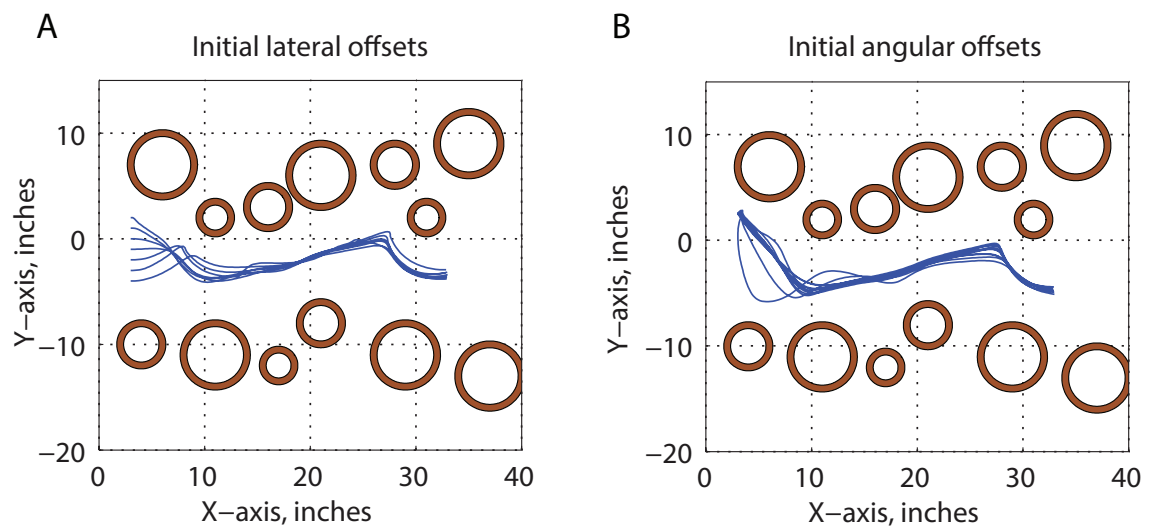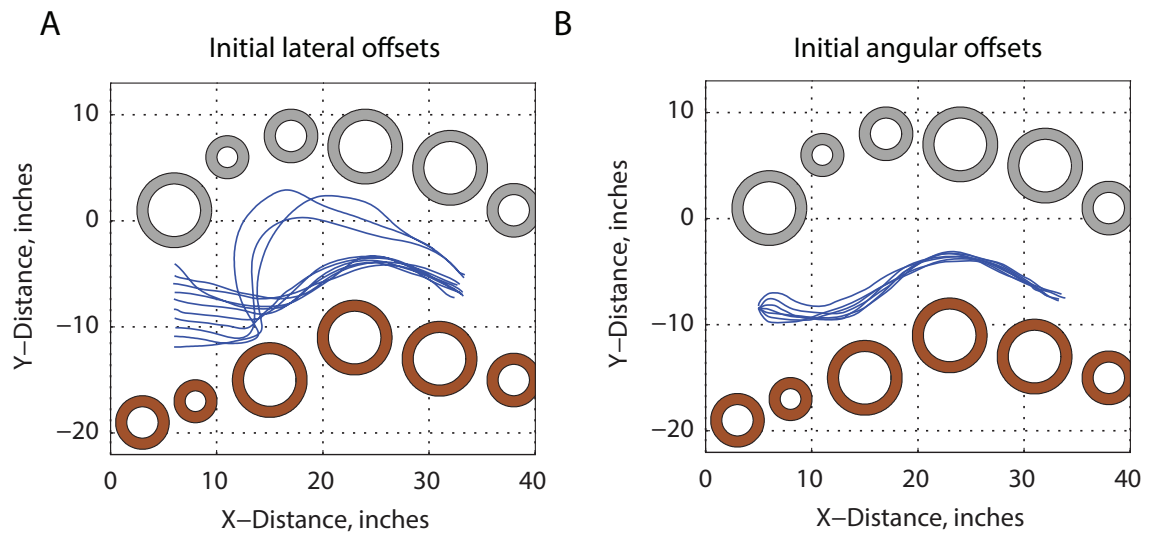

Figure 5.17: Effect of variation in initial conditions on trajectories in a cluttered corridor comprising of conductive and non-conductive cylinders, (A) Variation in initial lateral offset, (B) Variation in initial angular offset

Additional set of trials were performed with change in either the initial lateral offset or initial angular offset. It was observed that the vehicle stayed closer to the non-conductive cylinders in most of the cases as can be seen in Figure 5.17. The exceptions were the cases when the vehicle got very close to the non-conducting cylinders prompting the controller to make a big correction to avoid correction. Satisfactory level of convergence of trajectories was observed in these trials.

5.5.3 Obstacle Field

In these environments cylinders were arranged in a structured pattern providing as staggered obstacles for the vehicle. Walls were placed outside this arrangement of cylinders in order to prevent the vehicle escaping from the sides. Steel and PVC cylinders of 6 inches (15 cm) diameter and aluminum and wood plates were used to construct the environments. As before, three cases were considered, first with all conductive cylinders and conducting walls, second with non-conductive cylinders and walls and the third with a mix of conductive and non-conductive walls and walls. Due to the placement of the cylinders, the trajectory which provides least obstruction was taken, out of the presented choices. This is a property of reflexive obstacle avoidance. In this problem, there exist multiple steady state conditions unlike the previous problems where unique steady state conditions existed. Here the steady state condition can be defined as the locus of all the points between the cylinders where the electric perturbations in the left and right halves of the electric image are equal. This is a generic definition and in this problem could result into many such co-existing loci.

5.5.3.1 Conductive Cylinders

The obstacle field was constructed by placing the cylinders at an equal distance from all its neighbors. The aluminum plates were used to prevent the vehicle from escaping from the sides of the environment. The arrangement can be seen in Figure 5.18B.

Figure 5.18: Experiment demonstrating obstacle avoidance in an obstacle field comprising of conductive cylinders, (A) Trajectory, (B) Experimental setup, (C) Time trace of relative state, $\hat{y}$, (D) Time trace of relative states, $\hat{\theta}$

The relative states are plotted in Figure 5.18C and D staying closer to zero. The gains of $K_y = -20$ and $K_\theta = -40$ were used.

Figure 5.19: Effect of variation in initial conditions on trajectories in an obstacle field comprising of conductive cylinders, (A) Variation in initial lateral offset, (B) Variation in initial angular offset

Initial conditions were varied, one out of two variables at a time and trials were performed. It was observed that the vehicle traversed through the environment without any collisions and achieved satisfactory level of convergence of trajectories as shown in Figure 5.19. More interestingly, it took a path from either side of the central cylinders. The trajectories arriving from either side of the central cylinders towards the end did not converge afterwards and continued their course since there were no more objects present to induce a turn in the trajectories to initiate convergence.

5.5.3.2 Non-conductive Cylinders

In this case, all the cylinders that were used to build the environment were made out of PVC and the barricade walls were made out of wood. This case is similar to the conductive cylinders case above except that the value of the gains selected here were $K_y = 30$ and $K_\theta = 60$. The environment is shown in Figure 5.20B.

No collisions occurred while the vehicle traversed through the environment as seen from the trajectory plot in Figure 5.20A. The relative state estimates in Figure 5.20C and D converge and stay close to zero indicating the attainment of the steady state.

On varying the initial conditions, the vehicle was found to take the path of least resistance around the central cylinders. Satisfactory level of convergence was also observed as seen in Figure 5.21.

5.5.3.3 Conductive and Non-conductive Cylinders

In this case both, steel and PVC cylinders were used to build the environment. The issue of juxtaposed objects encountered in the cluttered corridor problem consisting of both types of objects was not experienced here since all the cylinders maintained a certain a distance from all their neighbors. So the cylinders were placed randomly as shown in Figure 5.22B.

As seen from the trajectory plot in Figure 5.16A, the vehicle made some turn maneuvers where it was not expected to. The vehicle made a turn just before the final central cylinder but it eventually corrected for this turn and completed
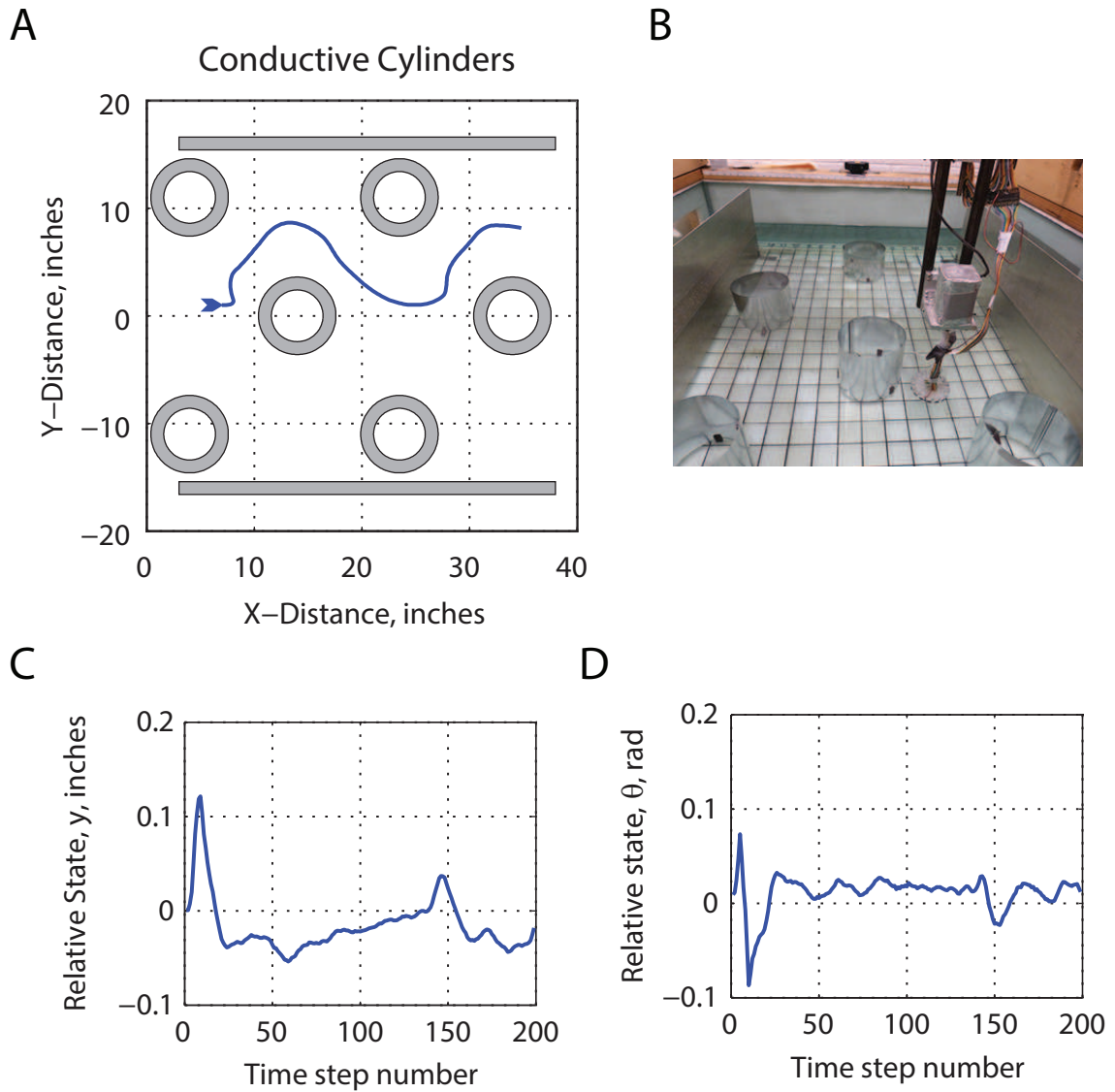
Figure 5.20: Experiment demonstrating obstacle avoidance in an obstacle field comprising of non-conductive cylinders, (A) Trajectory, (B) Experimental setup, (C) Time trace of relative state, $\hat{y}$, (D) Time trace of relative states, $\hat{\theta}$
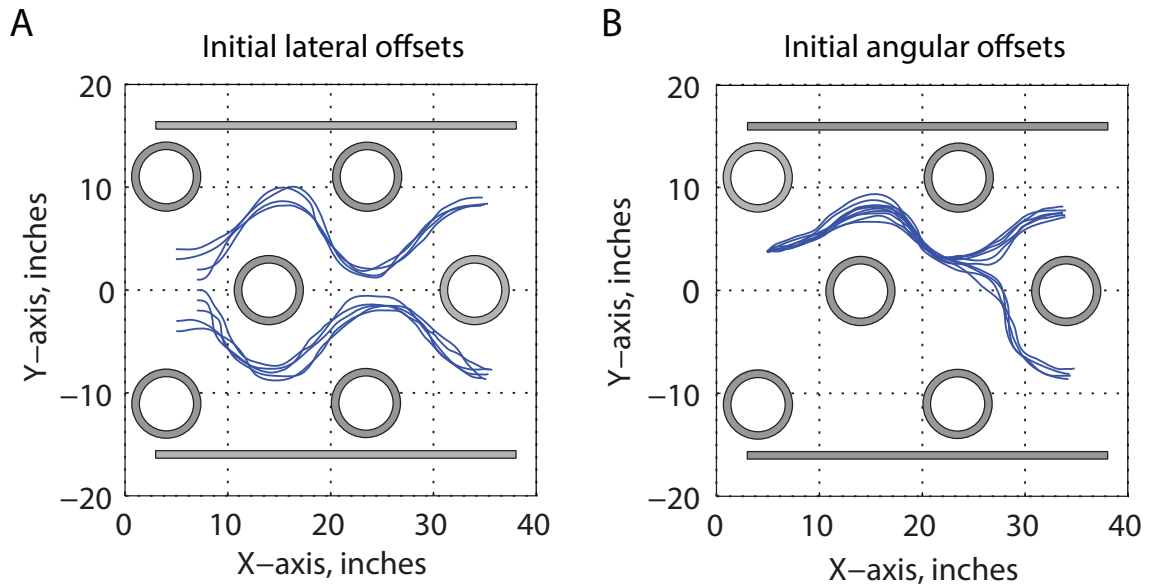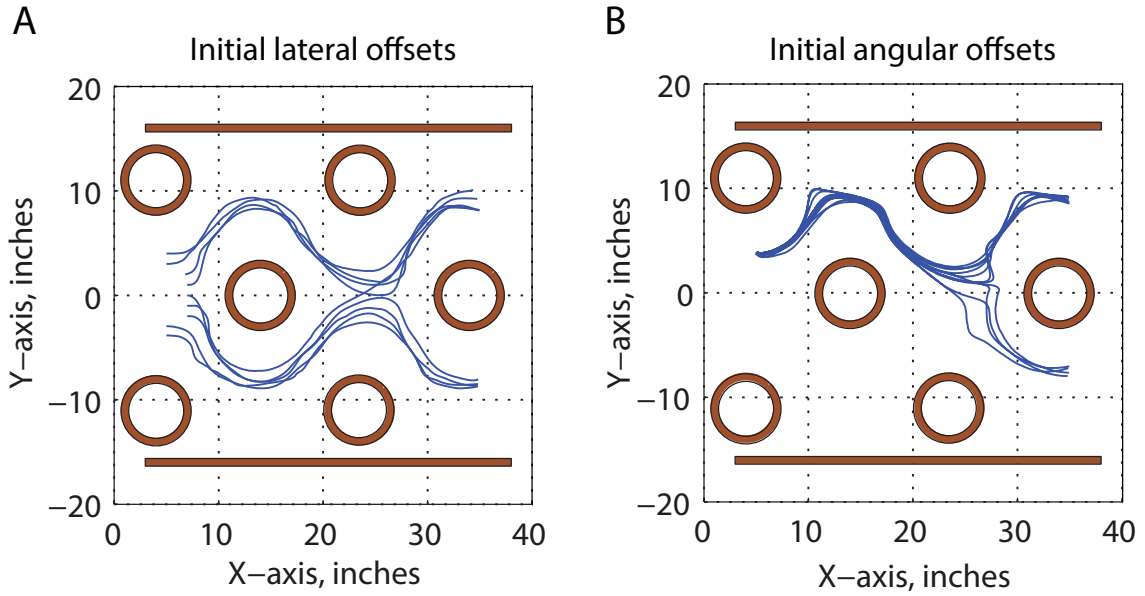
Figure 5.21: Effect of variation in initial conditions on trajectories in an obstacle field comprising of non-conductive cylinders, (A) Variation in initial lateral offset, (B) Variation in initial angular offset

its journey. This random turning behavior could be attributed to the difference in magnitudes of the electric image due to the two types of objects. The vehicle tried to move away from the central conductive object at the right side of the environment and towards the first central non-conductive object. So a turn was induced to complete this operation. However the vehicle sensed the second conductive object in the top row and corrected it path soon afterwards. This explanation was inferred from the relative states in Figure 5.22C where a dip in the state estimate $\hat{y}$ occurs due to the presence of a non-conductive object nearby and signals the controller to make the turn mentioned above. Similarly a positive peak indicates a conductive object nearby triggering the corrective turn.

Similar random turn maneuvers were also experienced when the initial condi-
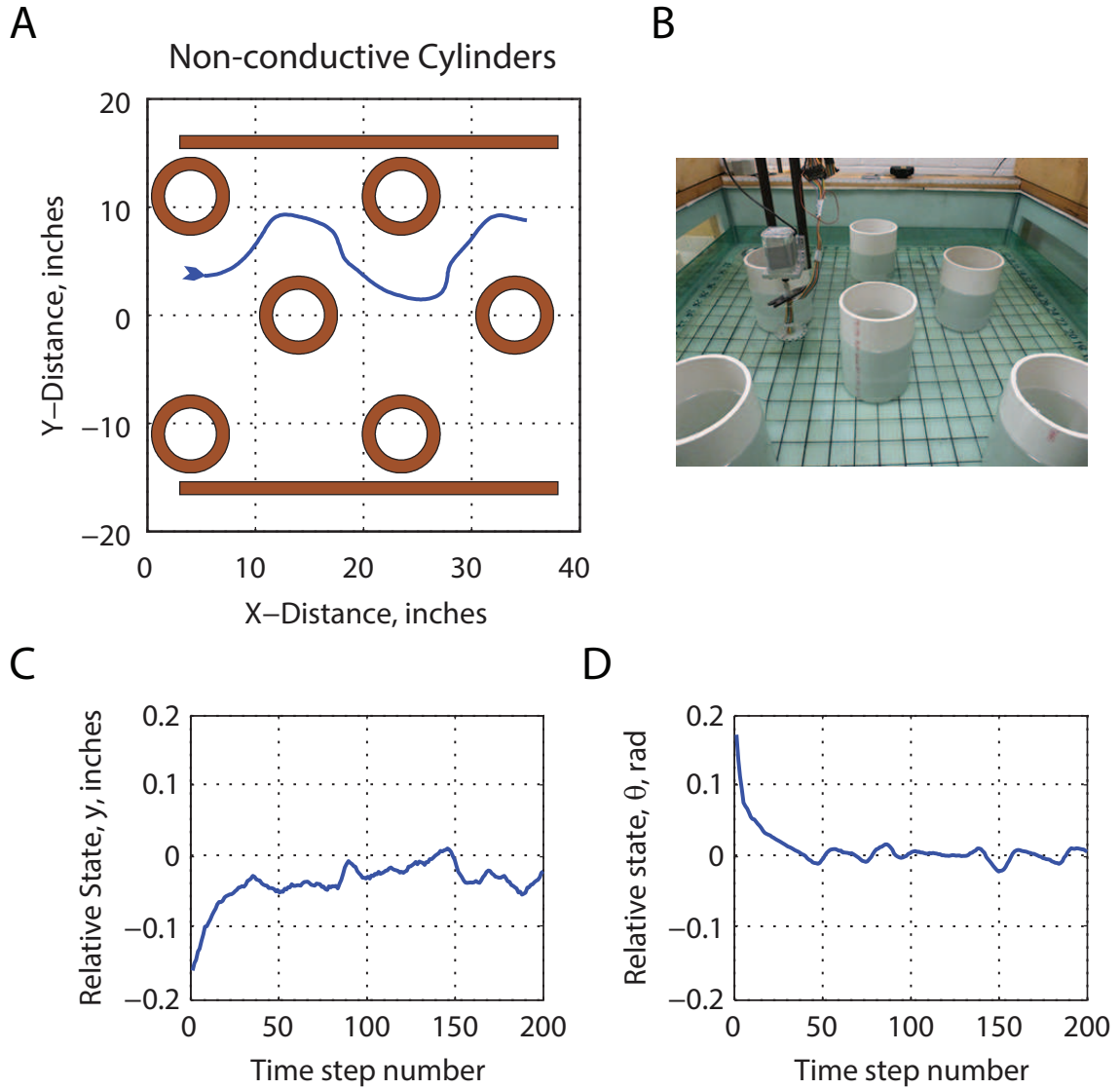
A **Conductive Cylinders**

B

C

D
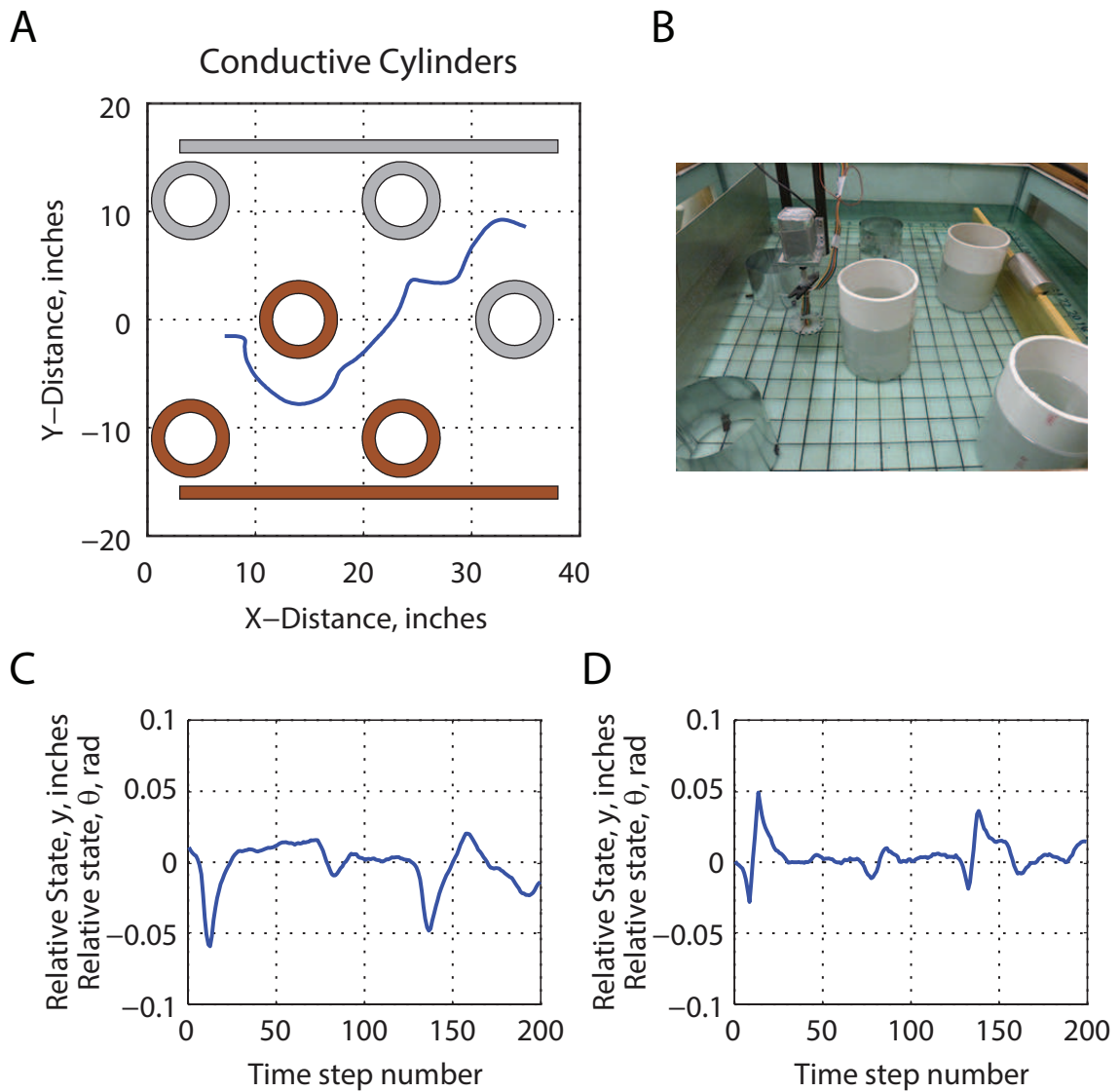
Figure 5.22: Experiment demonstrating obstacle avoidance in an obstacle field comprising of conducting and non-conductive cylinders, (A) Trajectory, (B) Experimental setup, (C) Time trace of relative state, $\hat{y}$, (D) Time trace of relative states, $\hat{\theta}$
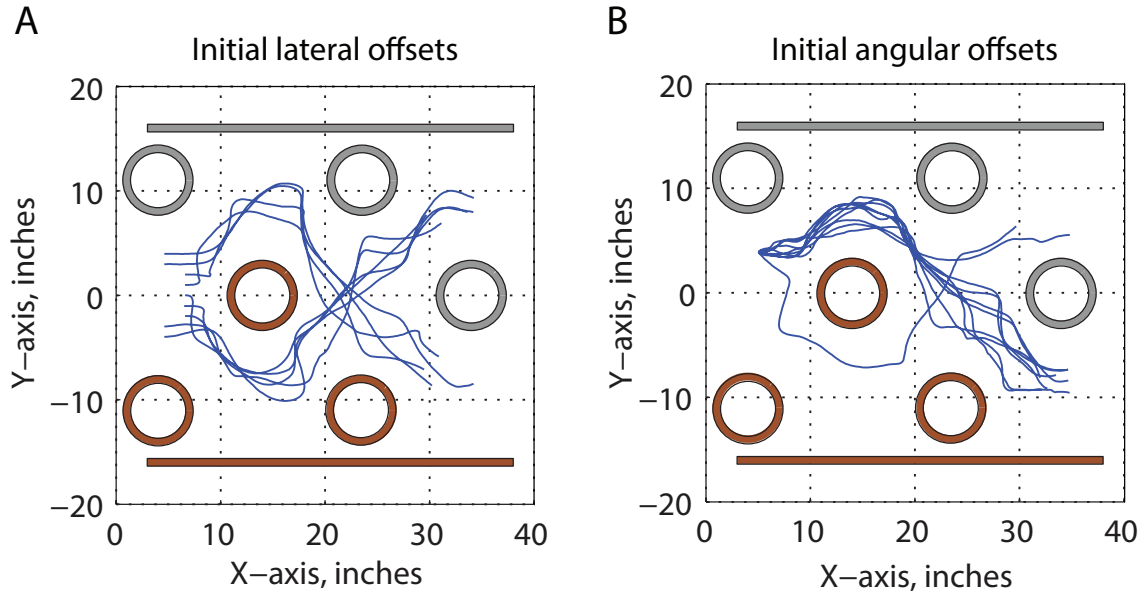
Figure 5.23: Effect of variation in initial conditions on trajectories in an obstacle field comprising of conductive and non-conductive cylinders, (A) Variation in initial lateral offset, (B) Variation in initial angular offset

tions were varied. These turn maneuvers make the trajectories jagged, but collisions were avoided in all the cases. The corresponding plots are shown in Figure 5.23.

There is a clear agreement between the simulation and experimental results. The inferences drawn from the observations in all the previous work have been summed up in the following Chapter. In addition the scope for future work is also discussed.

Chapter 6

Conclusions and Future Work

This study was set out to explore the possibility of use of electric images in performing reflexive obstacle avoidance in different environments in an attempt to mimic the navigational technique called electrolocation found in some electric fishes. In that respect, an electrostatics based model was developed to represent the electric images formed due to objects of simpler geometries. Wide-Field Integration (WFI) methodology was applied to extract proximity information from the above electric images in order to develop a general control strategy to perform autonomous navigation. Simulations demonstrating obstacle avoidance behaviors were generated using this control strategy. For hardware implementation, an electro-sensor and an experimental setup were designed and constructed. The same control strategy also proved useful in performing autonomous navigation and obstacle avoidance behaviors. While previous attempts at performing such tasks using electrolocation have been made, this study sought to achieve this goal by designing a controller that is computationally efficient and easy to implement on hardware with limited computational capabilities.

Following is the list of key findings and their technical implications.

1. In Chapter 2, the equations for electric images due to objects of simple ge-
   ometries were derived using principles from electrostatics. Of particular in-
   terest was the formulation for a straight tunnel. For deriving this equation,
   a technique called method of images was used. This subsequently allowed us
   to apply mathematical techniques to design weighting patterns that decode
   relevent information from electric image measurements.

Chapter 3: Control Strategy

2. In Chapter 3, the procedure to map an electric image directly to actuator
   commands was described. This consisted of two tasks, WFI processing of the
   electric image to obtain optimal estimates of relative states and linear feedback
   control.

3. WFI processing calls for computing inner products of the electric image with
   various sensitivity functions followed by linearization of the outputs of the
   inner products. The linearized equations directly relate the sensory signal
   i.e. the electric image with proximity information such as relative position
   and orientation. Since the electric image equations are difficult to integrate,
   a numerical scheme to perform the inner product operation was developed.
   Another routine was developed to linearize these inner products by performing
   numerical differentiation.

4. The linearized equations revealed that the number of WFI harmonics that

contained information about the states was more than the number of states. In other words, different sensitivity functions brought out different information from the electric image about the states of the vehicle. This resulted in a skinny C matrix on arranging the harmonics in the standard output form $v = Cx$. Thus the system of WFI equations became overdetermined due to the presence of more WFI outputs than the number of states involved. This is particularly helpful in optimal state estimation since the solution to the system of equations exists only if the above criteria is satisfied.

5. By inverting the set of linearized WFI outputs, the relative states of the system were computed. To minimize the error between the actual and relative states, a linear least squares estimation scheme was used. The end result of this process was a set of state extraction functions. Inner products between an electric image and the state extraction functions yielded the relative states in one step. This is a very desirable quality for hardware implementation.

6. The state extraction functions for y and θ states were computed to be $\sin(\gamma)$ and $\sin(2\gamma)$ respectively. The inner product between an electric image and $\sin(\gamma)$ yielded a positive value if the peak of the electric image existed between $0°$–$180°$ of the sensor. Such an electric image was formed if the sensor was close to an object on its right. A negative value indicated an object on the left side and a peak in the $180°$–$360°$ of the sensor. Thus this state extraction function was helpful in estimating the relative lateral offset from the centerline of a tunnel. On the other hand a zero value for the inner product between the

131

electric image and $\sin(2\gamma)$ function indicated a motion parallel to the tunnel walls. Any deviation from zero indicated a direction of travel along a direction in one of the four quadrants. Thus this function computes the relative angular offset of the vehicle with respect to the centerline of the tunnel.

7. It was shown using elementary simulations that different behaviors like centering (in a tunnel) and wall following (in a circular arena) could be achieved by selecting the appropriate steady state while designing the state extraction functions.

8. It can also be noticed that this entire procedure did not require computing the actual kinematic states or the distances of the objects. Nor did it need any prior knowledge of the environment. These qualities made the algorithm computationally efficient and easily integrable with hardware. It was possible to pre-compile and hard-code the state extraction functions in the controller due to their static nature, thus saving a lot of on-board computational effort.

Chapter 4: Quasistatic Simulations

9. FEM based quasistatic simulations were used to simulate environments consisting non-conductive as well as complex shaped objects. In addition the electric field was made oscillatory. Quasistatic approximation for an oscillatory electric field enabled the use of the methods and state extraction functions derived for electrostatic electric images.

10. The state extraction functions were designed for a straight tunnel but they

were found to work for other environments as well. The reasoning behind this was that the algorithm viewed every environment as a local tunnel and computed relative states accordingly. Thus as long as there are objects on either side of the sensor, this control strategy should work.

11. The scope of the state extraction functions is limited in that they apply to environments comprised of conductive objects. Hence modifications were suggested to make the same state extraction functions work for non-conductive objects as well. The obvious implication of this was that the control strategy could now be used for a larger variety of environments.

12. Normally FEM simulations are computationally heavy and time consuming. However, the background operation and localized refining of meshes adopted in this study made the process less arduous and quick. It was assumed that there were no noise sources present in the environments. This assumption although unrealistic, helped develop a better understanding of the process. In addition, this criteria also helped in tuning the controller gains. Controller gains designed this way provided a starting value of gains for all other simulations and even for experiments. In theory, fine adjustments to these gains should give the actual gains necessary in a particular situation.

13. The simulations suggested that the algorithm is quite robust to initial conditions and nature of objects perturbing the electric field of the sensor.

14. The controller was also found to be robust to slight changes in the corridor

width.

Chapter 5: Experimentation

15. The electro-sensor was designed to measure the electric field and perturbations to it in the plane of its disc. Rapid prototyped body of the sensor ensured perfect alignment of the electro-receptors in this plane. The source electrode was located on the bottom of the disc at its center. This location was favorable since a symmetric electric field could be generated in all direction. The gantry was designed and constructed to move the sensor at rapid rates and through large distances while providing a positioning accuracy of 0.001 inch (0.025 mm).

16. For mitigating noise in the readings, digitally filtered data was further fitted with a sine wave in a least squares fashion. Performing these operations was necessary to minimize the effect of noise on the RMS value computed off of the captured data.

17. EMI noise induced due to the stepper motors was considered to be an undesirable influence on electric images and was extremely difficult to get rid of using traditional filtering. Hence, the stepper motors were stopped before recording the electric images and started back again before the issuing of the command to move the gantry. This introduced a start and stop motion to the experiments however. Multithreading was used to perform some of the tasks in parallel. This was helpful in keeping the idle time of the gantry to a

minimum during experiments.

18. The experiments showed that the controller was robust to initial conditions, noise and environment structure.

19. Finally, the entire WFI routine and the control strategy was confirmed to be computationally very efficient and suitable for implementing on a real robot.

6.1 Future Work

The study has offered an evaluative perspective on autonomous navigation using electrolocation. In future, certain improvements can be made to the current state of this project. Additionally, the study encountered a few limitations, which also need to be considered in the future work.

The scope of the project was limited to planar electric fields and computations thereof. With 3D enhancements, to the sensor and the algorithm, it might become feasible to mount the sensor on a 6 DOf platform. The sensor itself can be modified in order to make compact and modular. With improvement in the sensor, the algorithm and the controller would require improvements as well. Another limitation of this study was that a random arrangement of objects was not possible. Finally, the gantry robot performed exceptionally in experiments and furnished some very good results. However, due to EMI issues, it was required to start and stop the motors while recording electric images, thus sacrificing continuous motion of the vehicle. This issue can be addressed in future as well.

Accordingly, the future work is divided into four categories. These are sensor

design, algorithm, environments and hardware.

6.1.1 Sensor Design

The sensor can be modified to measure electric images due to objects in entire 3D space and not just in the plane of the sensor's disc. For this purpose, a sensor consisting of three orthogonal discs can be constructed. However, a better option would be to construct a sphere with electro-receptors spread all over. Full spherical measurements of electric images provide redundancy and hence better quality electric images.

Another improvement in the sensor can be in the form of smaller and custom made electro-receptors. In the current version, EKG sensors were used as electro-receptors. However these receptors are large and bulky. Instead, tiny MEMS type sensors can be custom-made and used. This can facilitate construction of small and compact sensors. Further in future, the spherical sensor can be modified into a fish shaped sensor by performing conformal mapping. Such a sensor will promote a higher degree of bio-mimicking.

6.1.2 Algorithm

With improvements in sensor, the algorithm will be required to process 3D electric images of larger array of receptors. Another implication of this upgrade is that 2D sensitivity functions could no longer be used to perform WFI processing of the 3D electric images. Fourier harmonics were used in this study, whereas spherical

harmonics can be one of the candidate sets of the sensitivity functions for processing 3D electric images. For a fish shaped sensor, the algorithm will need to include fish kinematics instead of unicycle kinematics. As another enhancement to the algorithm, a dedicated robust controller, like a H_∞ loop shaping controller can be used to mitigate noise and disturbance introduced in the system through various sources.

6.1.3 Environments

It was observed in the experiments in cluttered corridors that a conductive and a non-conductive object could not be placed next to one another as this arrangement becomes almost invisible to the algorithm. So these type of environments were never used. The algorithm can be developed to test in such environments which were not considered in this study. The complete knowledge of the reasons for corruption of electric images in such cases can be useful in reverse processing such images to arrive at the original images.

6.1.4 Hardware

The current experimental setup was shown to perform autonomous navigation in different environments. However, it was required to be stopped while recording electric images and started back again for motion afterwards. This was done to prevent EMI induced noise entering the captured readings. One way to solve this issue is by designing better magnetic field shields around the motors. Another

approach that is often suggested against such issues is to completely redesign the drive system.

With the development of a fish shaped sensor, the gantry would eventually become unnecessary as a propulsion system could be mounted with the vehicle carrying the sensor. In that case, shielding will be required for the motors driving this propulsion system.

The demonstration of obstacle avoidance in simulation and experiments proves that spatial sensitivity function based methodology can be extended for extracting relative states from electric images. In fact the major contribution of this work is the development of the procedure to extract relative proximity from electric images. Bio-inspired systems are a relatively new area in the robotics field. This work is significant in that bio-mimicking was achieved while utilizing WFI which is a signal processing and control algorithm that was modeled by studying insects. Hence, this algorithms are highly efficient with regards to implementation. WFI processing has a marked advantage that a static feedback controller is used instead of dynamic controllers [31, 35]. The inner product operation is comparatively simple and can be used to compute the navigational parameters from an electric image in a single step. The property of conservation of computational resources makes this WFI based algorithm highly efficient and greatly simplifies hardware and software implementation.

Bibliography

[1] Widditsch HR. SPURV-The first decade. DTIC Document; 1973.

[2] Sariel S, Balch T, Erdogan N. Naval mine countermeasure missions. Robotics & Automation Magazine, IEEE. 2008;15(1):45–52.

[3] Griffiths G. 6. In: Griffiths G, editor. Technology and applications of autonomous underwater vehicles. vol. 2. CRC Press; 2002. p. 93–108.

[4] Kondo H, Ura T. Navigation of an AUV for investigation of underwater structures. Control engineering practice. 2004;12(12):1551–1559.

[5] Tivey MA, Johnson HP, Bradley A, Yoerger D. Thickness of a submarine lava flow determined from near-bottom magnetic field mapping by autonomous underwater vehicle. Geophysical Research Letters. 1998;25(6):805–808.

[6] Humbert JS, Hyslop AM, Chinn M. Experimental Validation of Wide-Field Integration Methods for Autonomous Navigation. In: Proceedings IEEE/RSJ International Conference on Intelligent Robots and Systems. San Diego, California, USA; 2007. p. 2144–2149.

[7] Marques C, Lima P. Avoiding obstacles-multisensor navigation for nonholonomic robots in cluttered environments. Robotics & Automation Magazine, IEEE. 2004;11(3):70–82.

[8] Conroy J, Gremillion G, Ranganathan B, Humbert JS. Implementation of wide-field integration of optic flow for autonomous quadrotor navigation. Autonomous robots. 2009;27(3):189–198.

[9] Horiuchi T, Cheely M. Analog VLSI Models of Range-Tuned Neurons in the Bat Echolocation System. EURASIP J Advances in Signal Processing;2003.

[10] Palmer T, Ribas D, Ridao P, Mallios A. Vision based localization system for auv docking on subsea intervention panels. In: OCEANS 2009-EUROPE. IEEE; 2009. p. 1–10.

[11] Petillot Y, Tena Ruiz I, Lane DM. Underwater Vehicle Obstacle Avoidance and Path Planning Using a Multi-Beam Forward Looking Sonar. IEEE J Oceanic Eng. 2001 Apr;26:240–251.

[12] Aulinas J, Petillot YR, Lladó X, Salvi J, Garcia R. Vision-based underwater SLAM for the SPARUS AUV. In: International Conference on Computer and IT Applications in the Maritime Industries (COMPIT); 2011. p. 171–181.

[13] Lissmann HW. On the function and evolution of electric organs in fish. Journal of Experimental Biology. 1958;35(1):156–191.

[14] Assad C, Rasnow B, Stoddard PK. Electric organ discharges and electric images during electrolocation. J of Exp Biol. 1999;202(10):1185–1193.

[15] Kashimori Y, Goto M, Kambara T. Model of P-and T-electroreceptors of weakly electric fish. Biophysical journal. 1996;70(6):2513–2526.

[16] Bastian J. Electrolocation: Behavior, Anatomy and Physiology. In: Bullock TH, Heiligenberg W, editors. Electroreception. John Wiley and Sons; 1986. p. 577–612.

[17] Bodznick D, Montgomery JC. The physiology of low-frequency electrosensory systems. In: Bullock TH, Hopkins CD, Popper AN, Fay RR, editors. Electroreception. Springer; 2005. p. 132–153.

[18] Nelson ME. Target Detection, Image Analysis, and Modeling. In: Bullock TH, Hopkins CD, Popper AN, Fay RR, editors. Electroreception. Springer; 2005. p. 290–317.

[19] Budelli R, Caputi AA. The electric image in weakly electric fish: perception of objects of complex impedance. Journal of Experimental Biology. 2000;203(3):481–492.

[20] Von der Emde G. Active electrolocation of objects in weakly electric fish. J of Exp Biol. 1999;202(10):1205–1215.

[21] Caputi AA, Budeli R. Peripheral electrosensory imaging by weakly electric fish. J Comp Physiol A. 2006;192:587–600.

[22] MacIver MA, Nelson ME. Towards a Biorobotic Electrosensory System. Autonomous Robots. 2001;11:263–266.

[23] Lissmann HW, Machin KE. The Mechanism of Object Location in Gymnarchus Niloticus and Similar Fish. J Exp Biol. 1958;35:451–486.

[24] Lissmann HW. Electric Location by Fishes. Scientific American. 1963 March;208(3):56–65.

[25] Knudsen EI. Spatial aspects of the electric fields generated by weakly electric fish. Journal of comparative physiology. 1975;99(2):103–118.

[26] Rasnow B. The effects of simple objects on the electric field of Apteronotus. J Comp Physiol A. 1996;178(3):397–411.

[27] Caputi A, Budelli R, Grant K, Bell CC. The electric image in weakly electric fish: physical images of resistive objects in Gnathonemus petersii. Journal of experimental biology. 1998;201(14):2115–2128.

[28] Fujita K, Kashimori Y. Modeling the electric image produced by objects with complex impedance in weakly electric fish. Biological cybernetics. 2010;103(2):105–118.

[29] Chetty G, Russell A. Electric field based sensing for underwater vehicle guidance. In: Proc. of the 2nd Intl. Conf. on Bioelectromagnetism. Melbourne, Australia; 1998. .

[30] Nguyen N, Wiegand I, Jones DL. Sparse beamforming for active underwater electrolocation. In: Acoustics, Speech and Signal Processing, 2009. ICASSP 2009. IEEE International Conference on. IEEE; 2009. p. 2033–2036.

[31] Solberg JR, Lynch KM, MacIver MA. Active Electrolocation for Underwater Target Localization. Intl J of Robotics Research. 2008 May;27(5):529–548.

[32] Neveln ID, Bai Y, Snyder JB, Solberg JR, Curet OM, Lynch KM, et al. Biomimetic and bio-inspired robotics in electric fish research. The Journal of experimental biology. 2013;216(13):2501–2514.

[33] Snyder J, Silverman Y, Bai Y, MacIver MA. Underwater object tracking using electrical impedance tomography. In: Intelligent Robots and Systems (IROS), 2012 IEEE/RSJ International Conference on. IEEE; 2012. p. 520–525.

[34] Lebastard V, Chevallereau C, Amrouche A, Jawad B, Girin A, Boyer F, et al. Underwater robot navigation around a sphere using electrolocation sense and Kalman filter; 2010. p. 4225–4230. Cited By (since 1996) 3.

[35] Lebastard V, Chevallereau C, Girin A, Servagent N, Gossiaux PB, Boyer F. Environment reconstruction and navigation with electric sense based on a Kalman filter. The International Journal of Robotics Research. 2013;32(2):172–188.

[36] Boyer F, Lebastard V, Chevallereau C, Servagent N. Underwater reflex navigation in confined environment based on electric sense. IEEE Transactions on Robotics. 2013;29(4):945–956.

[37] Franz MO, Krapp HG. Wide-field, motion- sensitive neurons and matched filters for optic flow fields. Biological Cybernetics. 2000;83:185–197.

[38] Franz MO, Chahl JS, Krapp HG. Insect-inspired estimation of egomotion. Neural computation. 2004;16(11):2245–2260.

[39] Egelhaaf M, Kern R, Krapp HG, Kretzberg J, Kurtz R, A W. Neural Encoding of Behaviourally Relevant Visual-Motion Information in the Fly. Trends in Neurosciences. 2002;25:96–102.

[40] Borst A, Haag J. Neural networks in the cockpit of the fly. Journal of Comparative Physiology A. 2002;188(6):419–437.

[41] Humbert JS, Frye MA. Extracting Behaviorally Relevant Retinal Image Motion Cues via Wide-Field Integration. In: Proceedings American Control Conference. Minneapolis, Minnesota, USA; 2006. p. 2724–2729.

[42] Humbert JS, Murray RM, Dickinson MH. Sensorimotor convergence in visual navigation and flight control systems. In: Proceedings 16th IFAC World Congress. Praha, Czech Republic; 2005. .

[43] Humbert JS, Murray RM, Dickinson MH. A Control-Oriented Analysis of Bioinspired Visuomotor Convergence. In: Proceedings 44th IEEE Conference on Decision and Control, and the European Control Conference. Seville, Spain; 2005. p. 245–250.

[44] Humbert JS, Conroy JK, Neely CW, Barrows G. Wide-Field Integration Methods for Visuomotor Control. In: Floreano D, Zufferey JC, Srinivasan MV, Ellington C, editors. Flying Insects and Robots. Springer Verlag; 2009. .

[45] Humbert JS, Hyslop AM. Bio-Inspired Visuomotor Convergence. IEEE Transactions on Robotics. 2010 Feb;26(1):121–130.

144

[46] Hyslop A, Krapp H, Humbert JS. Control theoretic interpretation of directional motion preferences in optic flow processing interneurons. Biological Cybernetics. 2010;103(5):353–364.

[47] Humbert S, Conroy JK, Neely CW, Barrows GL. 5. In: et al DF, editor. Widefield integration methods for visuomotor control. Springer; 2009. p. 63–71.

[48] von der Emde G. Discrimination of objects through electrolocation in the weakly electric fish, Gnathonemus petersii. Journal of Comparative Physiology A. 1990;167(3):413–421.

[49] von der Emde G, Schwarz S. Imaging of objects through active electrolocation in Gnathonemus petersii. Journal of Physiology-Paris. 2002;96(5):431–444.

[50] von der Emde G, Fetz S. Distance, shape and more: recognition of object features during active electrolocation in a weakly electric fish. Journal of Experimental Biology. 2007;210(17):3082–3095.

[51] Caputi A, Budelli R. The electric image in weakly electric fish: I. A data-based model of waveform generation inGymnotus carapo. Journal of computational neuroscience. 1995;2(2):131–147.

[52] Rother D, Migliaro A, Canetti R, Gómez L, Caputi A, Budelli R. Electric images of two low resistance objects in weakly electric fish. Biosystems. 2003;71(1):169–177.

[53] Schwarz S, von der Emde G. Distance discrimination during active electroloca-
tion in the weakly electric fish Gnathonemus petersii. Journal of Comparative
Physiology A. 2001;186(12):1185–1197.

[54] Jackson JD. 2. In: Classical Electrodynamics. John Wiley and Sons; 1963. .

[55] Ida N. 4. In: Engineering Electromagnetics. Springer-Verlag; 2004. p. 205–206.

[56] Hyslop AM, Humbert JS. Autonomous Navigation in Three-Dimensional Ur-
ban Environments Using Wide-Field Integration of Optic Flow. Journal of
Guidance, Control and Dynamics. 2010 Jan – Feb;33(1):147–159.

[57] Crassidis JL, Junkins JL. 1.2.1. In: Optimal Estimation of Dynamic Systems.
Chapman & Hall/CRC; 2004. p. 9–13.

[58] Deng Z, Richmond MC, Simmons CS, Carlson TJ. Six-Degree-of-Freedom Sen-
sor Fish Design: Governing Equations and Motion Modeling. Pacific Northwest
National Laboratory (PNNL), Richland, WA (US); 2004.

[59] Dimble KD, Faddy JM, Humbert JS. Extraction of Relative Proximity from
Electrostatic Images Using Wide-Field Integration Methods. In: Proceedings
of the 2010 American Control Conference (ACC). Baltimore, MD; 2010. .

[60] Skogestad S, Postlethwaite I. Multivariable Feedback Control: Analysis and
Design. John Wiley & Sons; 2005.

[61] Zhou K, Doyle JC, Glover K. Robust and Optimal Control. Upper Saddle
River, NJ, USA: Prentice-Hall, Inc.; 1996.

[62] Lo YT. Electromagnetic field of a dipole source above a grounded dielectric slab. Journal of Applied Physics. 1954;25(6):733–740.

[63] Martin OJF, Dereux A, Girard C. Iterative scheme for computing exactly the total field propagating in dielectric structures of arbitrary shape. JOSA A. 1994;11(3):1073–1080.

[64] Michalski KA, Mosig JR. Multilayered media Green's functions in integral equation formulations. Antennas and Propagation, IEEE Transactions on. 1997;45(3):508–519.

[65] Simsek E, Liu QH, Wei B. Singularity subtraction for evaluation of Green's functions for multilayer media. Microwave Theory and Techniques, IEEE Transactions on. 2006;54(1):216–225.

[66] Ayatollahi M, Safavi-Naeini S. A new representation for the Green's function of multilayer media based on plane wave expansion. Antennas and Propagation, IEEE Transactions on. 2004;52(6):1548–1557.

[67] Knupp PM. Achieving finite element mesh quality via optimization of the Jacobian matrix norm and associated quantities. Part I–a framework for surface mesh optimization. International Journal for Numerical Methods in Engineering. 2000;48(3):401–420.

[68] Knupp PM. Achieving finite element mesh quality via optimization of the Jacobian matrix norm and associated quantities. Part II–a framework for volume

mesh optimization and the condition number of the Jacobian matrix. International Journal for Numerical Methods in Engineering. 2000;48(8):1165–1185.

[69] Ladeveze P, Pelle JP, Rougeot P. Error estimation and mesh optimization for classical finite elements. Engineering Computations. 1991;8(1):69–80.

[70] Bank RE, Sherman AH, Weiser A. Some refinement algorithms and data structures for regular local mesh refinement. Scientific Computing, Applications of Mathematics and Computing to the Physical Sciences. 1983;1:3–17.

[71] Bänsch E. Local mesh refinement in 2 and 3 dimensions. IMPACT of Computing in Science and Engineering. 1991;3(3):181–191.

[72] Reddy JN. An Introduction to the Finite Element Method (Engineering Series). 2nd ed. McGraw-Hill Education; 2006.

[73] Zienkiewicz OC, Taylor RL, Zhu JZ. The Finite Element Method: Its Basis and Fundamentals. 6th ed. Butterworth-Heinemann; 2013.

[74] IEEE Standard for Digitizing Waveform Recorders. IEEE Std 1057-2007 (Revision of IEEE 1057-1994). 2008;1:c1–142.